INFORMATION TO USERS

This manuscript has been reproduced from the microfilm master. UMI films the text directly from the original or copy submitted. Thus, some thesis and dissertation copies are in typewriter face, while others may be from any type of computer printer.

The quality of this reproduction is dependent upon the quality of the copy submitted. Broken or indistinct print, colored or poor quality illustrations and photographs, print bleedthrough, substandard margins, and improper alignment can adversely affect reproduction.

In the unlikely event that the author did not send UMI a complete manuscript and there are missing pages, these will be noted. Also, if unauthorized copyright material had to be removed, a note will indicate the deletion.

Oversize materials (e.g., maps, drawings, charts) are reproduced by sectioning the original, beginning at the upper left-hand corner and continuing from left to right in equal sections with small overlaps.

Photographs included in the original manuscript have been reproduced xerographically in this copy. Higher quality 6" x 9" black and white photographic prints are available for any photographs or illustrations appearing in this copy for an additional charge. Contact UMI directly to order.

ProQuest Information and Learning
300 North Zeeb Road, Ann Arbor, MI 48106-1346 USA
800-521-0600

MULTILAYER FREQUENCY SELECTIVE SURFACES AS ARTIFICIAL SUBSTRATES FOR BROADBAND CONFORMAL ARRAYS

by

Yunus Emre Erdemli

A dissertation submitted in partial fulfillment
of the requirements for the degree of
Doctor of Philosophy
(Electrical Engineering)
in The University of Michigan
2002

Doctoral Committee:

Professor John L. Volakis, Chair
Professor Anthony W. England
Professor Jeffrey B. Rauch
Professor Thomas B. A. Senior

ACKNOWLEDGMENTS

I am thankful to Professor John L. Volakis for serving as my dissertation chair and for his continued support and mentorship throughout my graduate studies at the University of Michigan. I would also like to acknowledge the other committee members Professors Anthony W. England, Jeffrey B. Rauch, and Thomas B. A. Senior for their invaluable comments and suggestions.

I would like to acknowledge the Higher Educational Council of Turkey in conjunction with Kocaeli University whose financial support made my doctoral studies possible. I also acknowledge DARPA/Reconfigurable Aperture Program (RECAP) for the sponsorship of this research.

Finally, I would like to thank my current and former colleagues as well as the staff in the Radiation Laboratory for their help and support during my graduate studies.

I am especially grateful to my family and my friends for their constant love, encouragement, and support throughout this work.

TABLE OF CONTENTS

LIST OF TABLES

Table

LIST OF FIGURES

Figure

CHAPTER 1

INTRODUCTION

The thesis describes the analysis methods and fast techniques for the characterization of the proposed multilayer arrays. This analysis is based on the finite element-boundary integral (FE-BI) method with fast spectral calculation of the Green's function [1]. The developed array concept has a number of key features introduced for the first time:

1) Frequency selective surfaces (FSS's) are exploited to develop substrates whose reflection coefficient response varies with frequency such that it enhances array performance. In this application of primary importance is the phase response. In effect, this FSS substrate is passively reconfigured [2].

2) A new broadband balun feed is designed and employed within the array for impedance matching over a large band of frequencies.

3) A reconfigurable cross-slot array is proposed over the FSS substrate and designed for broadband operation to take advantage of the passively reconfigured FSS [3]. The reconfiguration of slots is realized by using switches such as Micro-Electro-Mechanical-Systems (MEMS) switches or PIN diodes. It is demonstrated that a 2-band reconfiguration allows for 800-3200 MHz performance, and new slot designs are proposed for achieving even 10:1 impedance bandwidths.

In the following, we discuss the motivation that led to this research and proceed with a description of the proposed reconfigurable aperture and its components. The outline of the thesis is then presented.

Motivation & Proposed Array Concept

Advancements in mobile communication systems have resulted in many antennas competing for very limited real estate on military or commercial vehicles. Although progress in electronics technologies allows for packaging of more functionality in smaller volumes, the wavelength dependency of antennas continues to resist miniaturization. Since the dimensions of conformal antennas in the VHF, UHF, and L-bands are large in the context of vehicle installation, their use for multifunction systems has been restricted to frequency and time sharing of single antenna elements. Most of the research with multifunction arrays has been in the microwave and millimeter wave bands where array dimensions are small enough for installation between structural sections of the vehicle. Wideband elements, such as notch or tapered slots [4], can be arrayed with the critical spacing needed for multi-octave, grating lobe-free beam scanning at the shortest wavelength. With most other elements, such as slot spirals [5], log-periodics [6] or bow-ties, however, the penalty for close spacing is a reduction in gain, increased impedance mismatches, distorted radiation patterns and grating lobes as a result of the strong mutual coupling and in some cases blind angle phenomena (scan blindness). An antenna array technology where frequency, polarization and element spacing can be reconfigured in real-time would overcome many of these obstacles while allowing for a reduction in the size and weight needed for the conformal array.

A reconfigurable antenna array concept is presented here as a means of meeting this need. The proposed reconfigurable aperture illustrated in Figure 1.1 is comprised of simple radiating elements (printed dipoles or slots) whose dimensions can be altered by using RF switches such as MEMS switches [7] or PIN diodes. These elements are integrated into the top layer of a multilayered composite structure consisting of passive FSS's that form a broadband ground plane system. As feeding structures, broadband balun/feed elements [8] are used, providing balanced/matched excitation for the array. Next we describe the key features of these major components constituting the reconfigurable aperture.

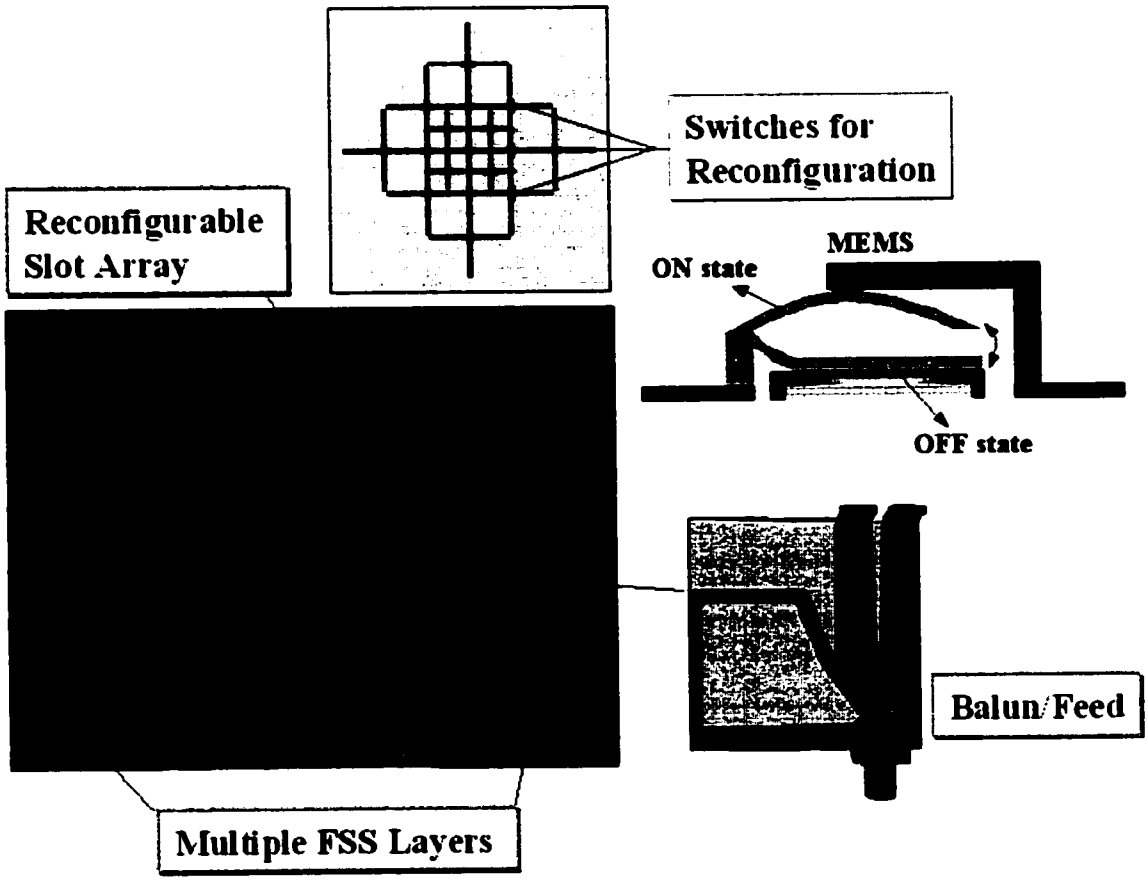

Figure 1.1: Reconfigurable antenna aperture and its components.

Antenna Elements

Crossed slot elements [9] are used to construct the proposed reconfigurable array (Figure 1.2). As shown in Figure 1.2, an interleaved two-band configuration of these elements is considered in order to reduce the array size as much as 40%. This choice of configuration also provides broadband array performance without grating lobes. In addition, use of crossed elements allows for both vertical and horizontal polarizations over the frequency band of interest.

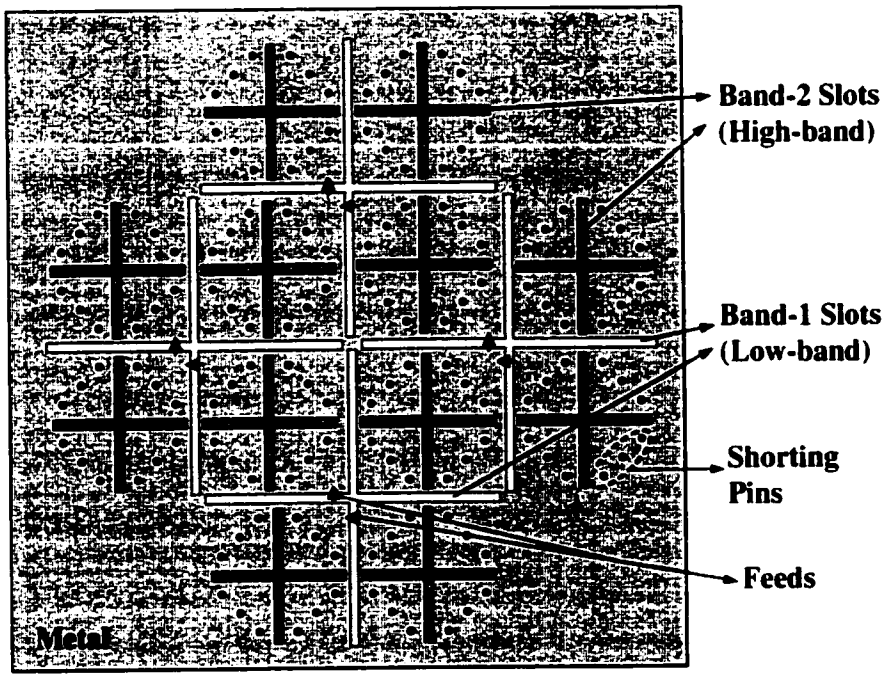

Figure 1.2: Two-band reconfigurable crossed-slot array with shorting pins. Band-1 configuration is shown where Band-1 slots are excited in the presence of unexcited (parasitic) Band-2 slots.

The reconfigurable array is placed at the top layer of the cavity-backed structure. Even though the cavity is necessary for a conformal structure, it introduces undesirable coupling effects and resonance modes. These parasitic effects can be mitigated by using shorting pins (see Figure 1.2) placed between the slot aperture and the ground plane. In the absence of an FSS substrate, a careful design of cavity depth along with shorting pin location can improve the bandwidth performance of the array. Additional improvement can be obtained by choosing slot size (width and length) and shape (varying slot width along the length) accordingly.

RF Switches

Array reconfiguration is achieved by means of RF switches such as MEMS switches (see Figure 1.1). The slot lengths are altered (increased or decreased) by using the "on" and "off" functions of the switch. At the off-state (open), the switch is configured to connect an extra length of the antenna element to meet the resonant length criteria for that frequency band. At the on-state (closed), the switch is configured to disconnect the extra length of the antenna structure. A good RF switch should have low insertion loss at the on-state, high isolation at off-state, fast on/off switching times, ability to withstand high voltages, low power consumption and a switching geometry that can be accommodated without disturbing the RF environment of the aperture.

FSS Substrate

The electrical spacing between the antenna array surface and the ground plane is a major parameter that strongly influences the overall array performance (VSWR, gain and radiation pattern). For optimum operation the effective electrical height between the array

surface and the ground plane should remain constant as the operating frequency changes. Since the physical spacing between the antenna array surface and the ground plane is fixed, such an electrical height change can be accomplished by modifying the effective dielectric constant of the material between the array plane and the ground plane. Such substrates employing perforated or bandgap materials have recently been used to increase the efficiency of printed antennas on thicker substrates [10]-[12]. However, these approaches are still applicable only to narrowband antenna structures. Instead, a passive ground plane with a multilayer FSS is a preferred choice for artificially altering the ground plane location. This can be achieved by using multiple layers of FSS's as part of the substrate in a manner similar to that used for designing broadband microwave filters. Each screen is resonant at a given frequency and is placed a distance $\lambda_s/4$ away from the antenna's surface, where λ_s refers to the wavelength at the screen's resonance frequency. In effect, the FSS used in the array acts as an adjustable ground plane maintained at a distance to give constant phase shift over a broad band, thus providing broadband array performance.

Feed Elements

In practice, to preserve bandwidth enhancement of the FSS substrate an equally broadband feed is required. For this purpose, compact, low-loss balun/feed structures are employed within the array (see Figure 1.1), providing a broadband balanced/matched feeding system which minimizes mismatch losses.

Outline

In this thesis, we consider analysis and design of the reconfigurable aperture components (except the switches) by means of a fast infinite array simulator, and we demonstrate enhanced bandwidth performances of the designed reconfigurable arrays. The formulation and validation of the full-wave simulator is presented in the Appendix.

In Chapter 2, we discuss the bandwidth limitation of conformal arrays and review possible ways to alleviate this caveat. In particular, we examine substrate/cavity effects and propose multilayer FSS's as artificial substrates to enhance the bandwidth performance. In Chapter 3, a simple circuit modeling of a dipole FSS is described, which leads to a multilayer FSS design having pre-specified reflection coefficient. In Chapter 3, we also introduce a novel FSS element which is then employed as a broadband substrate in Chapter 4, enhancing overall performance of a dipole array. A similar FSS substrate is extended to slot arrays in Chapter 5, providing bandwidth enhancement at the expense of some efficiency loss. In Chapter 6, we introduce a broadband balun/feed design, which is then incorporated into the slot/FSS design of Chapter 5, and we validate the final slot/FSS/balun design with measurements. In Chapter 7, we demonstrate bandwidth enhancements achieved for reconfigurable slot arrays over multilayer FSS substrates. Finally, we conclude with a summary of the accomplishments of this thesis work in Chapter 8.

CHAPTER 2

FREQUENCY SELECTIVE SURFACES FOR BANDWIDTH ENHANCEMENT

Bandwidth Limitation: Antenna Element & Substrate

Antenna bandwidth is determined by the antenna structure itself, material composition and the surrounding environment. Although, many approaches exist for designing broadband antennas, attention in recent years has been on developing radiating elements for conformal vehicle installation. In these cases, bandwidth is limited by the characteristics of the substrate rather than the antenna element itself.

Obviously, a narrowband element in isolation as is the case with the dipole or slot has its own bandwidth limitation. However, when placed on a substrate, its bandwidth is more severely affected. Certainly, one can re-shape or design elements for greater bandwidth. This is for example the case with bow-tie and spiral antennas (printed or slot) (see Figure 2.1). Alternatively, one could gain element bandwidth by loading or reconfiguring the element itself using switches as illustrated in Figure 2.2. Regardless of how the element bandwidth is enhanced, the major limitation for conformal arrays relates to the substrate. Consequently, much effort in recent years has been devoted to designing substrates that alleviate this bandwidth limitation.

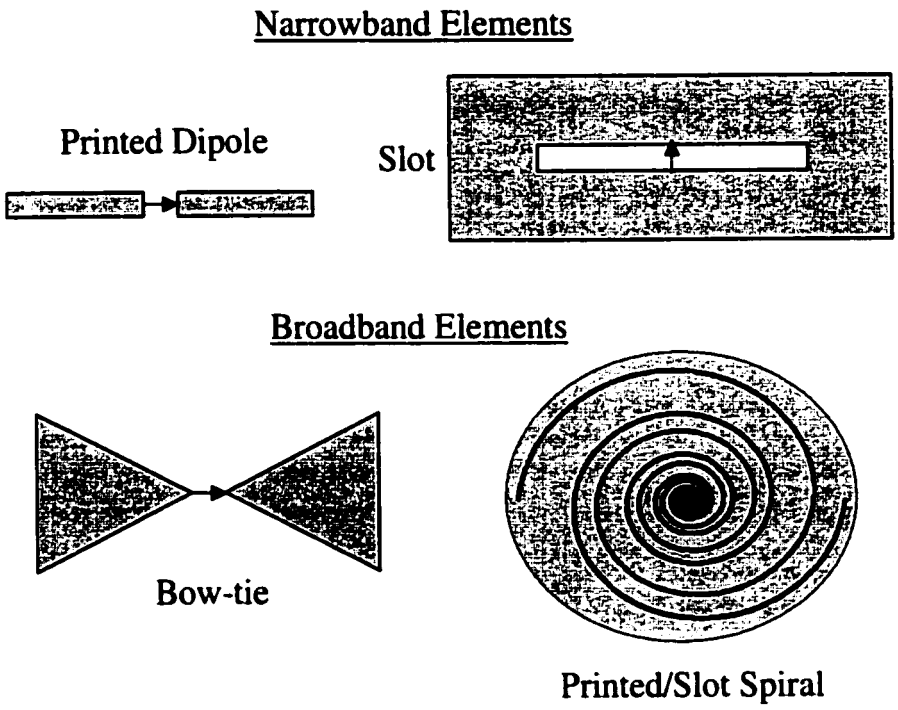

Figure 2.1: Examples of conformal antennas.

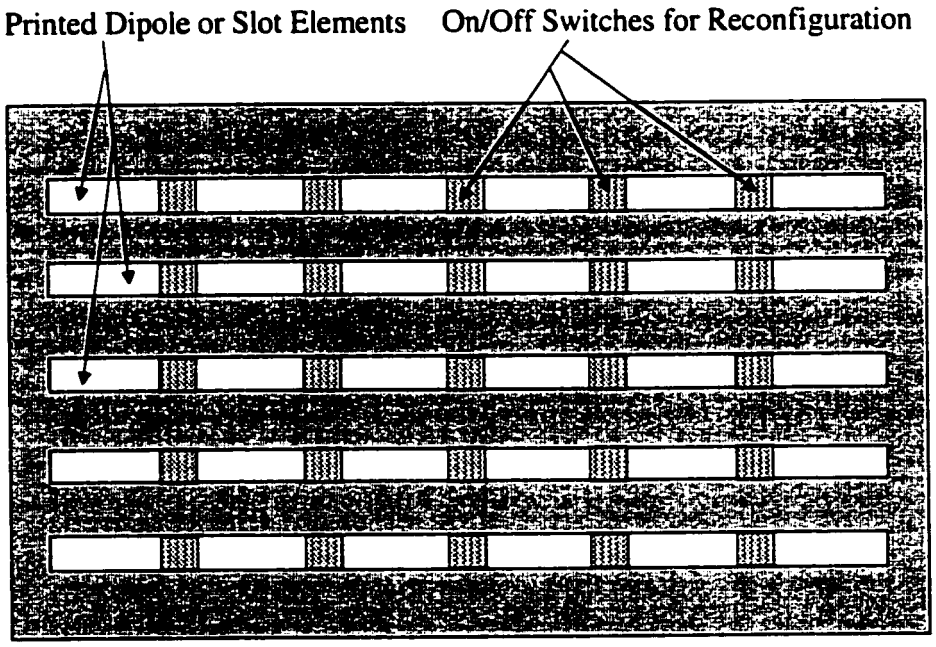

Figure 2.2: Reconfigurable dipole/slot array.

Conformal antennas are often printed on a planar or curved substrate comprised of a dielectric material backed by a metallic (conductive) surface (Figure 2.3). This metal sheet is used as a reflector or ground plane (GP) that partially shields objects on the other side. The presence of a GP plays an important role in antenna performance since it re-directs one-half of the radiation into the opposite direction (upper half-space), thus improving antenna gain by 6 dB. However, this optimum performance is obtained only when the antenna-to-GP distance is one quarter of wavelength at the operating frequency, making this operation quite narrowband. Also, for printed antennas, if the element is placed too close to the GP, poor radiation efficiency occurs due to current shorting. As is well known the perfect electric conductor (PEC) has the property of the reversing the phase of the reflected field at the metal-dielectric interface. Therefore, when the antenna is placed near the GP, the directly radiated field is cancelled by the reflected.

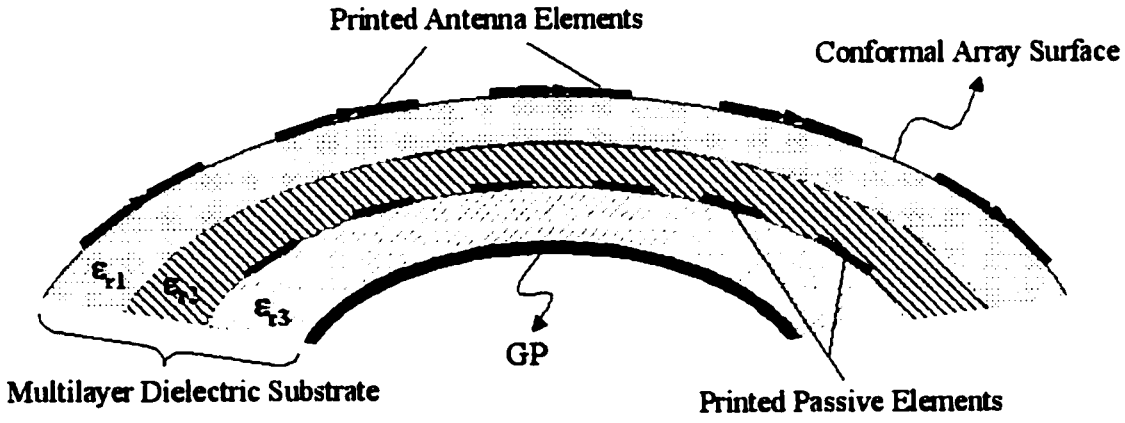

Figure 2.3: A general conformal antenna array/substrate configuration.

Another feature of the metal-backing relates to surface waves [13] supported by the substrate. These undesired waves that propagate along the metal-dielectric interface

causing low efficiencies, particularly, in high dielectric-constant or thick substrates. On a finite GP, surface waves propagate till they reach an edge or corner and subsequently radiate into free space as illustrated in Figure 2.4. Such diffracted components thus cause radiation pattern disturbances (ripples in the patterns). In the case of multiple antennas sharing the same GP, e.g., in an array environment, these surface currents can cause undesired mutual coupling between adjacent antenna elements.

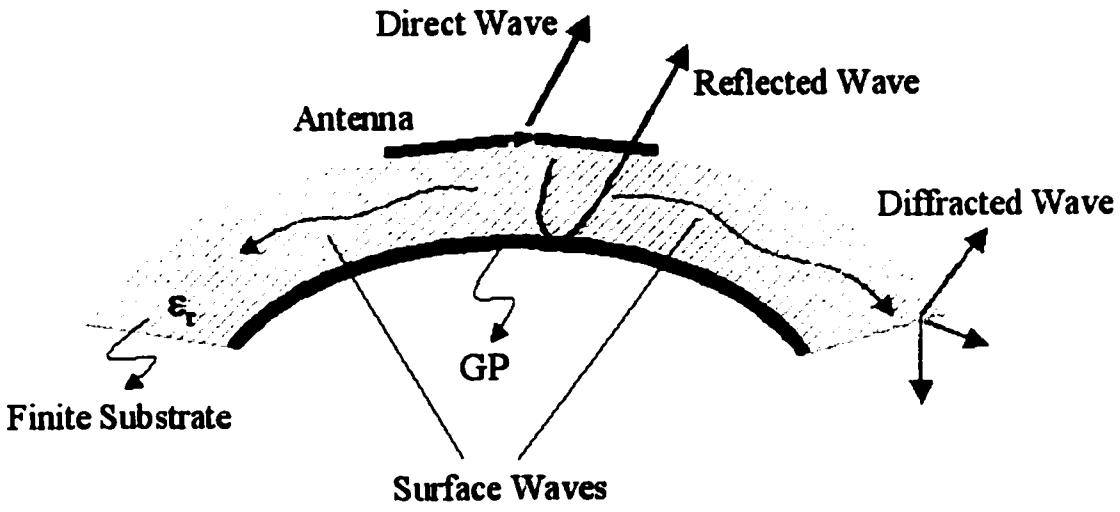

Figure 2.4: Surface waves within a cavity-backed substrate.

Photonic Bandgap (PBG) Substrates

Perforated or bandgap substrates [10]-[12], [14]-[22] have recently been proposed to improve bandwidth of conformal antennas as well as suppress surface wave phenomena. These novel substrates are a form of frequency selective volumes (Figure 2.5), which were originally introduced as photonic bandgap (PBG) materials [23]. They mimic perfectly magnetic conductors (PMCs) [24], [25] and inhibit the occurrence of surface waves within a "forbidden" frequency band [18]. Of significance to conformal antennas is that PMCs do not result in phase-reversal (180° phase shift) of the reflected waves, unlike PECs. On the contrary, when the wave impinges upon a PMC, it reflects the wave with no-phase change, i.e., 0° phase shift (see Figure 2.6). Consequently, the direct and reflected waves are in congruence to enhance radiation. These artificial magnetic GPs can provide in-phase reflections within a particular frequency band, i.e., PBG. Hence, the antenna performance is greatly enhanced over that specific bandgap, determined by the properties of PBG materials constituting the substrate (thickness, periodicity, material constituents, etc.).

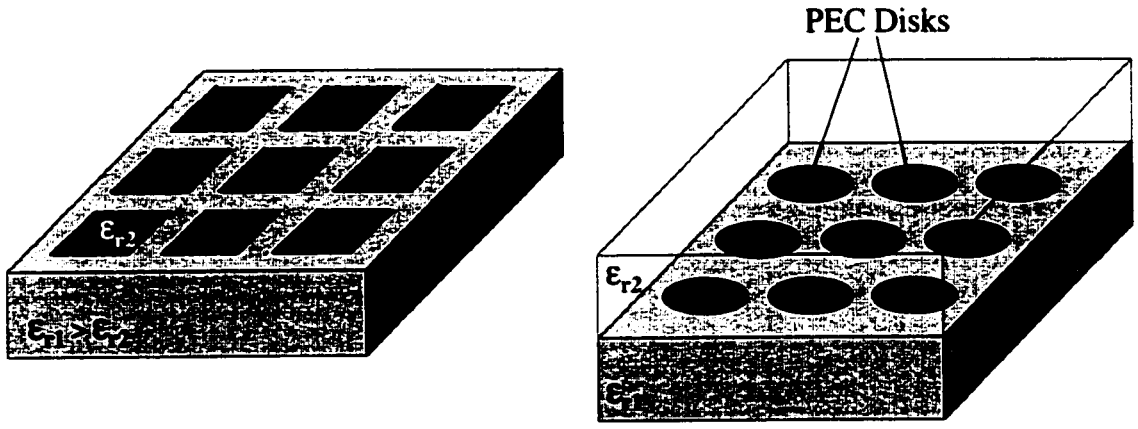

Figure 2.5: Example PBG configurations.

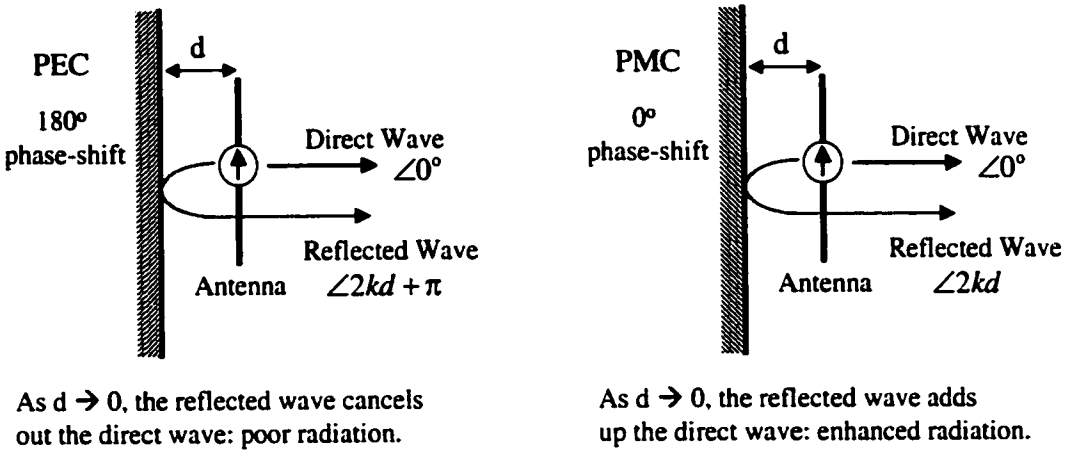

Figure 2.6: Reflection at PMC boundary vs. PEC boundary.

The PBGs are known to have fairly high surface impedance within their bandgaps [18], [26], but to better understand their behavior it is instructive to examine an equivalent circuit of the PBG substrate. To do so, each element of the periodic substrate is represented by an equivalent L and C (surface inductance and capacitance [27]) parallel connection which defines the surface impedance. This network of parallel resonant LC circuits (illustrated in Figure 2.7) act as an electric filter to block the flow of surface currents along the metal sheet. At the frequencies (i.e., within the bandgaps) where the periodic loading becomes open, a magnetic surface is generated. Example PBGs such as the uniplanar compact PBG [24] and the mushroom-like PBG [27] (see Figure 2.8) have been successfully used to emulate such high-impedance PMC surfaces.

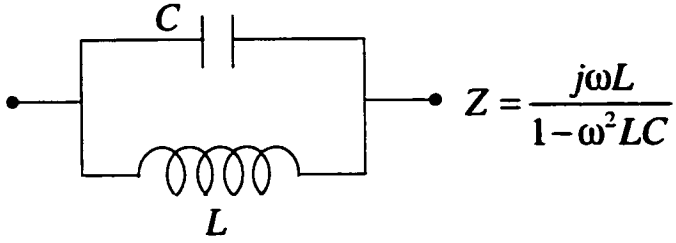

Figure 2.7: LC equivalent circuit representation of a high-impedance surface.

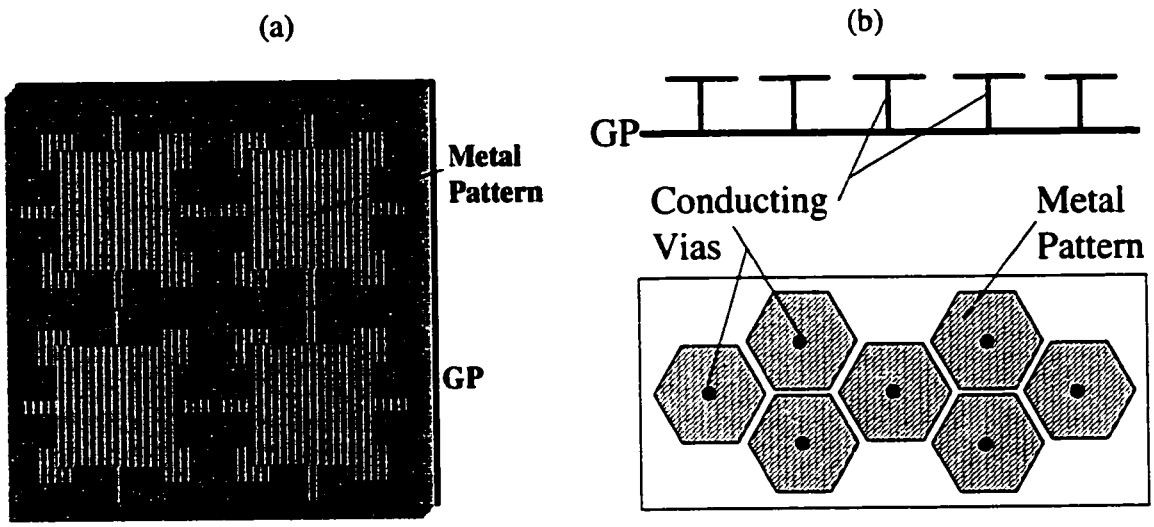

Figure 2.8: Examples of textured PBGs: (a) uniplanar compact PBG [24] (b) mushroom-like PBG [27].

The PBGs provided some means for increasing printed antenna bandwidth. However, their electrical behavior as magnetic conductors is limited to a narrow bandgap region. This is also the bandwidth over which the reflection coefficient falls between $+\pi/2$ and $-\pi/2$, and image currents are more in-phase than out-of-phase (see Figure 2.9). Clearly, the (frequency) boundaries of this behavior represent the maximum usable bandwidth of a flush-mounted antenna. As noted in [18], the relative bandwidth is proportional to $\sqrt{L/C}$ where L and C represent the equivalent surface inductance and capacitance of a high-impedance surface. The bandwidth can be controlled by selecting the parameters L and C accordingly. Typically, the capacitance is related to the surface dimensions of the texture as well as the number of layers within the structure. On the other hand, the inductance is mainly determined by the thickness of the structure (a linear proportionality). PBG materials or equivalently high-impedance surfaces behave as magnetic GPs only over a narrow band, but also the widths of these bands reduce as the

operation frequency decreases. So far, PBGs have been shown to provide operational bandwidths of 30% or so [19]. However, the goal of obtaining 2:1 bandwidth (or equivalently 150%) is far from being achieved.

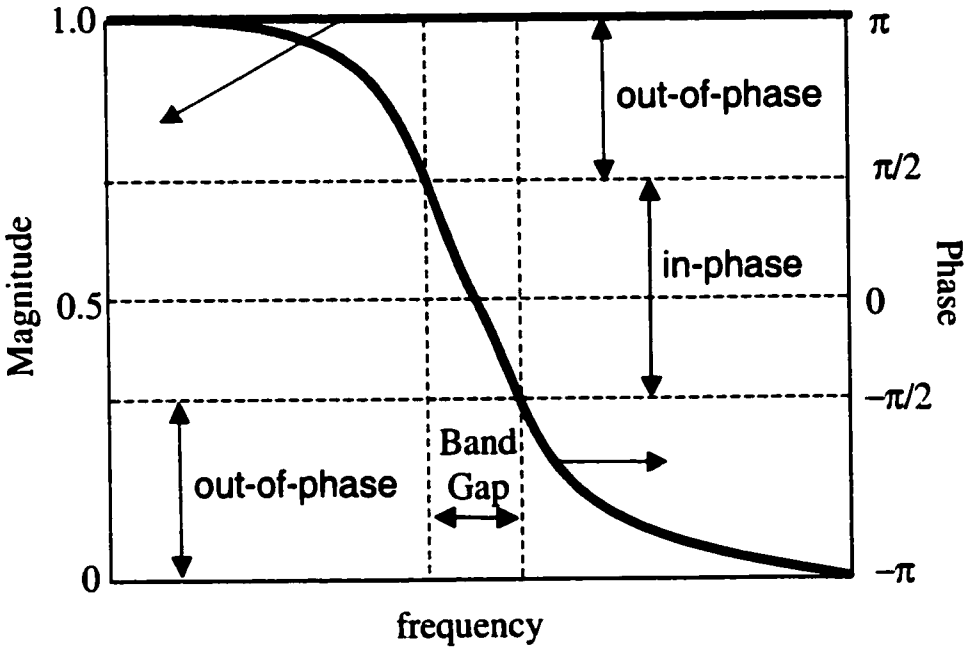

Figure 2.9: A characteristic reflection response of PBG substrates.

Frequency Selective Surface (FSS) Artificial Substrates

In this thesis we consider an alternative and a different class of substrates for improving conformal antenna bandwidth. One can instead employ a multilayer frequency selective surface (FSS) structure underneath a printed antenna or an antenna array (see Figure 2.10) to enhance its overall radiation as well as bandwidth performance [2]. FSS's are very similar in many respects to PBGs or frequency selective volumes. Both structures are periodic, but an FSS is planar and much simpler to construct and design. Moreover, multiple layers of FSS's can increase design flexibility. Of particular importance is that the FSS design and fabrication is entirely based on printed circuit technology. Additionally, a large body of knowledge and design techniques exists for FSS's [28], [29].

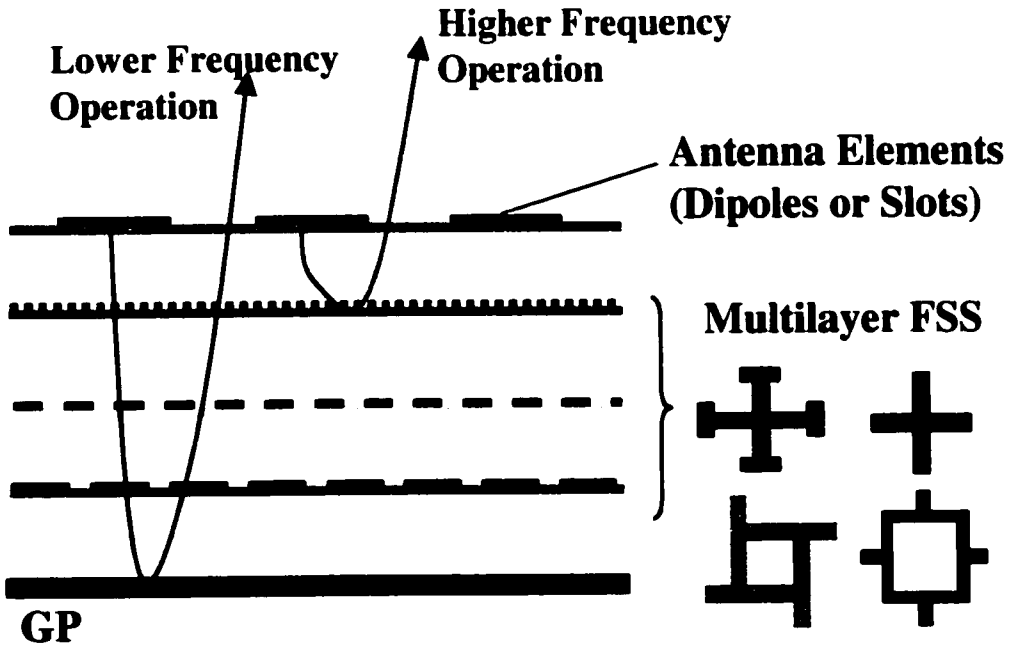

Figure 2.10: Proposed multilayer FSS substrate for conformal arrays.

Here the goal is to design such multilayer FSS's to emulate a PMC ground plane in much the same way as done by PBGs. Of particular interest is the design of arrays over a 2:1 bandwidth using these artificial substrates. Our goal is to accomplish this by optimizing the FSS parameters within a unit cell (size, orientation, loading, etc.), number of layers and the separation between layers as well as the periodicities of each layer to meet pre-specified reflection coefficient characteristics. The intended FSS will be designed so that the reflection coefficient phase remains within the range of $[-\pi/2, +\pi/2]$ over a broad band of frequencies. With such a phase response, the FSS should mimic a PMC ground plane. It is further important to note that the emphasis of our designs is on phase and not on amplitude as in the past.

In designing a multilayer FSS to achieve a nearly flat phase response, it is important to consider an equivalent circuit model of the FSS. For this purpose a simple, yet useful circuit model for a dipole FSS is developed in this thesis work. Such an equivalent model is shown in Figure 2.11 and consists of a series *LC* circuit with the *L* and *C* values related to actual dipole dimensions and periodic lattice parameters as will be discussed later. This prototype circuit model can also be used to design multilayer FSS structures by using stacks of equivalent *LC* circuits cascaded by inserting TLs between them. Since this is a first order model, its accuracy is degraded as the frequency increases. Further, in the case of lossy FSS elements, an additional resistor must be added in series to each *LC* branch to account for the introduced loss [2].

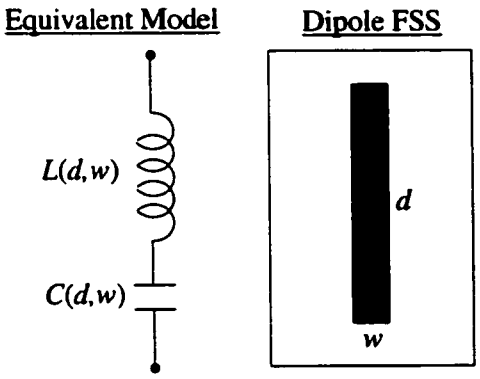

Figure 2.11: Proposed *LC* model for dipole FSS.

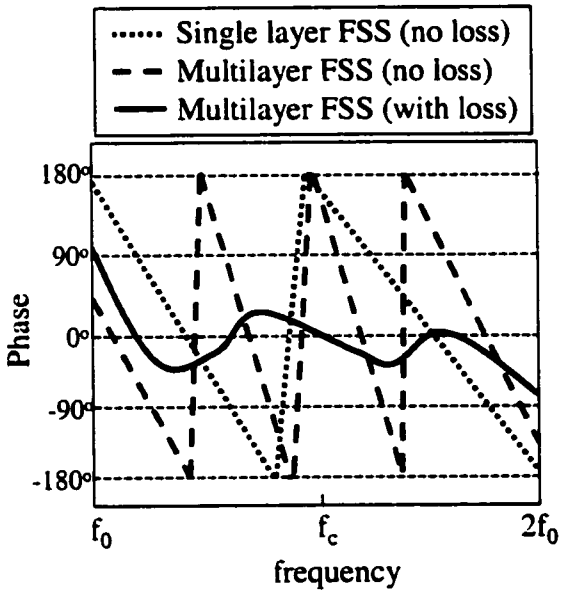

Figure 2.12: Characteristic phase response of multilayer FSS substrate with and without presence of loss.

To achieve a nearly flat-phase response around 0° over a broad range of frequencies, some loss needs to be introduced to smooth out the phase variation. As an example, consider a single layer FSS consisting of metallic printed elements (e.g., dipoles) placed within a cavity-backed structure. The resulting phase response (see Figure 2.12) is seen to have the characteristic zigzagging as the frequency is varied. For a

multilayer FSS structure, the number of oscillations increases accordingly over the same band (see Figure 2.12). In effect, the FSS behaves like a PMC within a narrow band around each zero-phase crossing. Hence, such an FSS substrate can be used in multiband antenna applications [30]. However, when some loss is introduced within the FSS (in the form of resistive cards), the phase oscillations are smoothed out, resulting in a nearly constant phase response over a broad bandwidth as depicted in Figure 2.12.

As part of our design effort, a goal is to also minimize the thickness of the multilayer FSS structure and this can be achieved by using rather broadband FSS elements. Such elements can be usually obtained by loading the canonical elements such as crossed dipoles, resulting in the well known Jerusalem crosses. If the element shape is designed such that both "capacitive" surface (dipoles or patches; band-stop filter) and "inductive" surface (slots or loops; band-pass filter) properties [29] are realized within the same structure, the resulting elements are expected to provide broadband performance. Such a novel, broadband element is introduced here and is shown in Figure 2.13. This fan-like element can be thought as a combination of a loop (inductive) and dipoles (capacitive). By tuning the lengths of the legs (dipoles) and the inner radius of the loop, the resonance behavior of the FSS and its bandwidth can be controlled. Also, when a resistively loaded fan element is used, very broadband responses can be achieved.

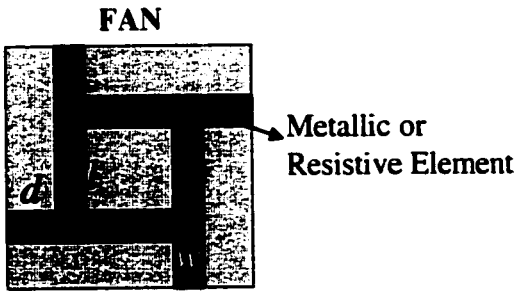

Figure 2.13: Proposed broadband FSS element: "Fan" element.

One can ask at this point whether a similar performance can be obtained by introducing some loss in the dielectric substrate instead of using a lossy FSS. Figure 2.14 shows that the lossy substrate slightly improves –10dB return loss (S_{11}) bandwidth, but the losses are rather large, whereas the FSS provides for a variable loss control using resistive cards.

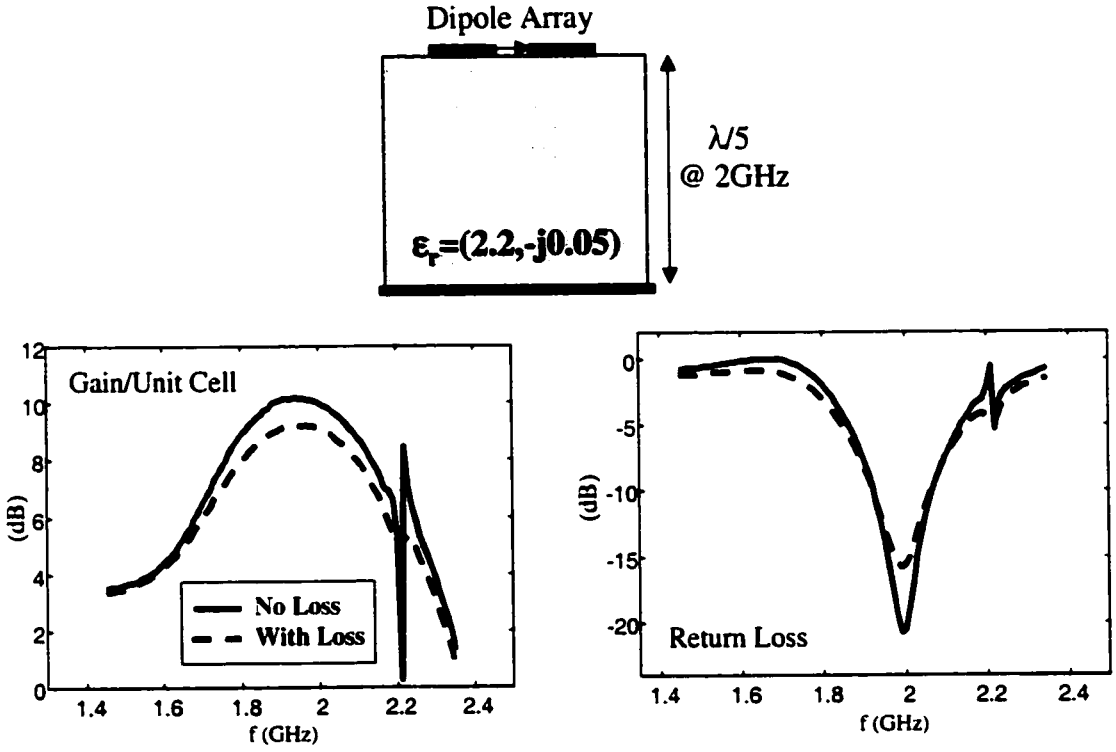

Figure 2.14: Dipole array performance over a lossy substrate.

Antenna Loading vs. Reconfiguration

For even greater bandwidth enhancements, loading and/or reconfiguration of the antenna element can be employed. Reconfiguration provides multiband operation by changing (increasing or decreasing) the antenna elements lengths (dipoles or slots) using switches (see Figure 2.2). For a two-band reconfiguration, multiple FSS substrates may be needed [3]. However, inclusion of the secondary FSS deteriorates the impedance characteristics for the low-band operation. In fact, the frequency response is shifted downwards, leaving a gap between low-band and high-band characteristics. To close this gap in the response, one can consider reactive loading within the slot elements in much the same way as done for miniaturization [31]. The purpose of loading is to increase the inductance or capacitance per unit length of the antenna and thus slow down the wave, with the goal of decreasing the antenna's operational frequency. By doing so, the high-band response is shifted downwards and the impedance response becomes more consistent/uniform across the entire band. Such novel loading techniques are proposed here, providing almost 10:1 impedance bandwidth coverage with reconfiguration.

In this chapter, we pointed out that the main issue with today's conformal arrays is their bandwidth limitation caused by substrate/cavity effects. Use of multilayer FSS's to serve as artificial substrates are proposed here to enhance the bandwidth performance of conformal arrays. These FSS's allow for design and loading control. Next we present a systematic procedure to design such substrates.

CHAPTER 3

FREQUENCY SELECTIVE SURFACE DESIGN FOR CONSTANT PHASE RESPONSE

As discussed earlier, a multilayer FSS configuration is proposed to enhance the bandwidth performance and impedance of the narrowband printed antenna. Of particular interest here is the development of FSS's which reflect with a pre-specified phase and amplitude over a broad set of frequencies. When the phase is actually maintained near zero degrees, such FSS's serve to emulate magnetic GPs (Chapter 4). As such, they can substantially enhance the radiation properties of printed antennas placed over the FSS since the reflected field will be in phase with that directly radiated by the antenna itself (see Figure 3.1). When the FSS is designed to deliver nearly constant phase over a broad bandwidth, substantial gain enhancement can be achieved over a wide range of frequencies (Chapter 4). In the past, FSS designs were mostly concerned with amplitude responses. However, when the FSS is used as substrate or serves as a GP for a printed antenna, the emphasis is on phase. One way to achieve smooth phase responses is to compromise the amplitude response, and this effect is demonstrated here.

In this chapter, we first present a simple circuit modeling of a dipole FSS, which leads to a multilayer FSS design having pre-specified reflection coefficient. We also introduce a novel FSS element which delivers the broadband properties needed for proposed antenna array design.

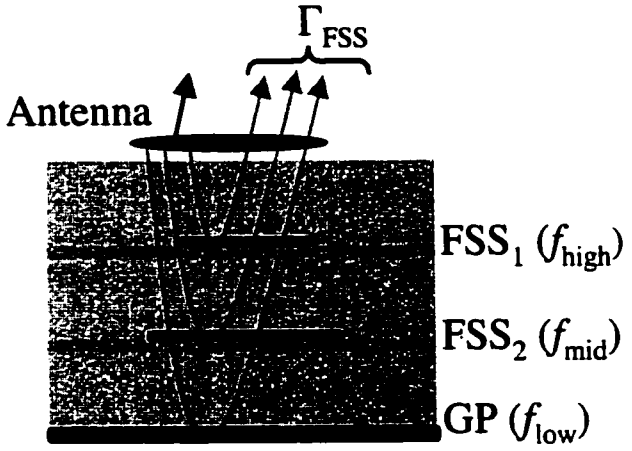

Figure 3.1: Coherence between antenna radiation and reflections from the substrate provides broadband operation.

Equivalent Circuit Modeling of Dipole FSS

A simple circuit model to predict the electromagnetic behavior of a single layer FSS plays a crucial role in the design process of multilayer FSS structures [29]. Employing the full-wave simulator in an optimization loop is not necessarily a viable strategy in designing multilayer FSS structures since such an approach is time consuming and inefficient. On the other hand, once obtained, the circuit model can be easily incorporated into existing circuit optimizers to provide geometry parameters that satisfy a given objective.

In this section, we present an equivalent circuit model for a strip dipole FSS. Our goal is to use this simple element as an example in understanding the FSS design for achieving nearly constant phase responses over a certain bandwidth. To this end, we first employ the equivalent circuit model to develop an initial design of the FSS. Full-wave

simulation results are then carried out as a final step on the basis of the derived circuit parameters.

For a single layer dipole FSS, the resonant behavior of the reflection coefficient suggests that a similar response can be obtained using an *LC* equivalent circuit. We use a first order transmission line/circuit (TL/CKT) model in conjunction with a simplex (direct search) curve-fitting algorithm [32] to determine the equivalent circuit parameters. The block diagram of this procedure is depicted in Figure 3.2. As shown, a dipole FSS structure is first analyzed using the full-wave simulator, and the reflection coefficient (Γ) of the FSS is then utilized in the simplex search algorithm to determine the corresponding circuit parameters. In the design process, it is essential to relate the circuit parameters L and C to the geometrical parameters of the structure. For this purpose, various dipole geometries were simulated by varying their lengths (d) and widths (w) using the full-wave simulator. As a result of this study, the following design formulae were developed:

$$L = \frac{A_L}{d\sqrt{w}} Z_0 \ \text{(nH)} \quad \text{and} \quad C = A_C \, d^3 \sqrt{w} / Z_0 \ \text{(nF)} \tag{3.1}$$

where the dipole dimensions d and w are in cm and Z_0=377Ω. Also, A_L and A_C are some constants to be determined during the curve-fitting process. They are dependent on the dielectric constant and thickness of the substrate (ε_r,t), element separation (D_x,Dy), and incidence angle (θ_i,ϕ_i). For the specific case of a free-standing dipole FSS having unit cell dimensions D_x=D_y=7.5cm and normal incidence, $A_L = 0.7674 \, (\text{nsec} \cdot \text{cm}^{3/2} \cdot \text{rad}^{-1})$ and $A_C = 0.1811 \times 10^{-3} (\text{nsec} \cdot \text{cm}^{-7/2} \cdot \text{rad}^{-1})$.

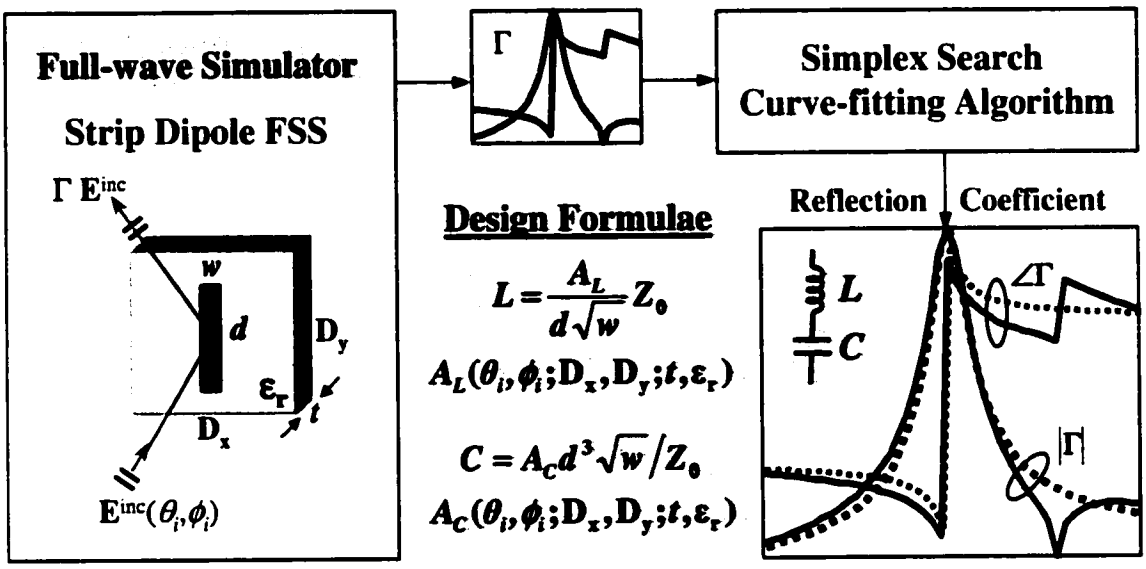

Figure 3.2: Building the equivalent circuit model for a single layer dipole FSS.

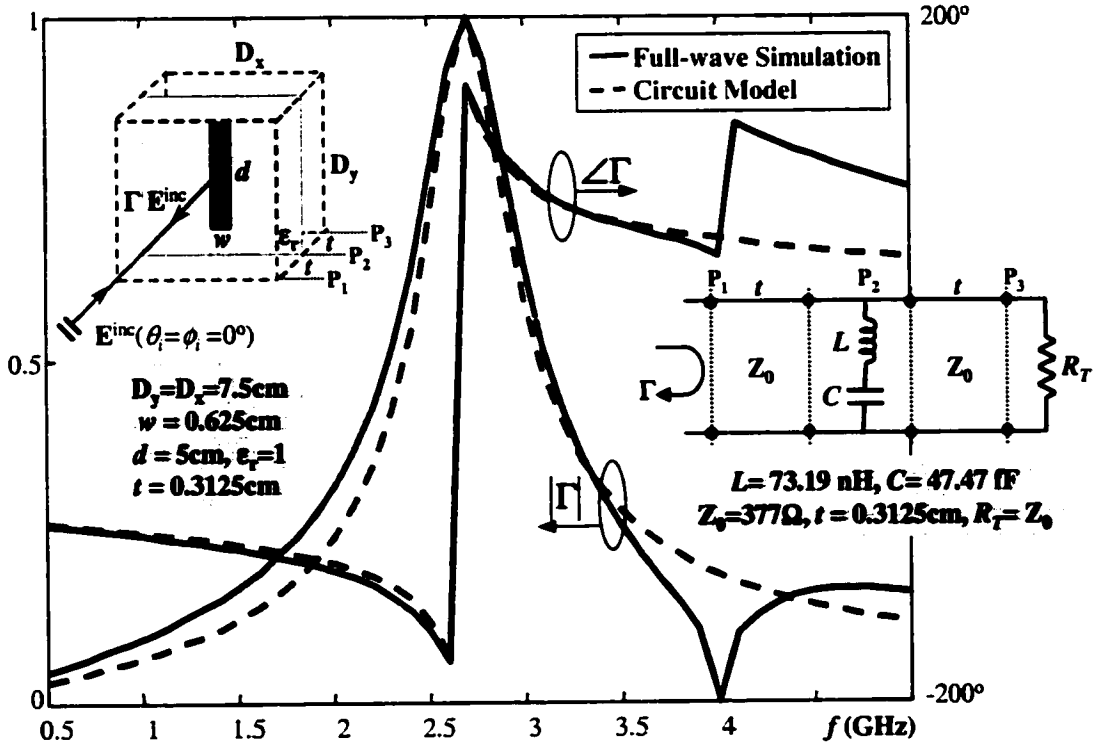

Figure 3.3: Reflection coefficient of a freestanding dipole FSS: the full-wave simulation (solid) versus the circuit model (dashed).

As an example, we display the reflection coefficient of a freestanding dipole FSS (d=5cm, w=0.625cm) along with its equivalent circuit (L=73.19nH, C=47.47fF) in Figure 3.3. As seen, the reflection coefficient based on the circuit model agrees sufficiently well with the actual reflection coefficient over a wide frequency band.

Note that the relations given in (3.1) represent a first order TL/CKT model, valid only for a single layer dipole FSS structure. Coupling between elements on the same FSS layer should also be incorporated in the model to obtain a broadband equivalent circuit representation, thus allowing periodicity parameters to be accounted for. In addition, for different incidence angles, A_L and A_C must be re-evaluated.

The above prototype circuit model can be used to design the multilayer FSS structure. We propose to model the FSS behavior using stacks of equivalent LC circuits cascaded by inserting TLs between them. As an example, we consider the optimum design of a three-layer lossless dipole FSS configuration with the pass-band response in the frequency range of 1.5-3.5 GHz. The lengths and widths of dipoles are varied as well as the separation between the layers during the optimization process. The comparative results for the TL/CKT model and the full-wave simulation are displayed in Figure 3.4. As seen, the optimization based on the first order model agrees very well with the full-wave simulation in the frequency band of 0.5-2.5 GHz. However, the agreement deteriorates beyond 2.5 GHz since the first order model design neglects higher-order mode coupling among the layers.

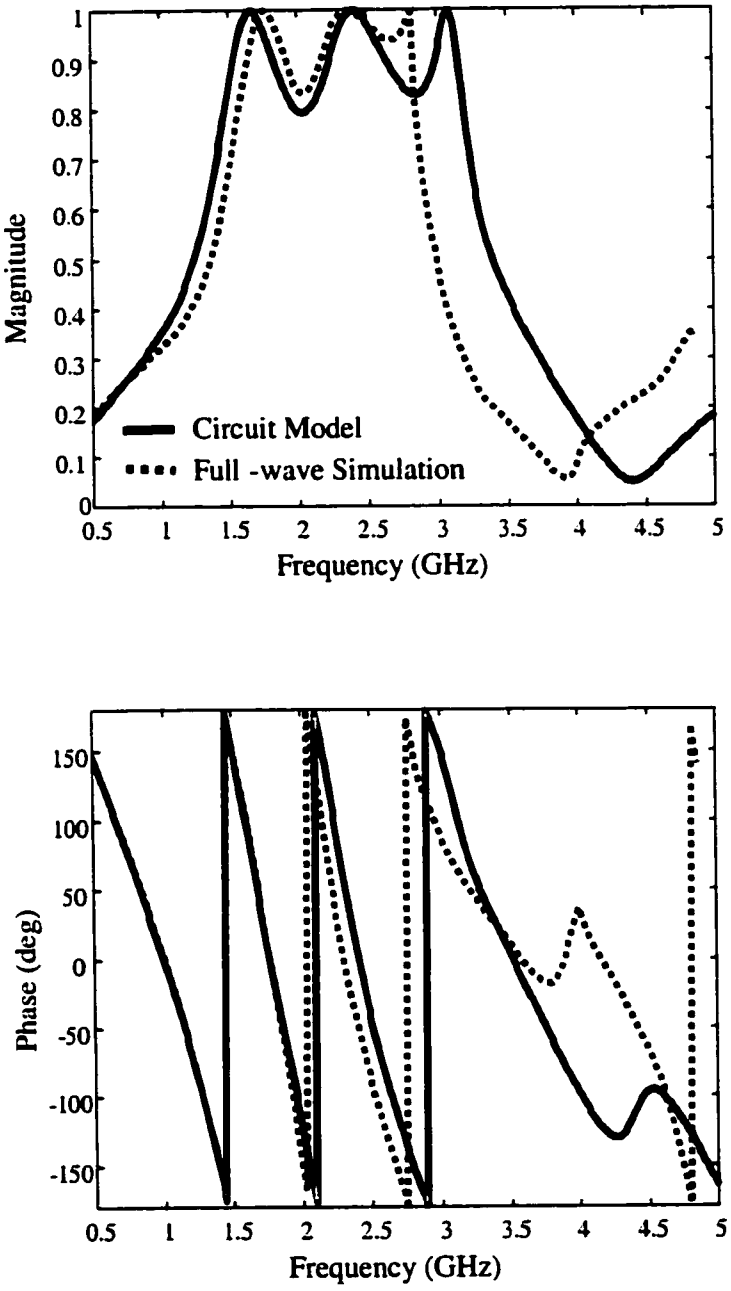

Figure 3.4: Reflection coefficient of the three-layer dipole FSS structure: the circuit model (solid) versus the full-wave simulation (dashed).

Design of FSS for Flat Phase Response

Of particular importance in assessing the results of Figure 3.4 is that the phase of the reflection coefficient is highly oscillatory. Hence, with a lossless FSS structure, it is not possible to obtain a reflection coefficient having a nearly flat phase response. To design a broadband GP, sharp variations in the phase must be eliminated so that the FSS reflected field could have a nearly constant phase response. As such, this reflected field will add in congruence with the direct antenna radiated field. By analogy with circuit theory, the phase response can be smoothed out by introducing some loss in the FSS structure. Resistive cards (R-cards) can be placed on the FSS layers for this purpose to smooth out the phase response in the pass-band at the expense of efficiency. In the corresponding circuit model, the effect of R-cards can be included by adding a resistor in series with the *LC* branch of the equivalent circuit. There is, of course, a trade-off between the flat phase response and the amplitude of the reflection coefficient. Introducing R-cards in the structure allows for a smooth phase response, but decreases the reflection coefficient amplitude. Next, we consider such a multilayer FSS design incorporating R-cards to simulate a broadband flat-phase GP.

Multilayer Crossed Dipole FSS

A three-layer FSS structure has been designed to simulate a broadband flat-phase GP for a practical reconfigurable array. In this case, the FSS is designed to reflect a wave that is in phase with the direct field radiated by the antenna towards the horizon. For practical purposes, the FSS design objectives for the reflection coefficient (Γ) are as follows:

$$\begin{aligned} &\text{Magnitude}: \ 0.4 < |\Gamma| < 1.0 \\ &\text{Phase}: \ -50^{o} < \angle\Gamma < 50^{o} \end{aligned} \qquad 3.2$$

These are based on achieving a maximum of 4dB loss (direct + reflected) in reference to an ideal reflector with $\Gamma=1e^{j0}$. First, according to the criteria above, a three-stage circuit modeling of the structure was devised as depicted in Figure 3.5. To smooth out the phase response, we introduced some loss by adding a resistor (R_i, i=1,2,3) in series within each LC branch of the circuit. Note that this structure is terminated by a short circuit, i.e., R_T=0. In Figure 3.6, the reflection coefficient of this three-stage TL/CKT design is shown for the cases with and without loss, i.e., R_i>0 and R_i=0 (i=1,2,3), respectively. As seen, the design objectives in (3.2) are achieved quite well in almost a 3:1 bandwidth by using the lossy TL/CKT design.

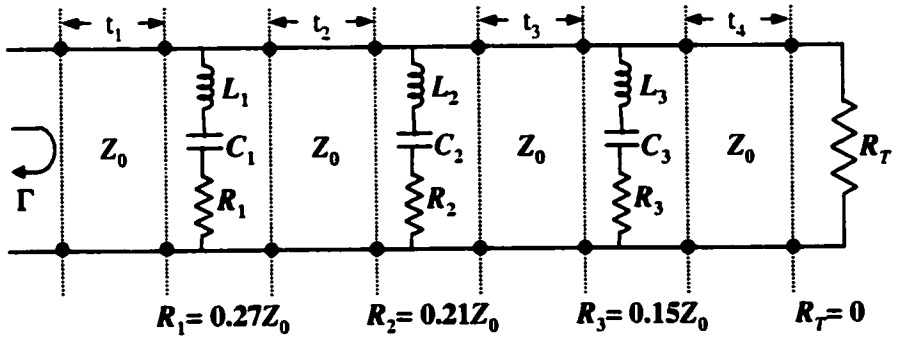

Figure 3.5: Three-stage TL/CKT design to achieve the criteria given in (3.2).

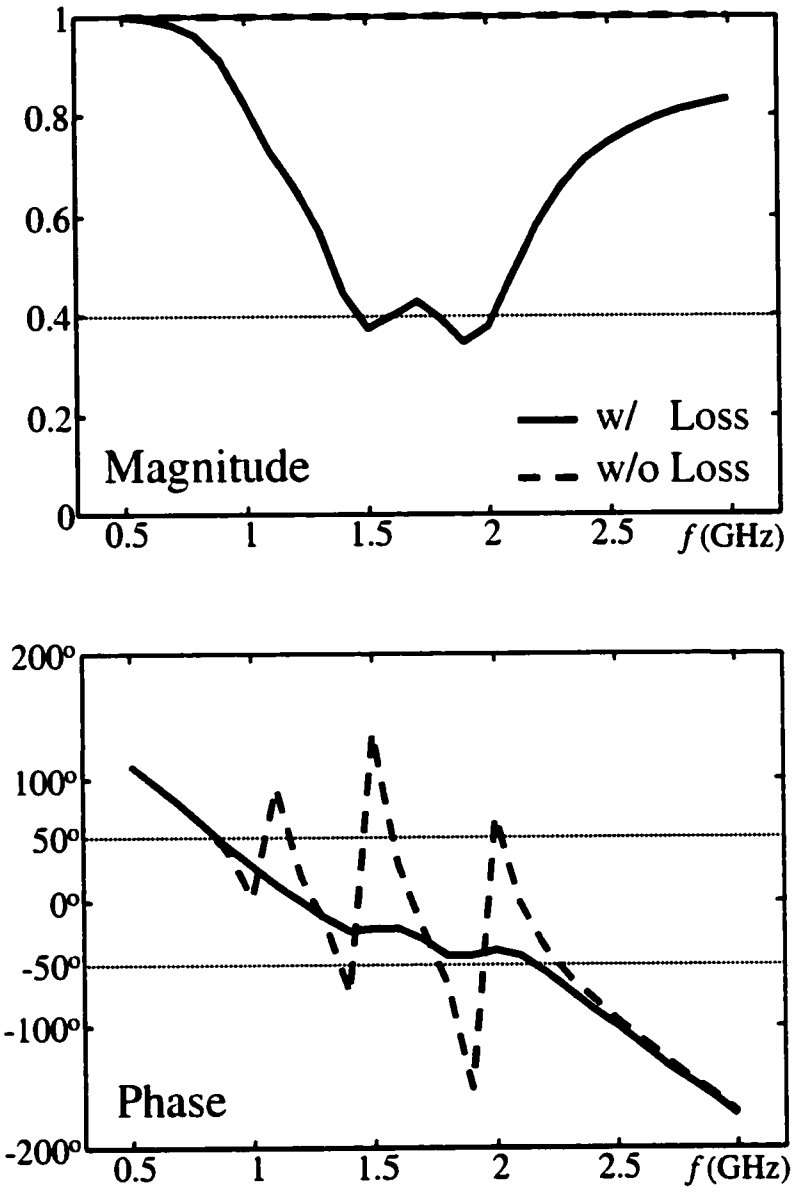

Figure 3.6: Reflection coefficient of the three-stage TL/CKT design in Figure 3.5 with and without loss.

Next, based on the equivalent circuit model for a single layer dipole FSS, the actual FSS structure was formed as shown in Figure 3.7 with the dimensions given in Table 3.1. As seen, this non-commensurate structure consists of closely packed crossed dipoles as FSS elements to achieve a broadband and polarization-free response. The dimensions of the strip dipoles forming the crossed dipole on each FSS layer were determined by the equivalent model formulae (3.1). The multilayer structure is backed by the ground plane (GP), representing the short circuit termination. In addition, the FSS elements are interleaved by R-cards to obtain the flat-phase response. In fact, these R-cards represent the resistors present in the TL/CKT design (see Figure 3.5). The R-card

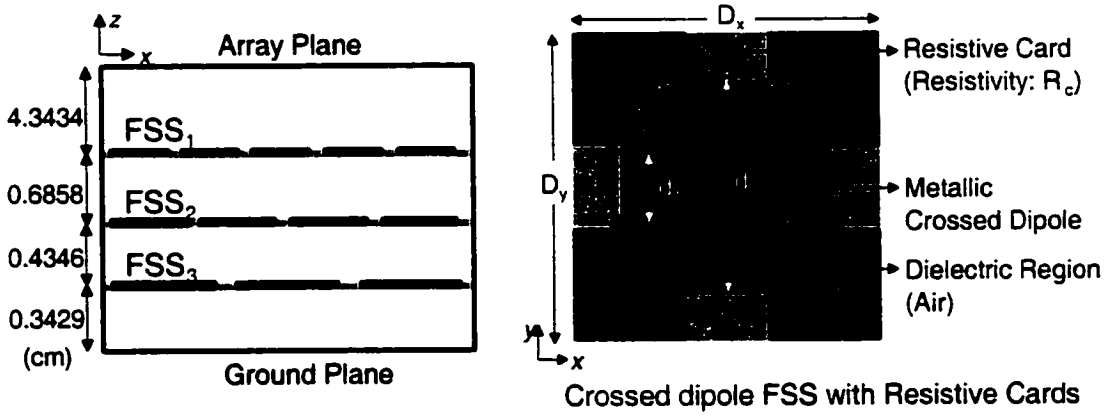

Figure 3.7: Configuration and unit cell geometry of the three-layer crossed dipole FSS.

(cm)	FSS_1	FSS_2	FSS_3
d_1	3.012	3.270	3.702
d_2	5.890	7.560	10.776
$D_{x(y)}$	10.0	12.0	16.0
$R_c(\Omega/cm^2)$	1800	1400	1000

Table 3.1: Dimensions of the crossed dipole FSS's.

parameters (resistivity and dimensions) were optimized to meet the design criteria (3.2). No design formula was used to relate the resistor values in the circuit model to the R-card parameters. However, the ratios of resistor values remained the same as those of the corresponding resistivity values, i.e., $R_1/R_3=R_{c1}/R_{c3}$ and $R_2/R_3=R_{c2}/R_{c3}$. In Figure 3.8, the full-wave simulation results for the designed three-layer FSS structure are displayed for a normally incident plane wave. We observe that the design criteria for the reflection coefficient are indeed attained whereas the resistive loading flattens the phase at the expense of some efficiency. Also, note that the circuit model response given in Figure 3.6 agrees well with the actual response in Figure 3.8. Though being a first order model, the developed TL/CKT model has been very useful in understanding and designing multilayer FSS structures.

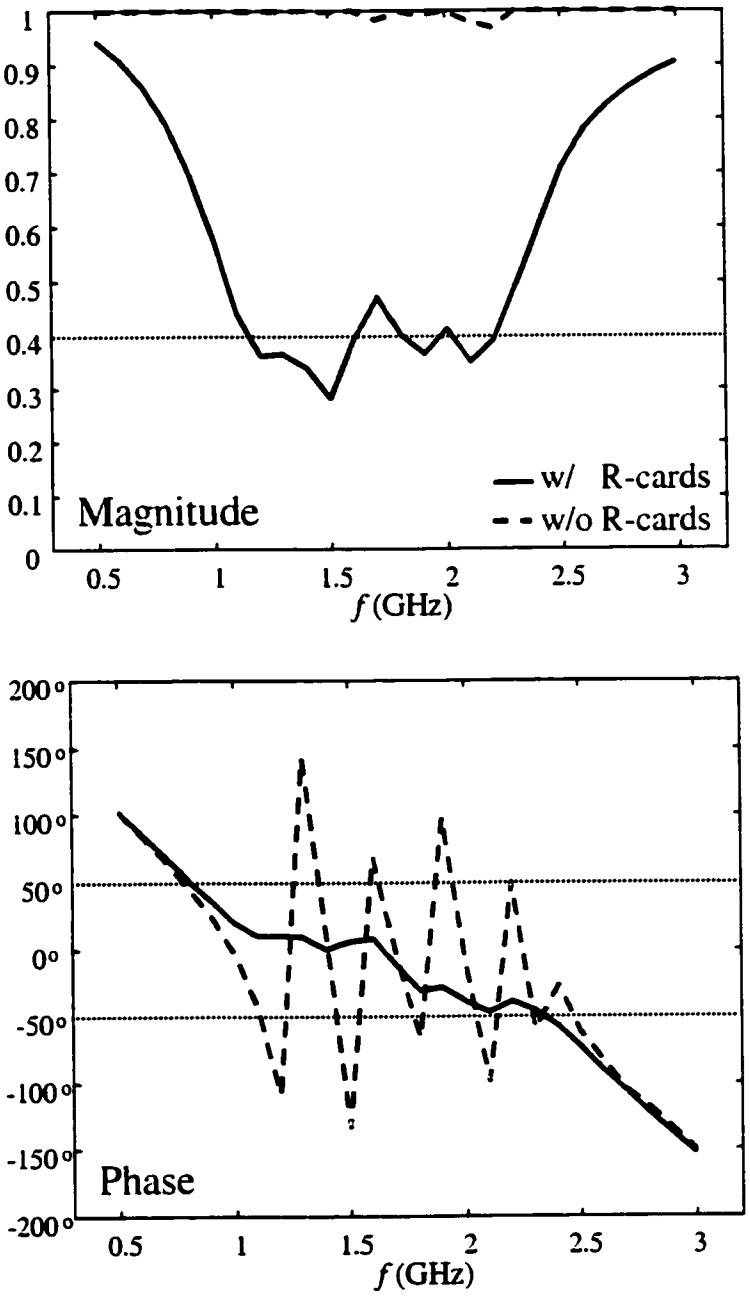

Figure 3.8: Reflection coefficient of the three-layer FSS structure with and without resistive loading.

Novel FSS Element: "Fan" Element FSS

To achieve broadband operation for reconfigurable arrays, the emphasis must be on the phase control of the substrate reflection coefficient. Above, we demonstrated that a three-layer dipole FSS can achieve a fairly flat phase response from about 0.8 to 2.3 GHz. Of interest in this section is to minimize the FSS thickness (possibly using a single FSS layer) and to further ensure that the phase response is maintained at $|\text{phase}(\Gamma)| < 50^{\circ}$. The choice of FSS elements therefore plays a crucial role since these elements must also be broadband to minimize the thickness of the FSS. Towards achieving this goal, various shapes of printed FSS elements were investigated using the full-wave simulator, and some of these broadband elements, namely, crossed dipole, loaded loop and fan, are shown in Figure 3.9. Reflection characteristics of these elements are also displayed in Figure 3.10. In particular, the displayed fan element in Figure 3.9 was found quite attractive in terms of magnitude bandwidth and phase response (see Figure 3.10(c)). This fan element can be thought as a combination of a loop and dipoles. By tuning the lengths of the dipoles (legs) and the inner radius of the loop, we can control the resonance behavior of the FSS.

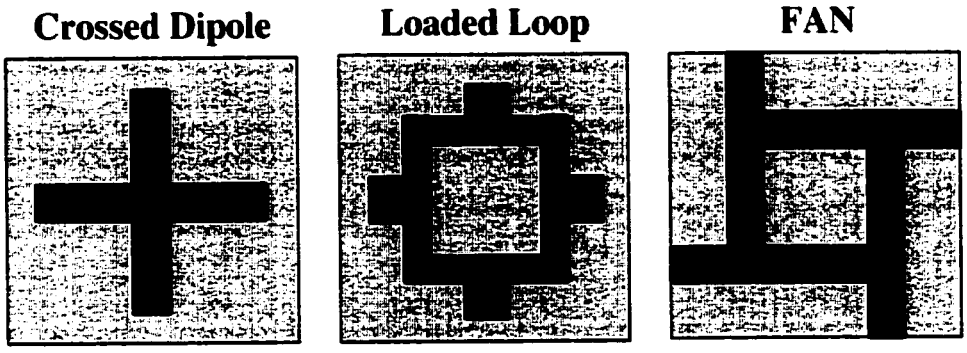

Figure 3.9: FSS elements investigated as candidates for broadband reflection.

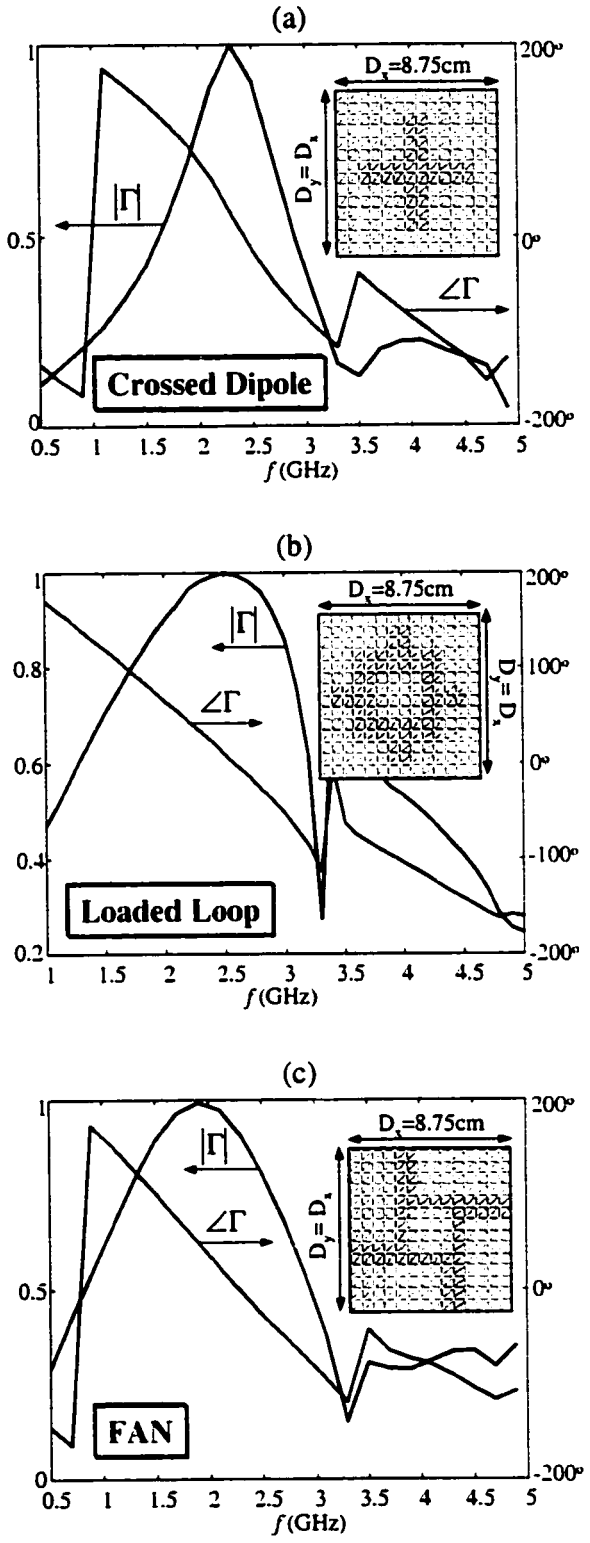

Figure 3.10: Reflection coefficient characteristics of the examined FSS elements; (a) crossed dipole, (b) loaded loop, (c) fan.

We also examined relations between element parameters and FSS response, and considered coupling effects. It was found that bandwidth is enhanced when the FSS elements are brought close to each other within the same FSS layer. In addition, as expected, loaded elements yield broader bandwidths (see Figure 3.10). Also, one could compromise between the individual FSS bandwidth and number of FSS layers included in the design.

Once the FSS element is chosen, the desired response can then be synthesized by increasing the number of FSS layers and varying their separation. In particular, two layers of the fan element FSS provide broadband reflection with unit amplitude over three octaves as seen in Figure 3.11. Also, its phase response is not as oscillatory as that of the dipole. Because of this behavior, the fan element is a preferred choice for a thin, broadband FSS. Previously, it was also demonstrated that optimizing the resistive loading provides improved FSS phase performance. Relatively flat phase (+/-50°) can be achieved by reducing the reflected power (a loss of 3dB or so) for an acceptable operation. In light of these observations, we designed a single layer, resistive fan element FSS to achieve the design criteria for the reflection coefficient. The configuration and unit cell geometry of this novel FSS are shown in Figure 3.12, and the corresponding response is displayed in Figure 3.13. As seen, a relatively flat-phase response is obtained over the whole band using only one layer of the resistive fan element FSS.

In the next chapter, we consider the performance of a reconfigurable dipole array where the designed fan FSS in Figure 3.12 is used as the substrate.

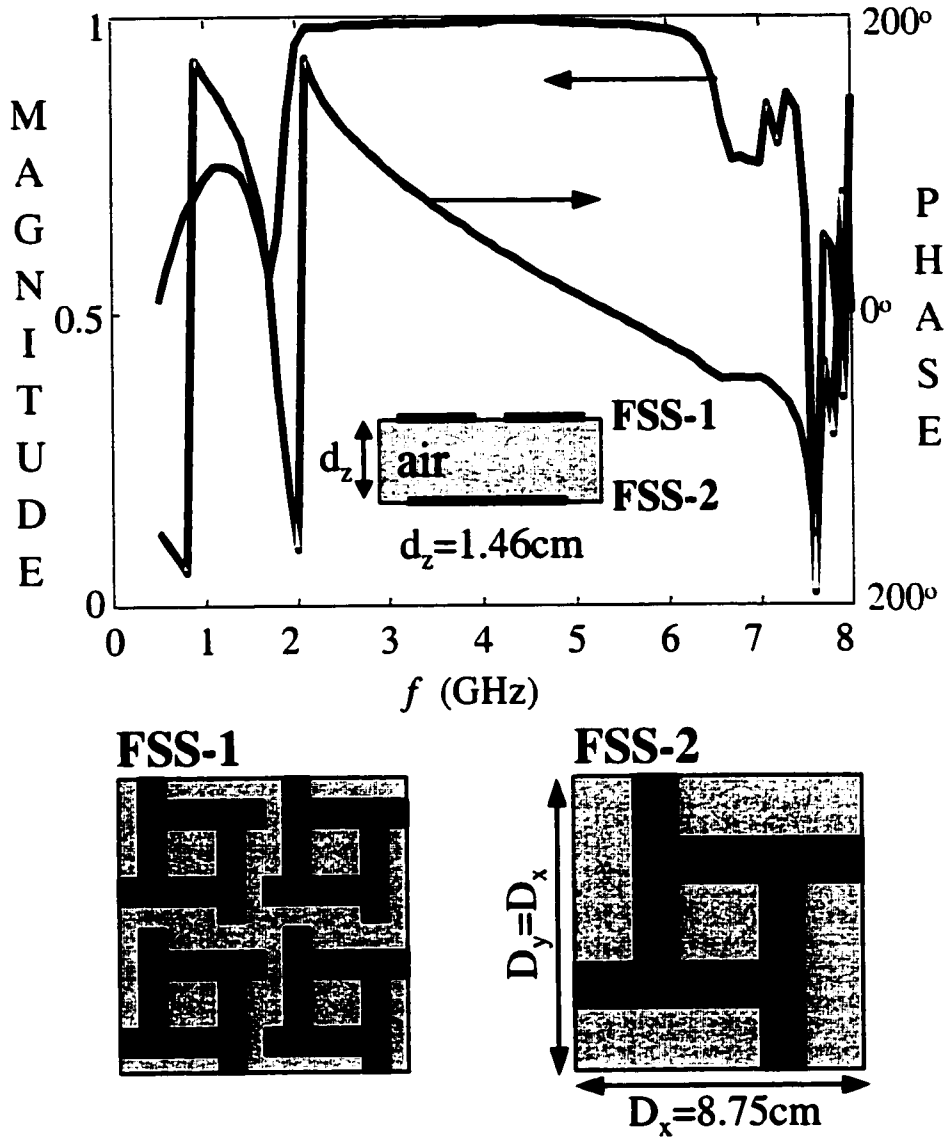

Figure 3.11: Reflection coefficient of the two-layer fan element FSS.

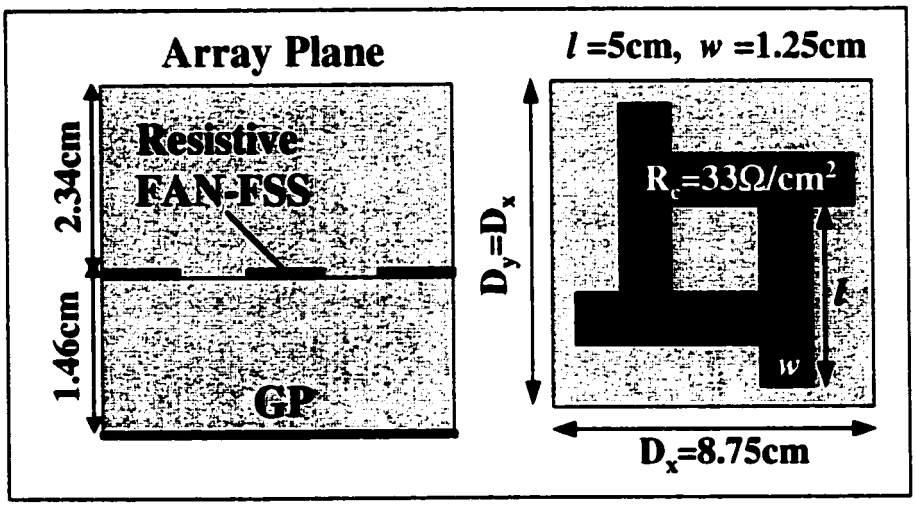

Figure 3.12: Configuration and unit cell geometry of the designed single layer resistive fan element FSS.

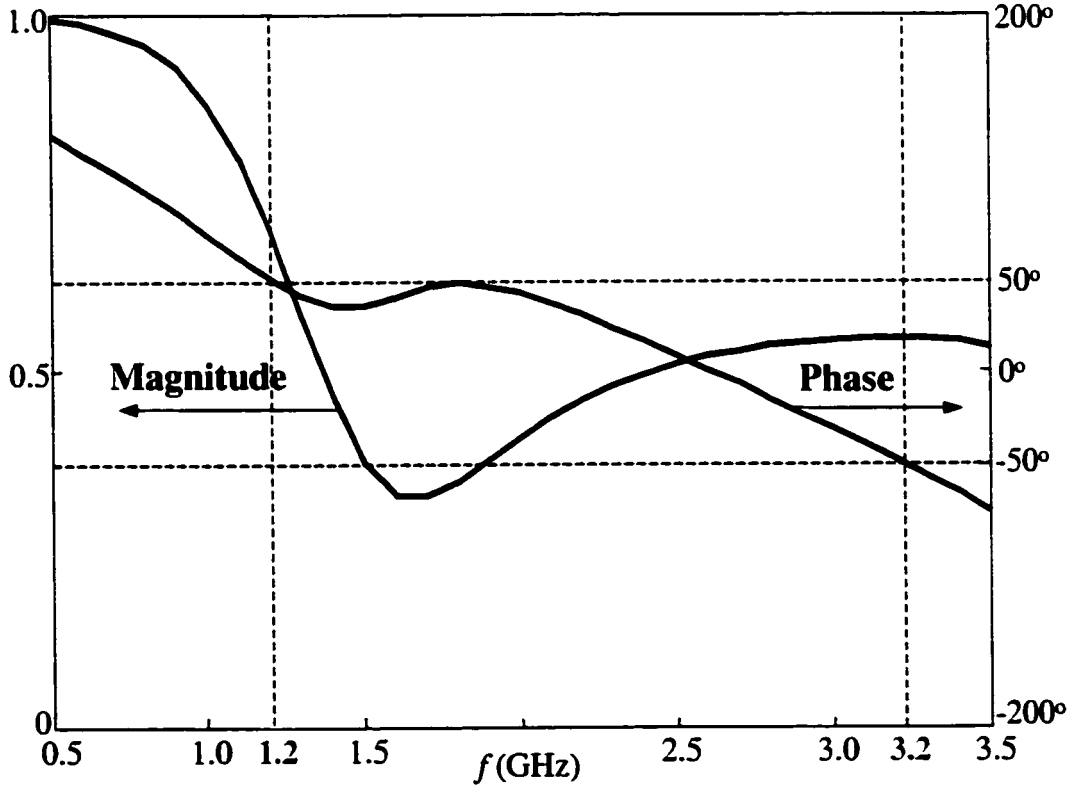

Figure 3.13: Reflection coefficient of the resistive fan element FSS.

CHAPTER 4

RECONFIGURABLE PRINTED DIPOLE ARRAY ON AN FSS SUBSTRATE

Here we consider the performance of a reconfigurable dipole array placed over the fan element FSS substrate introduced in the previous chapter (see Figure 3.12). The unit cell configuration of the dipole array over the fan-FSS substrate is depicted in Figure 4.1. Note that this is a non-commensurate configuration because the unit cell periodicities of the array and the FSS layer are not the same. The dimensions as well as the location of the FSS substrate remain the same during array reconfiguration. In practice, the reconfiguration of the array elements is accomplished by using PIN diodes or MEMS switches. Here these devices are modeled as on/off switches by means of a metallic pad across the gap formed by the switch.

In this chapter, we demonstrate the bandwidth and gain enhancement of a dipole array achieved by using the designed FSS substrate. The overall array performance will also be demonstrated when the array reconfiguration takes place by means of switches. Note that the presented results were obtained by using the infinite array simulator discussed in the Appendix.

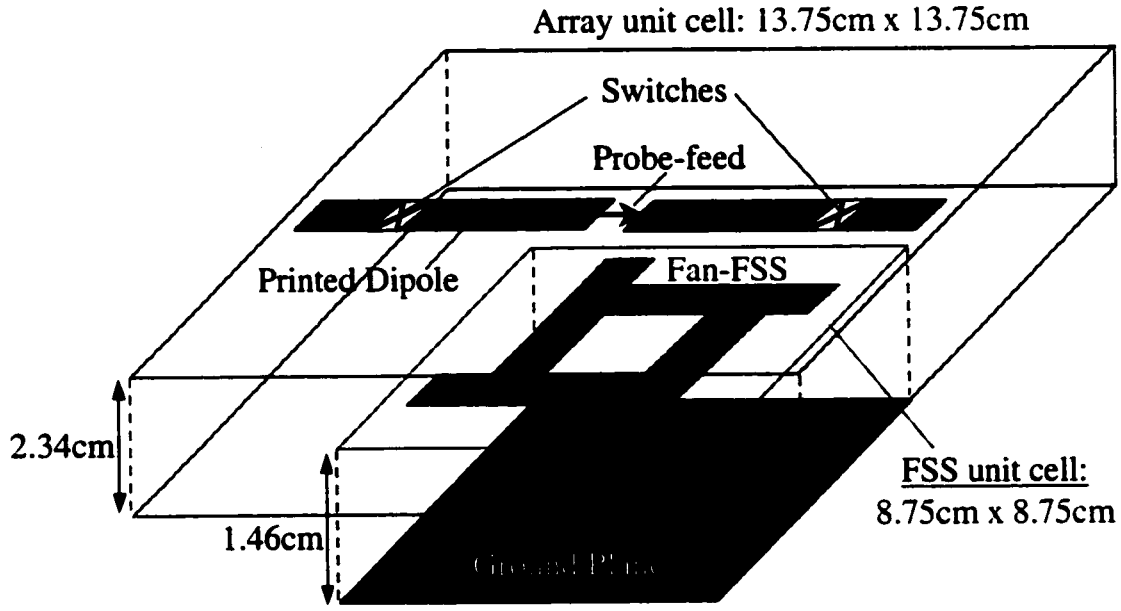

Figure 4.1: Unit cell geometry of the non-commensurate dipole array/fan-FSS substrate configuration.

Bandwidth & Gain Performance

We first demonstrate the improved bandwidth achieved for a dipole array in the presence of the fan element FSS (see Figure 4.1). The unit cell geometry of the dipole array is shown in Figure 4.2 and the FSS unit cell is the same as that shown in Figure 3.12. In Figure 4.3, we display the broadside scanning input impedance[1] characteristics of the dipole array with and without the presence of the FSS substrate. As seen, a remarkable 2:1 impedance bandwidth is achieved by inclusion of the FSS substrate. This bandwidth improvement is quite impressive when compared to the typical 5% bandwidth of a free-standing dipole. This enhancement is due to the relatively flat phase behavior of the fan element FSS. Since the phase is maintained near zero degrees, the FSS serves to emulate a magnetic GP. As such, the reflected field arrives in congruence with the direct (upper half space) dipole radiated field without a resort to the typical quarter wavelength distance between the dipole and GP.

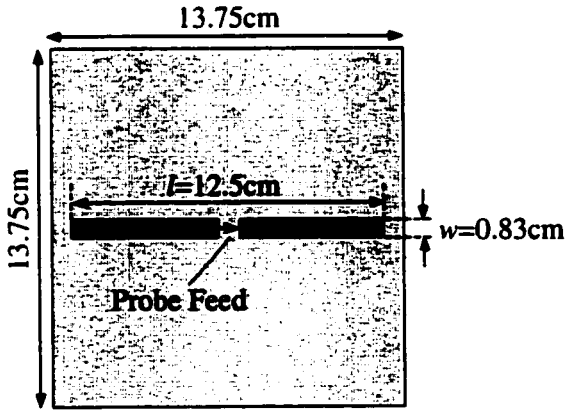

Figure 4.2: Unit cell geometry of the dipole array placed over the fan-FSS substrate.

[1] When a constant excitation current (voltage) is applied to each array element with the element phases adjusted to provide the desired scan angle, the impedance of an element is called "scan impedance" [33].

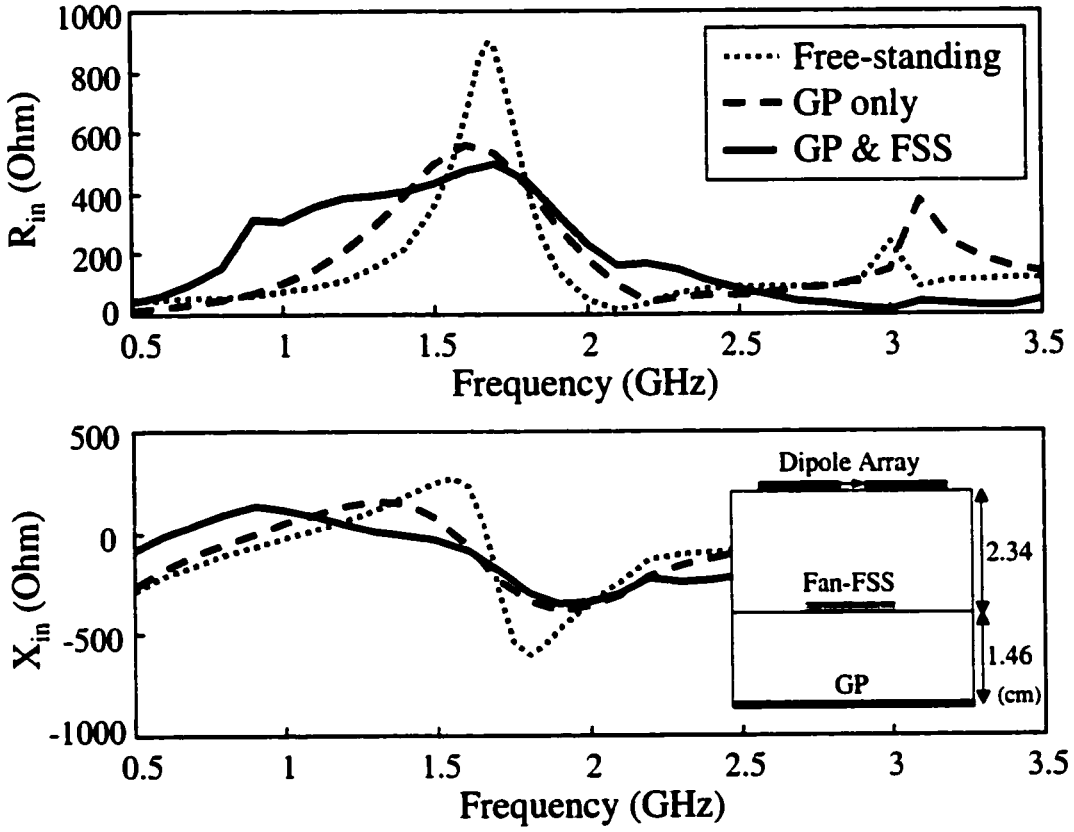

Figure 4.3: Broadside scanning input impedance ($Z_{in}=R_{in}+jX_{in}$) of the dipole array for three cases: the free-standing array, the array backed by GP, and the array over the fan-FSS and GP.

To demonstrate the enhanced radiation performance of the dipole array over the fan-FSS, we calculated the E-plane radiation patterns at different frequencies as shown in Figure 4.4. Note that these patterns were obtained by integrating the aperture currents over the unit cell. We observe that the FSS-GP provides significant improvement in radiation performance as compared to the purely metallic GP. Also, broadband radiation patterns are attained by using the FSS substrate.

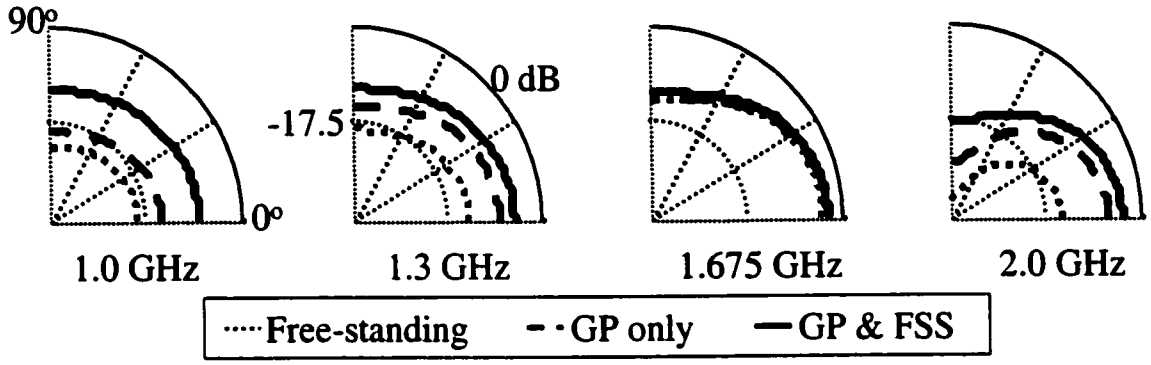

Figure 4.4: E-plane radiation patterns of the dipole array at broadside (zero degrees refers to broadside).

In addition to the bandwidth, we also computed the overall gain per unit cell of the dipole array with and without the presence of the FSS, as displayed in Figure 4.5. The overall gain-measure considered here includes the relative gain (P_{rad}/P_{in}), directive gain (D_0), and mismatch efficiency factor ($1-|\Gamma|^2$), where P_{rad}/unit cell is obtained by integrating the aperture currents over the unit cell. The formulae to compute the gain are given in Table 4.1 where the reference impedance Z_{ref} is the real part of the mean value of input impedances (in presence of the FSS; see Figure 4.3, solid line) over the frequency band of 0.8-2.0 GHz. As can be seen from Figure 4.5, a remarkable 4-22 dB gain

enhancement is achieved over the band of 0.8-3.0 GHz by means of the FSS-GP as compared to the free-standing array configuration (despite the lossy FSS). In particular, a 4 dB improvement in gain occurs at the frequency of 1.675 GHz where the stand-alone dipole resonates (see Figure 4.3). On the other hand, more than a 20 dB gain enhancement is achieved away from the resonance where a maximum impedance mismatch occurs around 2.2 GHz, resulting in a dip in the gain profile as seen in Figure 4.5. The FSS substrate also provides a higher gain profile (1-9 dB more) as compared to the GP-only case over the whole band. Similarly, a 1 dB gain improvement is observed at the resonance, and a 9 dB enhancement is attained after the resonance where a maximum mismatch occurs for the dipole/GP structure. At this point, one may ask whether the same performance could be achieved using a multilayered lossy dielectric above a GP instead. The multilayered lossy configuration will however lead to higher losses and to a much thicker ground plane.

$\text{Overall Gain}: G_0 = e_m\left(\frac{P_{rad}}{P_{in}}\right)(D_0)$	$\Gamma = \frac{Z_{in} - Z_{ref}}{Z_{in} + Z_{ref}}, Z_{ref} = 330\Omega$
$\text{Directive Gain}: D_0 = 4\pi\frac{U_{\max}}{P_{rad}}$	$P_{in} = \frac{1}{2}\lvert I\rvert^2 R_{in}, Z_{in} = R_{in} + jX_{in}$
$\text{Mismatch Efficiency}: e_m = (1-\lvert\Gamma\rvert^2)$	$P_{rad} = \int_0^{2\pi}\int_0^{\pi/2} U(\theta,\phi)\sin\theta\, d\theta d\phi$
	$U(\theta,\phi) \equiv \frac{1}{2\eta}\left[\lvert E_\theta(\theta,\phi)\rvert^2 + \lvert E_\phi(\theta,\phi)\rvert^2\right]$

Table 4.1: Formulae used to compute the overall gain/unit cell.

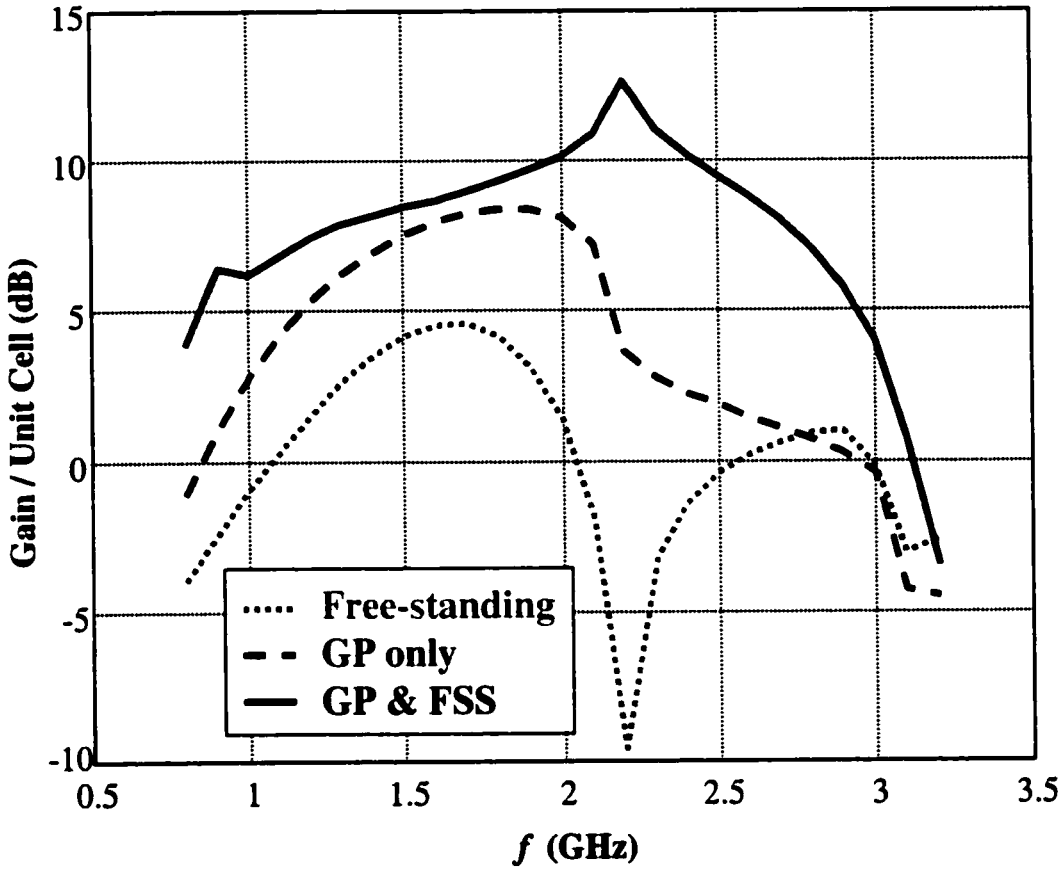

Figure 4.5: Overall gain per unit cell of the dipole array with and without presence of the FSS substrate.

Reconfiguration

In this section, we demonstrate the reconfigurable dipole array performance over the FSS substrate. The dipole length is altered using switches to operate at a different band without a need to change the FSS design which serves as a broadband substrate. The reconfiguration of dipoles is depicted in Figure 4.6 and the frequency band of interest is 0.8-3.2 GHz. When the switch is on, the dipole length becomes λ/2 at 1.2 GHz (low-band operation). When the switch is set at the off–state (open), the dipole length reduces to λ/2 at 2.0 GHz, thus forming the high-band configuration. In this case, besides the excited dipole, the remaining unconnected sections of the dipole are kept in the analysis and they act as parasitic elements.

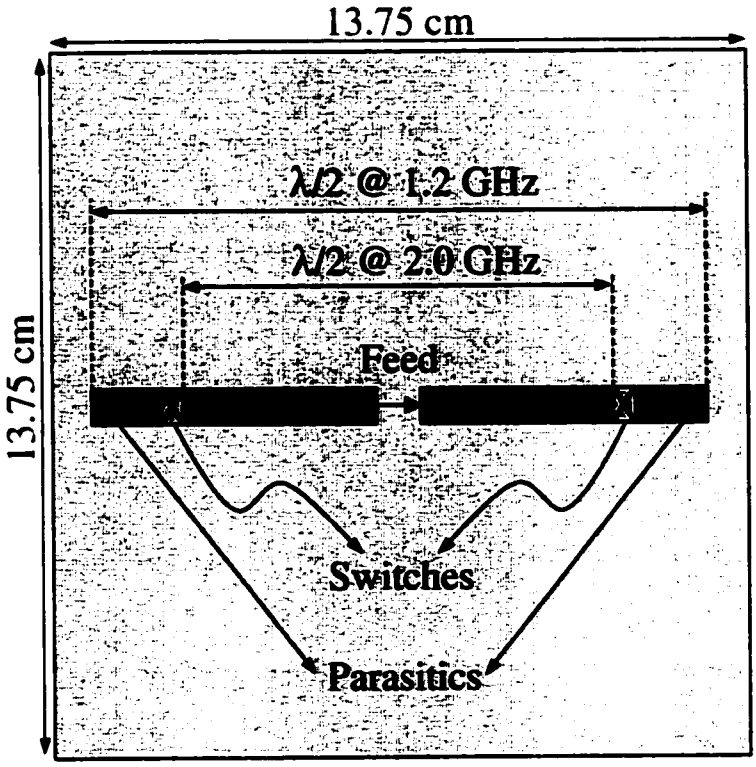

Figure 4.6: Unit cell geometry of the reconfigurable dipole array.

In the previous section, we demonstrated enhanced bandwidth and gain performance of a dipole array over the FSS substrate. In fact, the dipole array considered then (see Figure 4.2) had exactly the same configuration as the low-band configuration shown in Figure 4.6 when the switches are closed. For the high-band configuration, the switches are now opened and the dipole length is shortened. Besides the fed-dipole, we now have parasitic strips present in the array plane, but these only cause a slight shift in the frequency response which can be accounted for in the design, and is furthermore not of concern due to the broader bandwidth of the array. In Figure 4.7, the input impedance characteristics of the dipole array are displayed for the high-band configuration as well as the low-band. As seen, the reconfigurable dipole array over the resistively loaded fan element FSS performs quite well over the entire 800 to 3200 MHz band. The broadside impedance of the array is maintained at about 330Ω over this band and this is demonstrated in Figure 4.7. Note, however, that the location and dimensions of the FSS are kept the same (see Figure 4.1) for both low and high band operations. In addition, in Figure 4.8, the E-plane radiation patterns for broadside scanning at different frequencies are displayed for the reconfigurable array, showing the broadband radiation performance. The overall gain (per unit cell) of the reconfigurable array is displayed in Figure 4.9. As seen, the reconfigurable dipole array above the FSS substrate demonstrated an efficient performance over a broad set of frequencies.

In this chapter, we demonstrated the bandwidth and gain enhancement of a reconfigurable dipole array by means of the designed FSS substrate. The presented results were obtained by using the infinite array simulator which is well validated for printed dipole structures. Therefore, measurements were not needed as additional

validation. In the next chapter, the FSS substrate is extended to slot arrays, and slot array/FSS substrate designs are considered in the rest of the dissertation. Since less reference data are available in the case of slot arrays, measurements were carried out for a designed slot/FSS configuration for validation purposes.

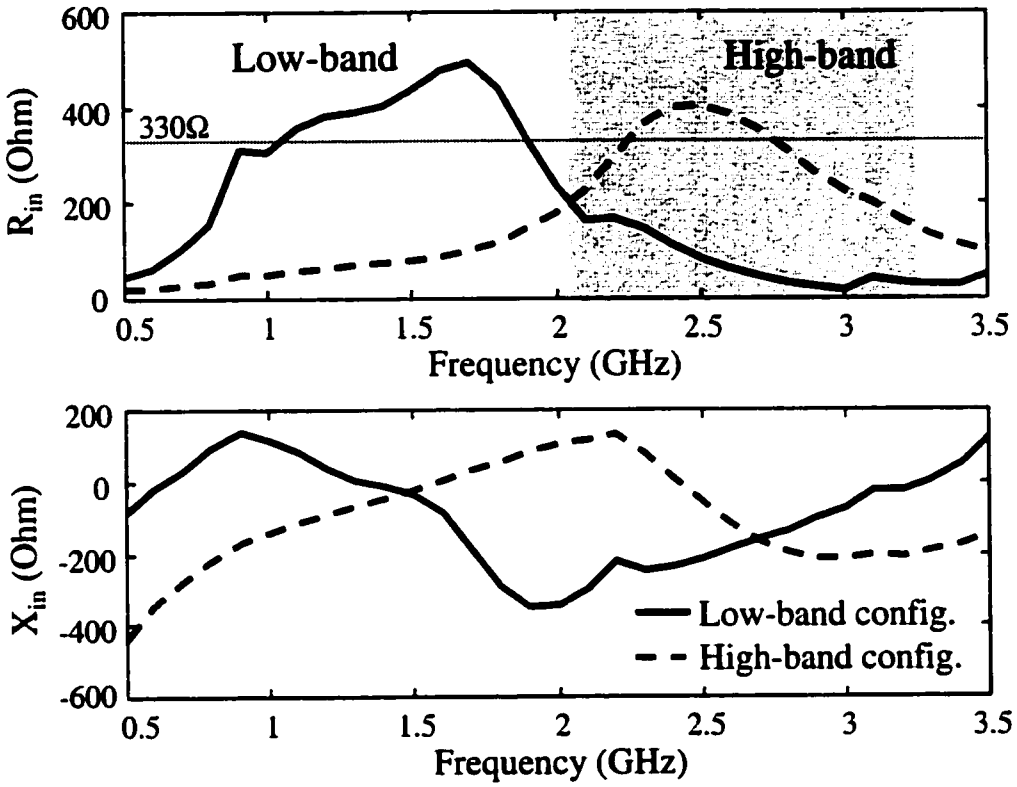

Figure 4.7: Input impedance ($Z_{in}=R_{in}+jX_{in}$) of the reconfigurable dipole array over the resistively loaded fan element FSS.

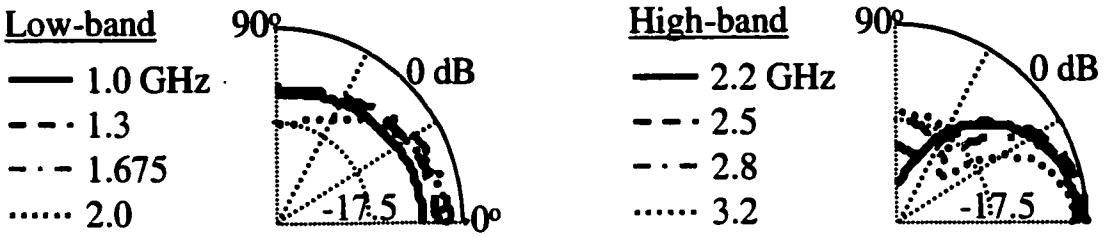

Figure 4.8: E-plane radiation patterns of the reconfigurable dipole array at broadside.

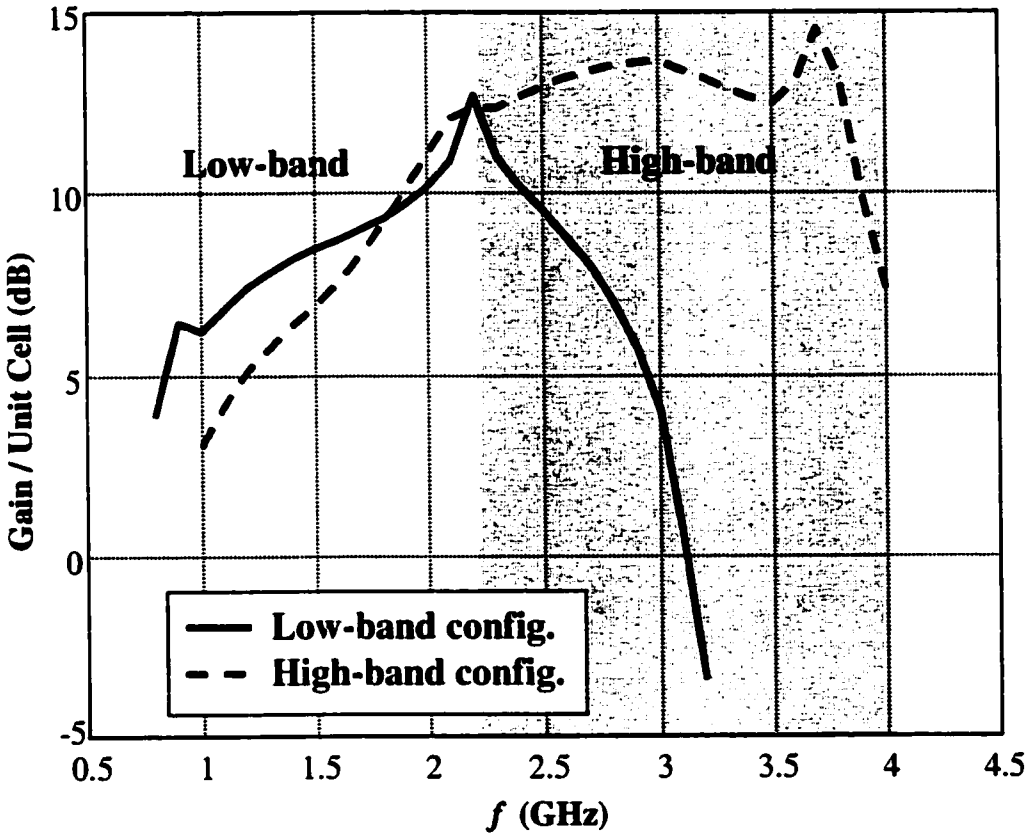

Figure 4.9: Overall gain per unit cell of the reconfigurable dipole array over the FSS substrate.

CHAPTER 5

SLOT ARRAY ON AN FSS SUBSTRATE

In the previous chapter, we demonstrated the performance of a printed dipole array over an FSS substrate consisting of fan-like elements. This FSS substrate was shown to provide broadband array performance for dipoles. Here the FSS substrate is extended to slot arrays as depicted in Figure 5.1. The FSS substrate previously used for the dipoles is further optimized to obtain broadband performance for the slots. The modified FSS still provides a nearly constant phase response but at a phase other than zero degrees. For the slot array, because of the higher order reflections within the cavity below the aperture, the most of the reflected power is consumed within the cavity (see Figure 5.2). As a result, although the FSS substrate provides bandwidth enhancement for slots, the overall efficiency is degraded more than that of the dipoles. Thus, an additional goal is to minimize this efficiency loss. It will be shown that the slot array efficiency can be improved by compromising impedance bandwidth.

In this chapter we first demonstrate bandwidth enhancement for slots with an FSS substrate and then examine effects associated the FSS parameters (resistive loading, orientation, location within the cavity) on the bandwidth performance. Finally, the overall gain performance of the slot/FSS configuration is examined and it is shown that by optimizing the FSS parameters, the overall efficiency can be improved at the expense of the bandwidth.

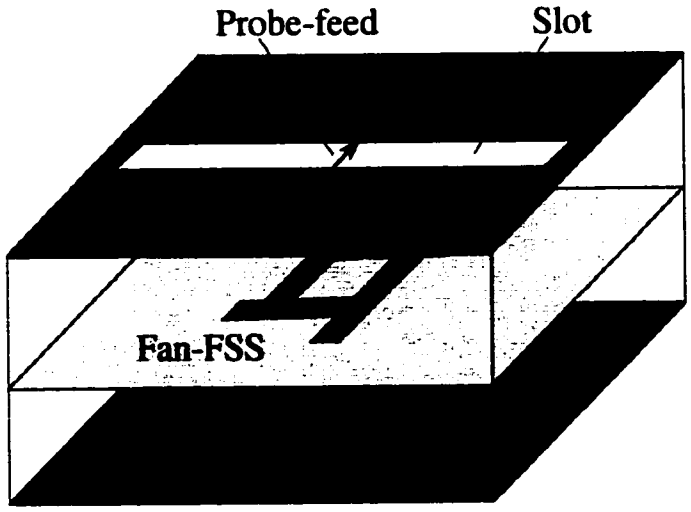

Figure 5.1: Unit cell geometry of the slot array/fan-FSS configuration.

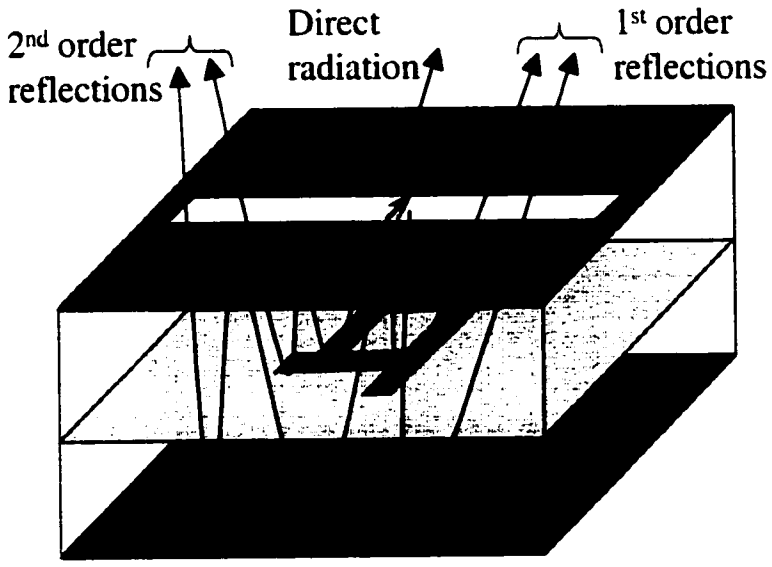

Figure 5.2: Radiation mechanism of the slot/FSS substrate configuration.

Bandwidth Enhancement

In this section, we present the FSS design to be used as an artificial substrate for a planar slot array. To achieve broadband operation for a cavity-backed antenna system, the goal is to achieve a constant phase response for the FSS substrate reflection coefficient. Previously, a constant-phase FSS substrate was designed to achieve a 2:1 bandwidth for a dipole. Here we employ a similar FSS substrate as displayed in Figure 5.3 to achieve bandwidth enhancement for slots. In our design process, we optimized the parameters of the fan as well as cavity depth and separation between the FSS and the slot (Figure 5.3). Both the slot array and the FSS are supported by a thin layer of FR4 material for practical purposes. The analysis and design of the slot/FSS configuration was carried out by means of the infinite array simulator discussed in the Appendix.

As seen from the simulation results in Figure 5.4, the slot array with the resistive fan-FSS configuration provides a remarkable 2:1 slot bandwidth (a constant impedance bandwidth) as compared to the highly resonant impedance characteristics of the isolated slot (< 5% bandwidth) in the absence of the loaded FSS substrate. In Figure 5.4, we also display "reference data" along with the infinite array simulations for validation purposes. These "reference data" were obtained by means of a well-validated finite array simulator [34], and as seen the agreement between the two curves is excellent. The finite array analysis of the slot/FSS configuration was carried out by modeling the unit cell placed at the center of a metallic cavity whose walls coincided with the periodic cell boundaries. The cavity walls thus served as image boundaries in much the same way as the waveguide simulator.

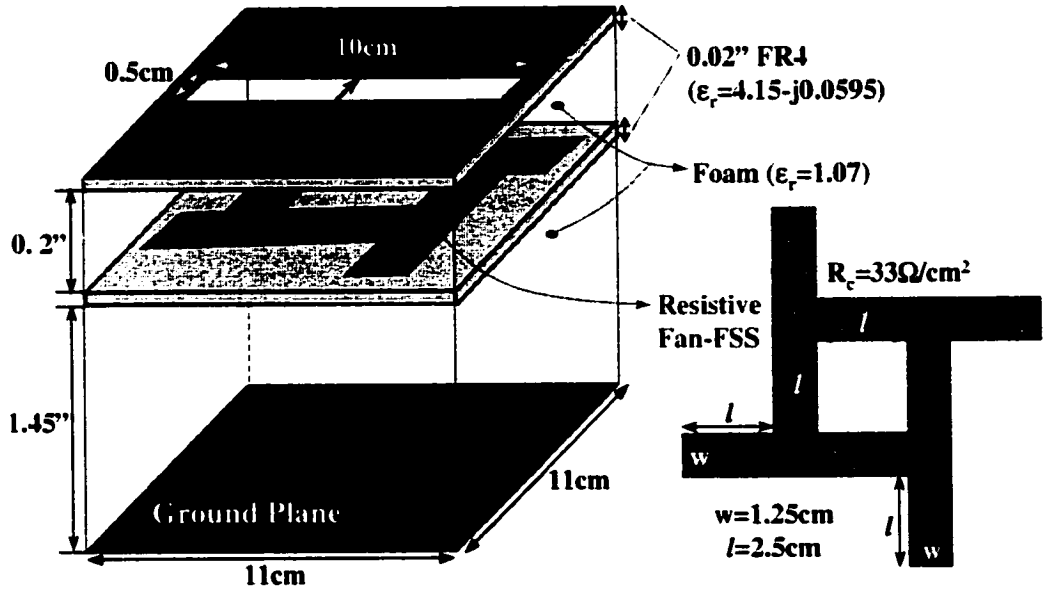

Figure 5.3: Unit cell geometry of the designed slot/fan-FSS configuration.

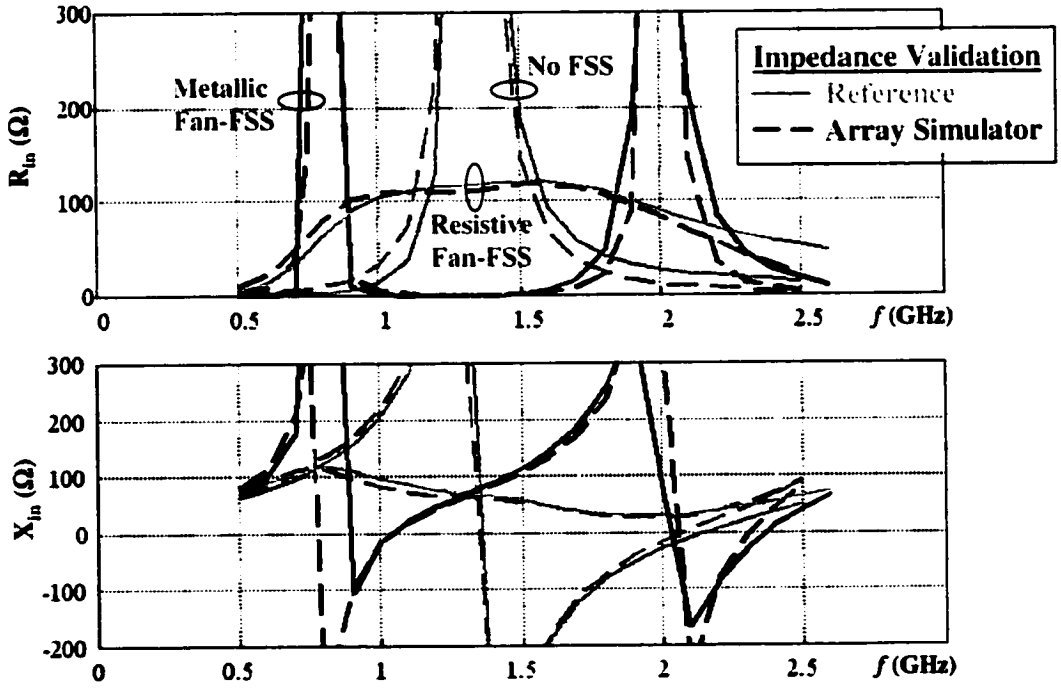

Figure 5.4: Broadside input impedances for the slot/FSS substrate configuration.

Here it is also important to point out the effect of resistive loading on impedance bandwidth. As can be seen from Figure 5.4, the slots with metallic FSS also provide for a highly resonant impedance profile, similar to the response of isolated slots. However, the resistive loading smoothes out these highly mismatched impedances, resulting in almost constant impedance characteristics with a real part of ~115 Ohms over the frequency band of 0.9-1.8GHz. In the next section we show that the resistive loading yields flat-phase reflections (well above zero degrees) at the expense of reducing the magnitude of the reflection coefficient (<0.4).

FSS Parameters and Bandwidth Performance

Resistive loading is a crucial control parameter for achieving a smooth phase response. For a broadband FSS substrate, sharp variations or high oscillations in the phase must be eliminated so that the reflected field from the FSS will have a nearly constant phase response. This can be achieved using resistive cards within the same FSS layer (see Figure 2.7) or using resistively loaded FSS elements (see Figure 5.3). The latter is applied here and the effect of resistive loading and element-orientation on the slot bandwidth is examined along with the slot-to-FSS distance as another parameter for bandwidth control. In particular, the FSS loading and the location of the FSS will later be used as control parameters to improve the gain profile by compromising the bandwidth.

To demonstrate the effect of resistivity on bandwidth performance, we carried out a parametric study of bandwidth versus resistivity (R_c). As seen from Figure 5.5, there is a compromise between loading and bandwidth, and the optimum constant impedance profile over a 2:1 bandwidth is achieved with $R_c=33\Omega/cm^2$. For the resistivity values less or larger than this value, the response deviates from the optimum profile. It is observed

from Figure 5.4 and Figure 5.5 that as the resistivity is increased, the impedance profile approaches that of the isolated slot case where no FSS is present. On the other hand, as the resistivity is lowered, the response moves toward to that of the metallic FSS case where the resistivity is zero, as expected.

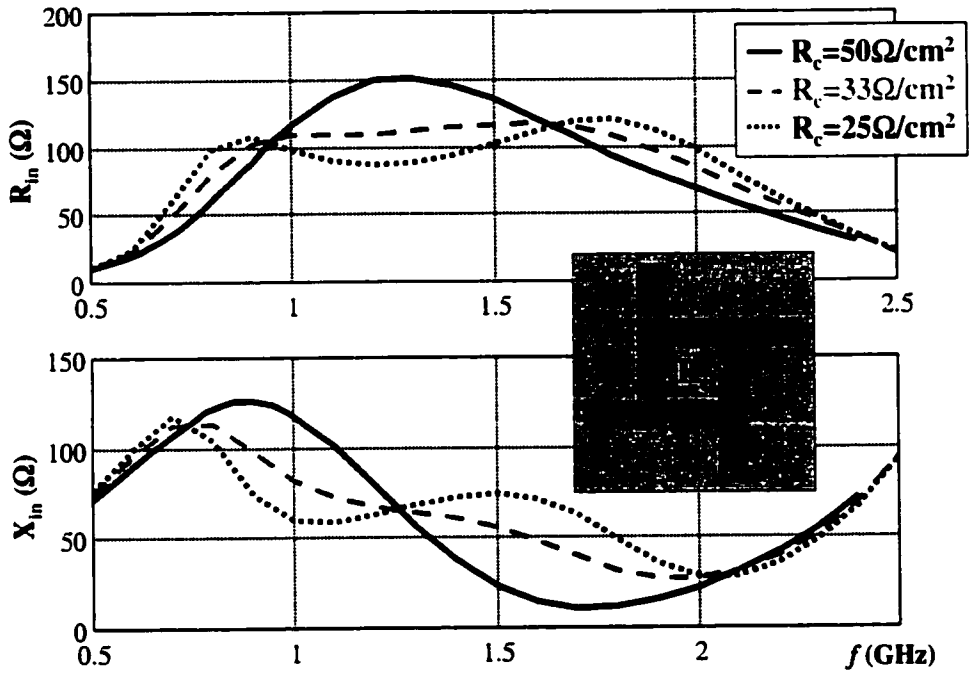

Figure 5.5: Effect of resistive loading on the slot bandwidth.

To better understand the behavior of resistive loading, we considered the FSS/GP structure by itself (without the presence of the slot aperture; see Figure 5.6) and computed the reflection coefficient characteristics (at normal incidence) of the FSS for different loading values. For this study, we kept the location of the FSS fixed with respect to the array plane (d=0.22") and only varied the resistive loading values. Corresponding reflection responses are displayed in Figure 5.7. Also, displayed are the reflections for the metallic FSS and no-FSS (only GP backing) cases. As seen, when there is no FSS

present, the reflection coefficient has a unit magnitude (as expected) with a linear phase response. In fact, the phase remains within the $-50°/+50°$ range over the band 1.1-1.9 GHz. For the metallic FSS (zero resistivity) case, the magnitude remains the same, but the phase now has an oscillating or zigzag response. On the other hand, for the resistively loaded FSS, the amplitude levels become less than 0.4 for the resistivity values less than 100 Ohms/cm^2 over the frequency band of 0.8-2.4 GHz. From the phase responses we observe that as the resistivity increases, the oscillating behavior tends to smooth out and become closer to the linear response of the no-FSS case for higher values. In particular, in case of R_c=50 Ohms/cm^2, the phase is leveled at 50° over the 1-1.5GHz band.

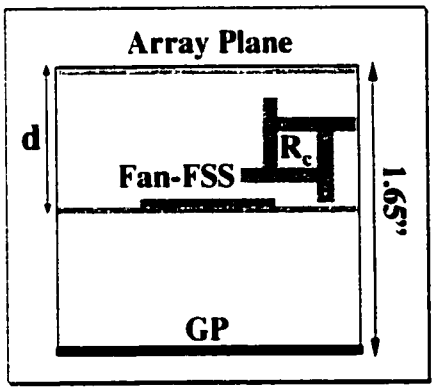

Figure 5.6: Unit cell configuration of the FSS/GP considered for reflection coefficient studies.

We also carried out a parametric study of bandwidth versus the slot-to-FSS separation (d). In Figure 5.8, the slot impedances are displayed for different d values where the resistivity is 33 Ohms/cm^2. The more the separation d is, the less effective the FSS becomes. In fact, the FSS is shorted by the GP as it gets closer to the GP, and this is expected. In Figure 5.9 we display the reflection coefficient responses of the FSS/GP structure for different d values. As seen, the reflection from the FSS/GP approaches that

of the no-FSS case (GP backing only) as the separation is increased, and this is in accordance with the results of Figure 5.8.

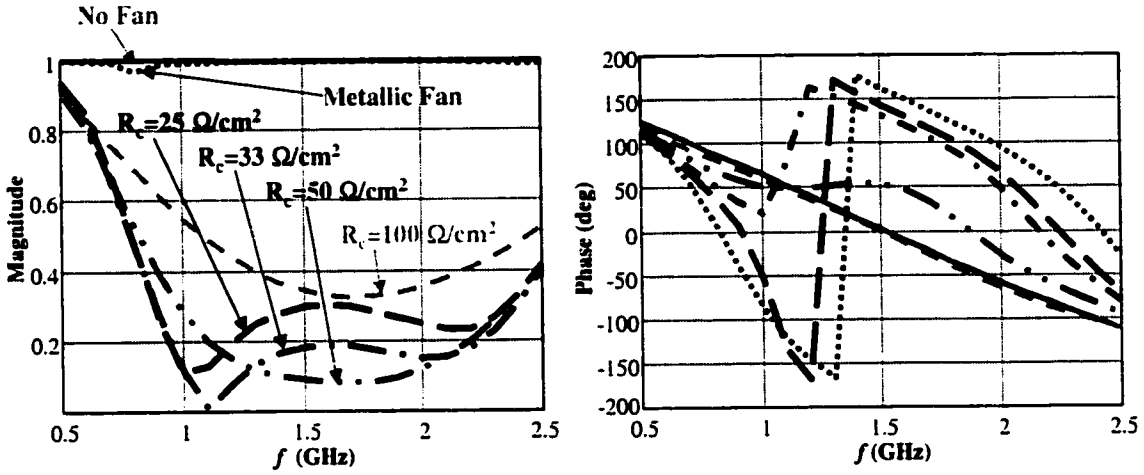

Figure 5.7: Reflection coefficient characteristics of the fan-FSS/GP configuration for different resistive loadings.

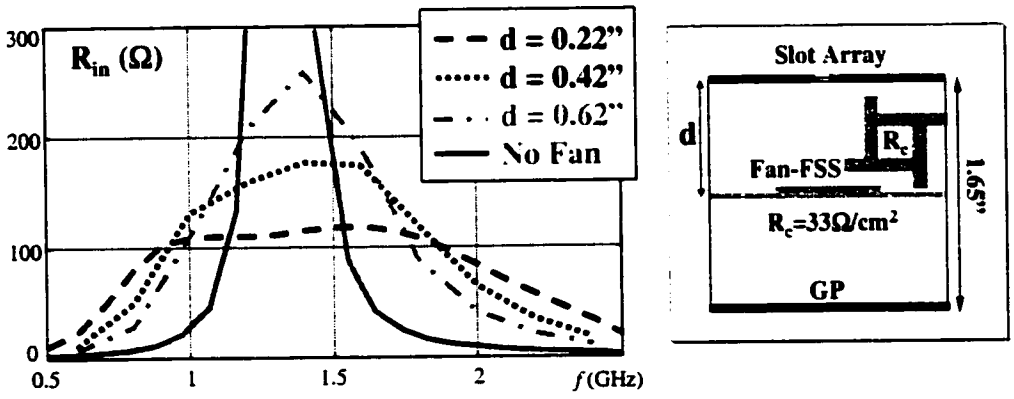

Figure 5.8: Effect of slot-to-FSS distance on the slot bandwidth.

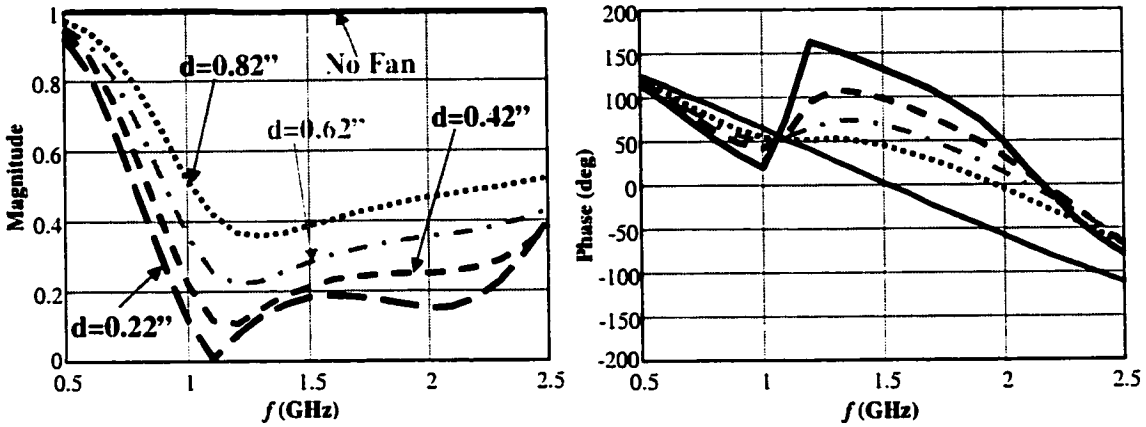

Figure 5.9: Reflection coefficient characteristics of the fan-FSS/GP configuration for different array plane-to-FSS distances.

Furthermore, to facilitate construction of the array and achieve better cell isolation, we also examined situations where the FSS element was rotated at different angles as shown in Figure 5.10. The rotated fan element allows for more flexibility in the practical feed placement (see Figure 6.1). Of importance is that rotation does not cause much deviation from the unrotated FSS performance as displayed in Figure 5.10.

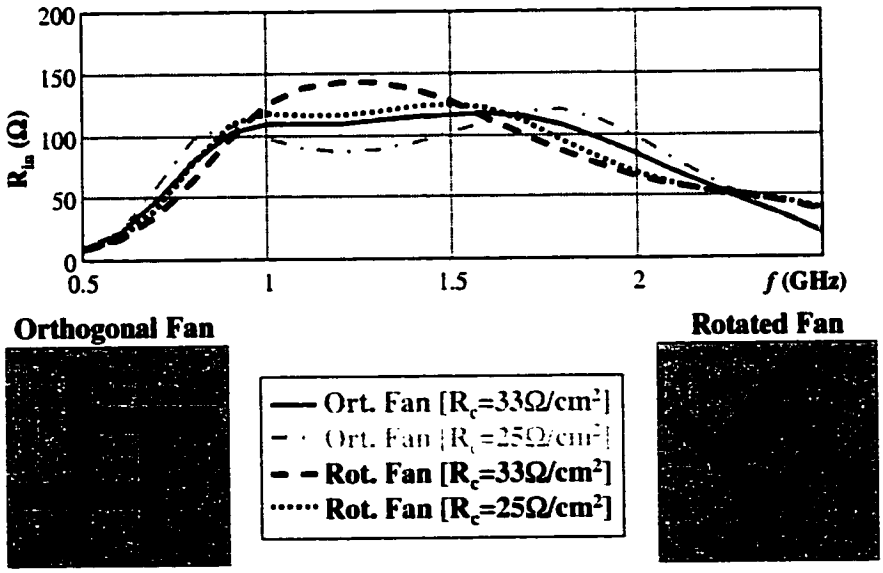

Figure 5.10: Effect of rotating the fan element on the slot bandwidth.

Gain Performance

To assess the gain performance of the proposed slot array/FSS configuration, we computed the overall gain/unit cell as described in Chapter 4 and defined in Table 4.1 with Z_{ref}=100 Ohms. In Figure 5.11, we display the return loss ($|\Gamma|^2$), the mismatch efficiency ($1-|\Gamma|^2$; see Table 4.1), and the overall gain/unit cell for different resistive loadings and different slot-to-FSS separations. It is observed from Figure 5.11 that even though the FSS substrate with resistive fan elements has provided bandwidth enhancement for the slots (see Figure 5.4), it also results in as much as 6 dB loss over the frequency band as compared to the isolated slot case. That is, the gain performance of the isolated slot dominates over that of the slot/FSS configurations. The main reason for this efficiency loss is the higher order reflections taking place within the cavity (see Figure 5.2) where the trapped waves undergo multibounces on the resistive FSS ground plane prior to being escaped from the slot array radiation. These multiple reflections also have different phase characteristics and thus lead to further mismatches of the direct radiated and ground plane reflected fields.

As also seen from the results in Figure 5.11, there is a compromise between the slot bandwidth and gain performance. As previously shown, the bandwidth improvement is degraded when the FSS is placed further away from the slot aperture (see Figure 5.8) The same is observed when the resistivity is less/higher than the optimum value of 33 Ohms/cm^2 (see Figure 5.5). Conversely, the gain performance can be improved by increasing the resistivity R_c or the separation distance d at the expense of bandwidth. Although the optimum bandwidth configuration (see Figure 5.3) provides a 3-6 dB better mismatch efficiency (over the whole band) than the isolated slot, this improvement is

surpassed by much higher power dissipation taking place within the cavity. However, sacrificing the bandwidth for a better gain profile, more efficient slot array/FSS substrate configurations can be realized. In Figure 5.12, we display the characteristics of such configurations with optimum gain profiles along with that of the optimum bandwidth design. As seen, size modification of the FSS element can also serve as a control parameter to achieve optimum gain performance.

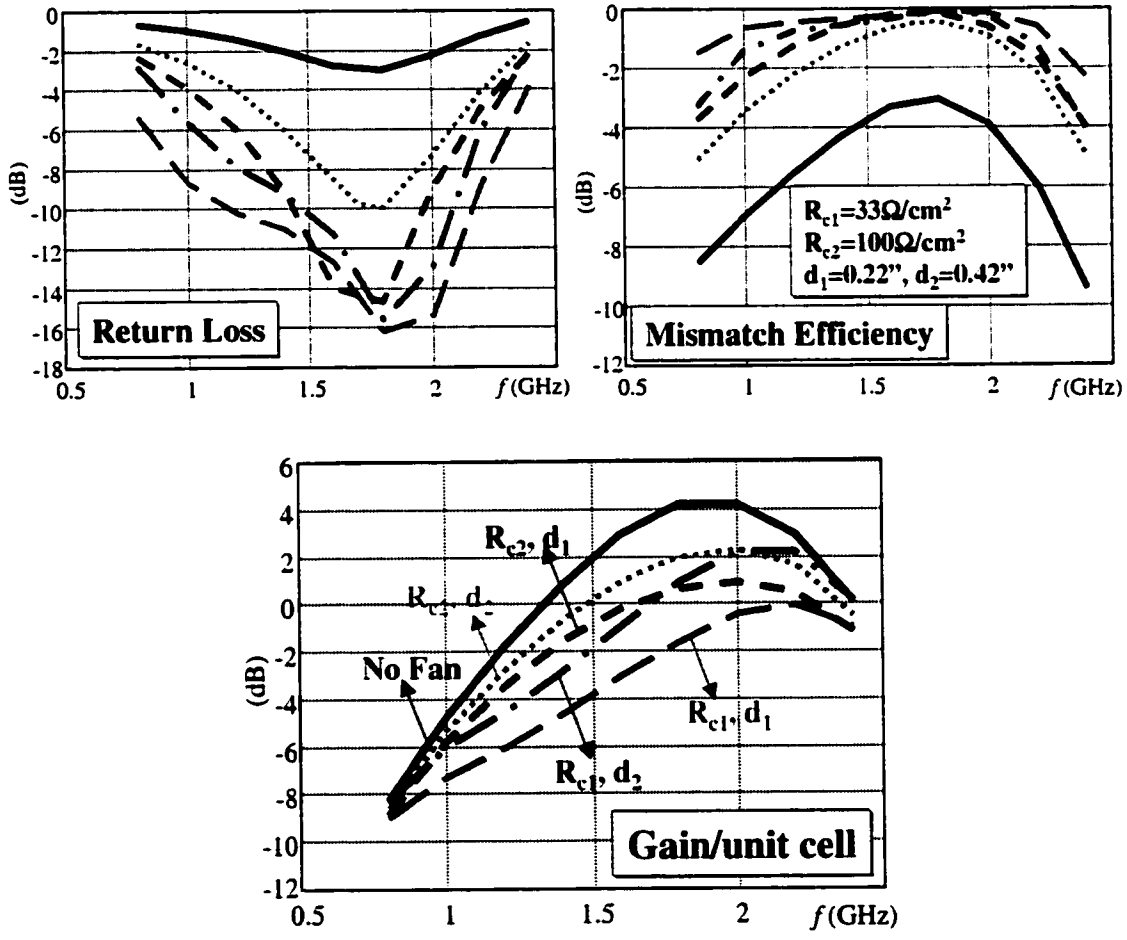

Figure 5.11: Gain versus bandwidth performance of the slot/FSS configuration with respect to resistive loading and the FSS location.

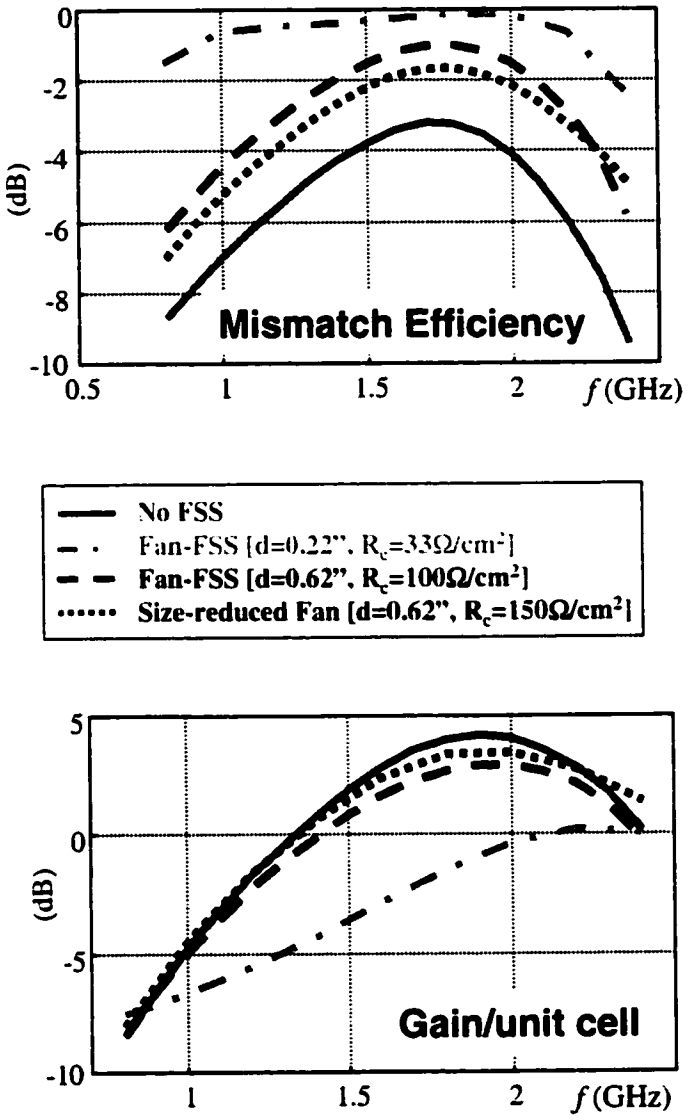

Figure 5.12: Mismatch efficiency and gain characteristics for optimum-gain slot/FSS configurations.

In this chapter, we demonstrated the bandwidth enhancement for the slot arrays by means of the designed FSS substrate at the expense of some gain reduction. To preserve this bandwidth improvement, there is also a need for a broadband balanced/matched feed structure. In the next chapter, the design of such a feed component is presented along with measurements for validation purposes.

CHAPTER 6

BROADBAND BALUN/FEED DESIGN

In the previous chapter, we demonstrated bandwidth enhancement for slot arrays by means of the designed FSS substrate. The cavity-backed substrate consisting of a resistively loaded, fan element FSS provided at least a 2:1 slot bandwidth at the expense of some efficiency losses. In practice, to preserve bandwidth enhancement an equally broadband feed is required. Herewith we introduce a new balun/feed design consisting of a YY microstrip-to-slotline transition in its input port and a tapered slot-line at the output for impedance transformation. The resulting feed configuration shown in Figure 6.1 achieves a 6:1 bandwidth for a VSWR < 3 when terminated with 100-200 Ohms of impedance loads. The design was carried out by using the infinite array simulator and validated with measurements. The final integrated structure incorporating the slot array, FSS substrate and balun/feed in Figure 6.1 was also fabricated and tested to validate the simulations. It will be demonstrated that the proposed slot/FSS/balun configuration provides at least a 2:1 bandwidth.

In this chapter, we also validate our simulated slot/FSS/balun design with measurements. We first consider the design of broadband balun/feed structure. The slot/FSS/balun structure is then constructed to achieve a broadband and matched antenna configuration operating over a 2:1 bandwidth.

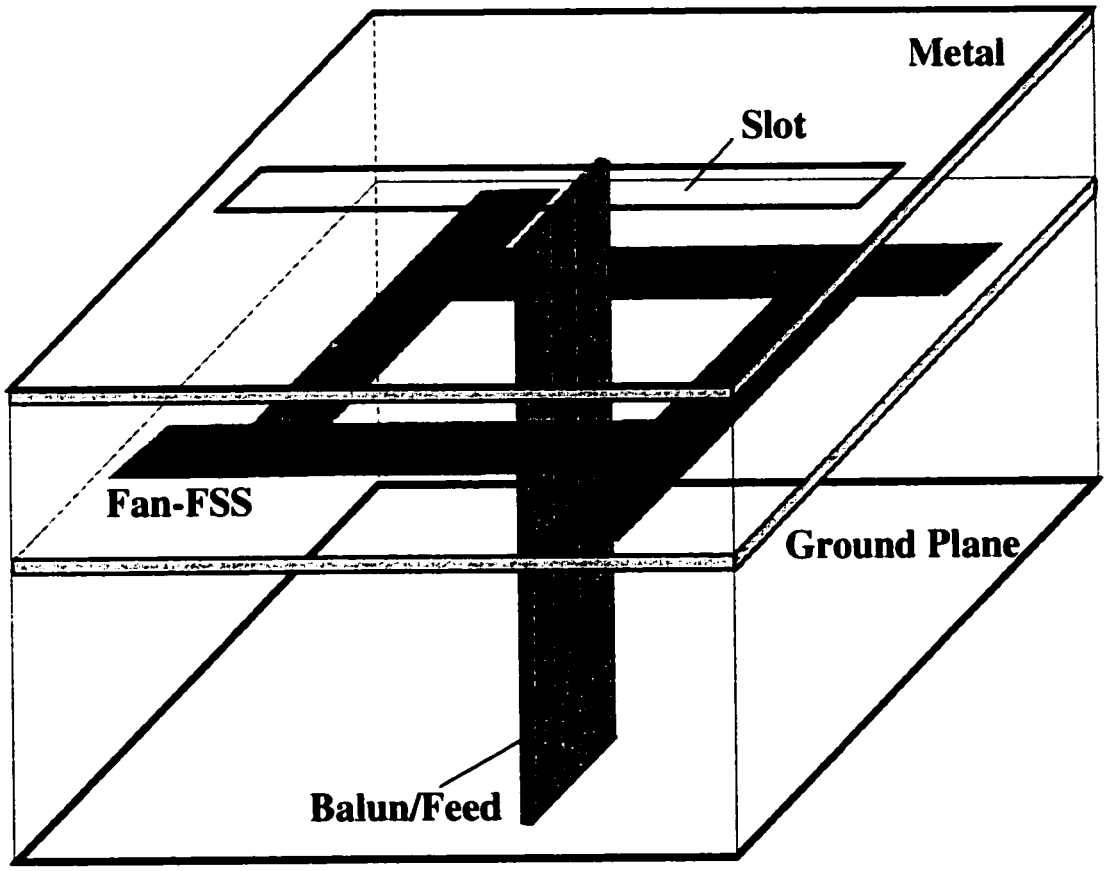

Figure 6.1: Proposed slot/FSS/balun configuration.

Balun/Feed Design

For the slot arrays presented previously, current probe-feeds [35] were used as feeding elements in simulations and placed at the center of the slot elements (see Figure 5.1). However, in practice, a balanced and matched feed is required, and for this purpose a broadband balun/feed is proposed, consisting of an YY microstrip-to-slotline transition with a tapered slot-line (see Figure 6.1). In this section, we present the design procedure for the proposed feed configuration and validate our simulated designs with measurements. Note that balun/feed designs presented here was accomplished by means of the array simulator.

As demonstrated in Chapter 5, a 2:1 slot bandwidth was achieved by means of the FSS substrate. In practice, a broadband balanced/matched feed is required to preserve this bandwidth enhancement. Coaxial cable feeds are usually employed at the front end of practical antenna systems and these are inherently unbalanced feed components. A viable approach to balance such a component is to incorporate a balun[1] structure into the system. Here we consider a YY microstip-to-slotline balun configuration [8], [37] to achieve a balanced feeding for a slot radiator as illustrated in Figure 6.2. We selected this type of balun structure mainly due to its low-loss and broadband performance [8]. Also, its compact planar structure allows for of easy integration with the cavity-backed slot configuration (see Figure 6.1).

---

[1] A balun is a device used to couple a balanced system to an unbalanced system by canceling or choking a leakage current flowing through a path other than the main path of signal transmission [36].

As shown in Figure 6.2, the double-Y balun is supported by a thin dielectric substrate. The microstripline section is placed on one side of the substrate and the slotline section on the other side. In this six-port configuration, the input and output ports are decoupled and a perfect transmission between these two ports are achieved if the junction effects can be neglected and if the characteristic impedances of the strip and slotlines are all the same, e.g., 50Ω [8]. In addition, considering the other four ports of the junction, opposite pairs of lines should have reflection coefficients with opposite phases to attain a balanced system. That is, one pair of lines should be short-circuited and the other one should be open-circuited (see Figure 6.2). Accordingly, the electrical length from the short and open circuits to the center of the junction should be equal, i.e., $\beta_m l_m = \beta_s l_s$ [8]. Here β_m and β_s are the respective wavenumbers for the microstripline and the slotline sections; l_m and l_s are the corresponding distances from the short or open circuit terminations to the center of the junction as depicted in Figure 6.2.

Even though double-Y baluns are all-pass networks in principle, in practice they do not demonstrate characteristics of all-pass networks. This is because the slotline open circuit is usually realized as a circular slotline (see Figure 6.2) which can only provide a 2-3 octave frequency range [37]. Therefore, one of the design goals is to optimize the shape as well as the size of the slotline open circuit to achieve a desired bandwidth performance, which is a 6:1 bandwidth in our case. Another design goal is to achieve an impedance transformation between the input port (50Ω system) and the output port, where the slot aperture is located. The corresponding slot impedances at the aperture level were predicted to be on the order of 100-200 Ohms in case of a slot/FSS configuration (see Figure 5.5 and Figure 5.8). Therefore, the microstripline and slotline

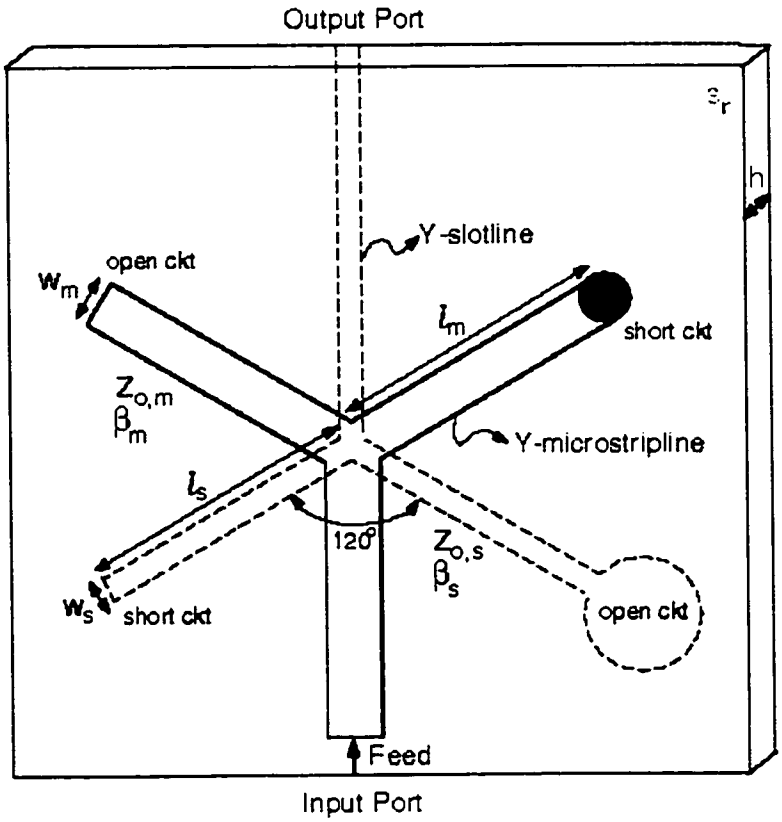

For perfect transmission from the input port to the output port the followings should be satisfied:

$$\beta_m l_m = \beta_s l_s$$

$$\beta_m = \frac{2\pi}{\lambda_{g,m}} \qquad \lambda_{g,m} = \frac{\lambda_o}{\sqrt{\varepsilon_{eff:m}}} \qquad \varepsilon_{eff:m} = \varepsilon_{eff:m}(\varepsilon_r, W_m/h)$$

$$\beta_s = \frac{2\pi}{\lambda_{g,s}} \qquad \lambda_{g,s} = \frac{\lambda_o}{\sqrt{\varepsilon_{eff:s}}} \qquad \varepsilon_{eff:s} = \left\{ \begin{matrix} averaged\ over \\ frequency\ range \end{matrix} \right\} \varepsilon_{eff:s}(\varepsilon_r, W_s, h, \lambda_o)$$

$$Z_{o,m}(\varepsilon_r, W_m/h) = \left\{ \begin{matrix} averaged\ over \\ frequency\ range \end{matrix} \right\} Z_{o,s}(\varepsilon_r, W_s, h, \lambda_o) = 50\ \Omega$$

Figure 6.2: Double Y microstrip-to-slotline balun configuration and governing relations for an ideal balanced system.

parameters (width, length, ε_r) need to be optimized accordingly so that the slot impedance seen at the input port of the balun/feed is close to the matched value (50Ω) as much as possible. Slotline tapering is another control parameter while considering the impedance matching at the input port.

The overall parameter optimization mentioned above is hampered by modeling limitation associated with the array simulator (memory and CPU time). The simulator employs a structured mesh for modeling, and this mesh consists of triangular surface and prismatic volume elements as discussed in the Appendix. Hence, arbitrary geometries (circular or tapered sections) can be modeled only by a stair-case approximation, which may cause inaccurate modeling, especially for the very fine features of the geometry. Furthermore, while modeling those fine features, the memory size of the problem can be dramatically increased to a level that the computational resources cannot handle. As a result of these limitations, we considered a rather approximate design for validation purposes and thus modeling requirements were relaxed. We considered a VSWR < 3 as the design criterion to be met at the balun's input port instead of the standard criterion of VSWR < 2, which corresponds to $|S_{11}| < -10$dB.

Considering those issues, we designed the balun/feed structure depicted in Figure 6.3 by means of the array simulator. In Figure 6.3, both modeled (stair-case approximation) and the actual balun geometries are displayed. As shown, the design employs a slotline which has no tapering. In fact, a linearly tapered slotline could not be modeled accurately with stair-case approximation since this modeling required at least three sections along the slotline length and thus much smaller mesh discretization that was beyond the memory capacity of available computational resources. For the design

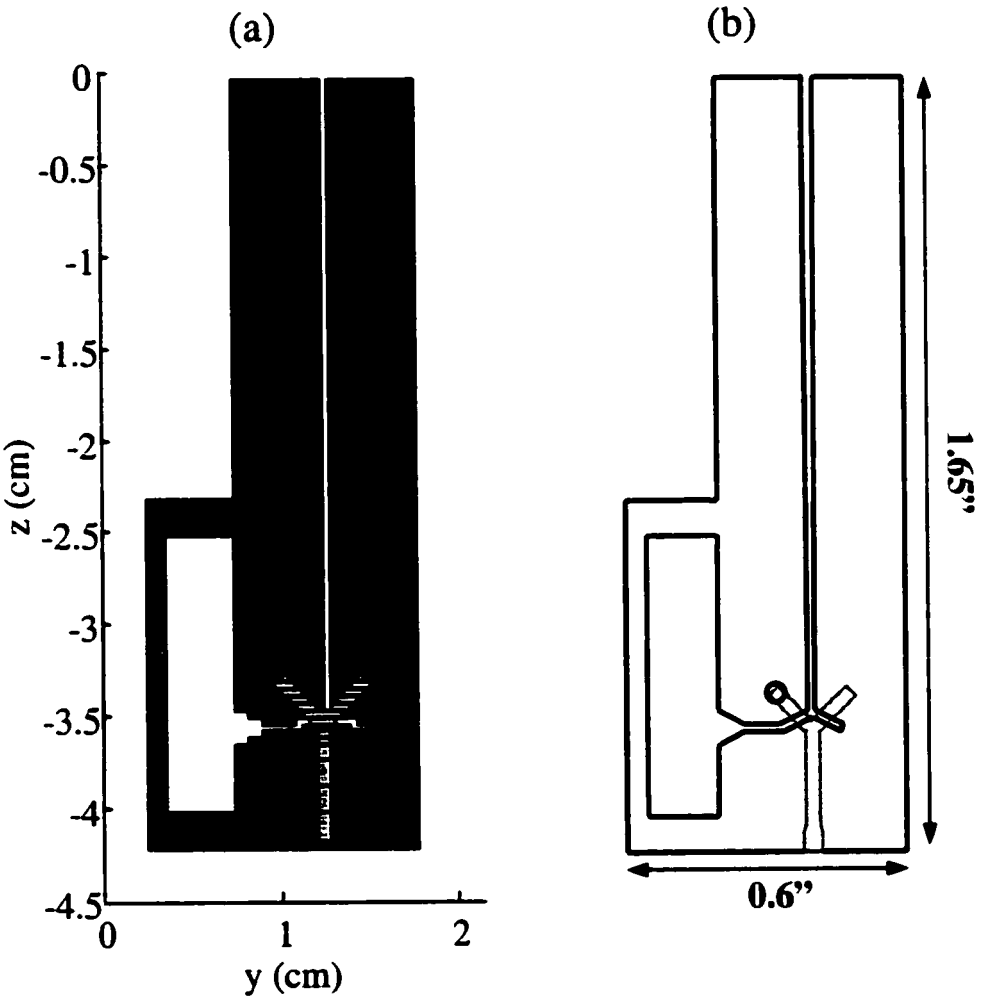

Figure 6.3: Designed balun/feed configuration; (a) modeled geometry, (b) actual geometry.

shown in Figure 6.3, we optimized the microstripline and slotline parameters specified in Figure 6.2 and also optimized the shape and size of the virtual open circuit [38] for the slotline to achieve the design criterion over a broad bandwidth. The rectangular shape was chosen for better incorporation of the balun within the slot/FSS configuration (see Figure 6.1). The balun size, especially the height of the open circuit, was minimized for less interaction with the FSS layer which is cut through for installation of the balun.

The design optimization was carried out by terminating the slotline with various resistive loads of 100–200Ω, representing equivalent slot impedances. The feed was located at the lower-end of the microstripline and input impedance computations were carried out by means of the simulator. The computed VSWR along with the simulated geometry are displayed in Figure 6.4. As seen, the designed balun/feed provides more than a 6:1 bandwidth for VSWR < 3 when terminated with 100Ω or 150Ω loads. In particular, a 100Ω termination provides for VSWR < 2 over the whole band. However, the performance deteriorates in case of a 200Ω termination for which the VSWR exceeds 3. In fact, since the empirical characteristic impedance value for the slotline used here is about 100Ω, the performance is expected to improve as the load values becomes close to 100Ω. In Figure 6.4 we also display data from transmission line (TL) theory, obtained by simply transferring each load impedance to the feed location using the empirical characteristic impedances of the slotline and microstripline sections [39]. Of course, this TL approach neglects junction effects and the corresponding data are presented here as an ideal-case of reference. The agreement between the simulated and TL data is nevertheless reasonable except at the higher-end of the band. This is expected because the junction effects become more influential as the frequency increases.

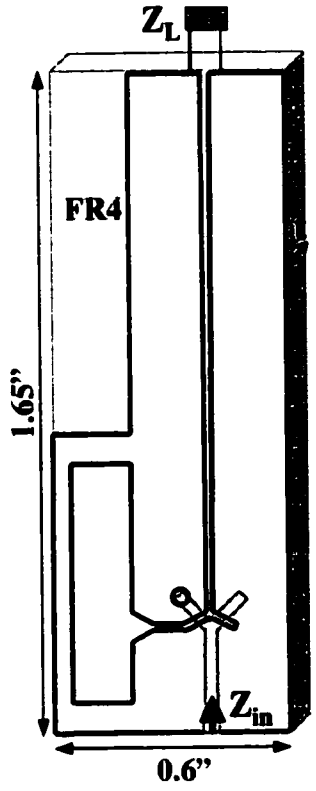

Balun Design Specs:

FR4: t= 0.02", ε_r= 4.15-j0.0595

Microstrip: w_m= 0.030" (Z_{0m}=59Ω)

Slotline (No Taper):

w_s= 0.015" (Z_{0s}=100Ω)

$$\Gamma = \frac{Z_{in} - Z_{ref}}{Z_{in} + Z_{ref}}$$

$$VSWR = \frac{1+|\Gamma|}{1-|\Gamma|}$$

$$Z_{ref} = 50\Omega$$

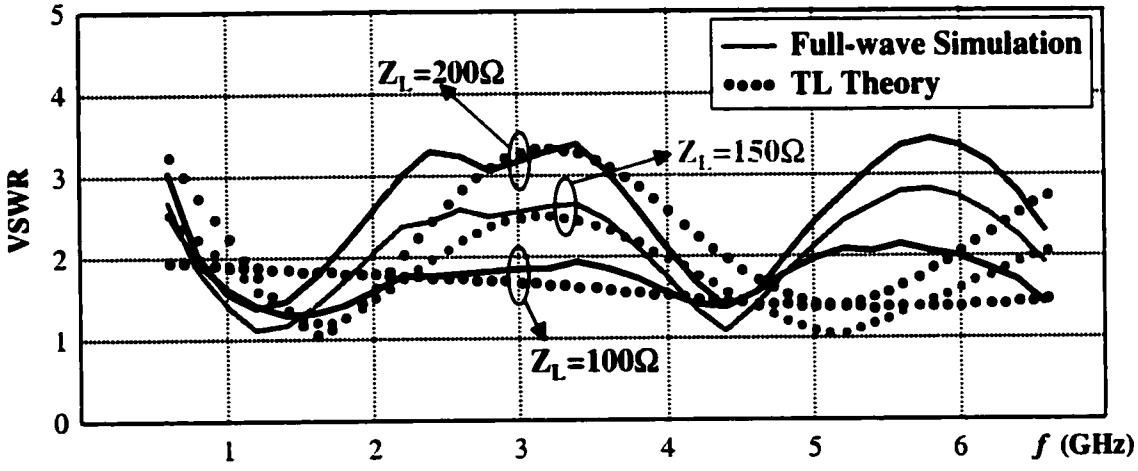

Figure 6.4: Simulated VSWR results for the designed balun/feed structure.

The designed balun/feed structure shown in Figure 6.4 was also fabricated and VSWR measurements were carried out accordingly. As can be seen from Figure 6.5, the simulations agree with measurements reasonably-well over the whole band when the termination is set at 150Ω. Similar agreement was also observed for the 100Ω and 200Ω terminations. Even though a balun structure with a linearly-tapered slotline could not be simulated due to modeling difficulties discussed earlier, a similar structure was analyzed using the TL theory described above. However, the corresponding measurements do not agree with the TL approach. In fact, the TL theory predicts a VSWR of about 1.5 almost over the whole band and the fabricated balun with a linear slotline tapering yields a VSWR < 3 over the band.

In this section, we introduced a new broadband balanced balun/feed design which provides a 6:1 bandwidth for VSWR < 3 when it is terminated with resistive loadings of 100Ω-200Ω. In the next section, we employ this balun design within the slot/FSS configuration to construct the slot/FSS/balun structure shown in Figure 6.1. Corresponding simulations along with measurements are presented for validation purposes.

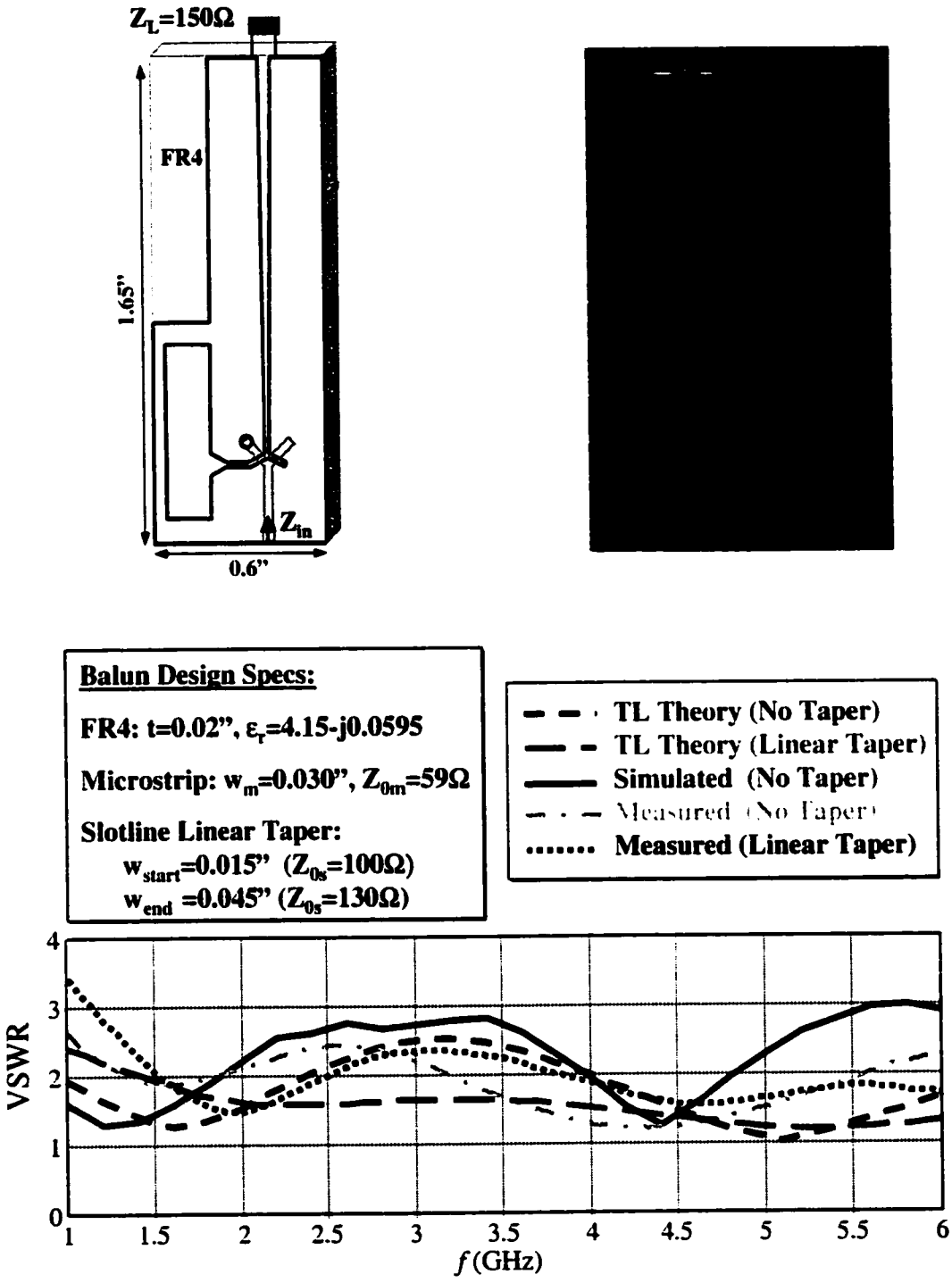

Figure 6.5:Simulated versus measured VSWR characteristics for the designed balun/feed structure.

Slot/FSS/Balun Configuration: Measurements & Validation

Here we incorporate the broadband balun design of the previous section into the broadband slot/FSS design introduced in Chapter 5 (see Figure 5.3). We first describe an alternative way to predict the response of the final slot/FSS/balun configuration and then present the corresponding simulation results along with measurements for validation purposes.

To model the slot/FSS/balun configuration, we considered a two-stage modeling of the whole structure due to its computational complexity. This complexity is caused by the much finer features of the balun/feed structure as compared to the slot/FSS configuration. While modeling the balun structure, we employed about twice the number of prism layers used along the cavity depth (or equivalently along the length of the balun) for the slot/FSS modeling. On top of that the finite-element discretization for the balun modeling was 1/8 of that of the slot/FSS modeling. Hence, the modeling of the whole slot/FSS/balun structure would be computationally too expensive. Instead, here we propose a two-stage modeling approach for analyzing the whole structure. At the first stage of this approach, we computed input impedances for slot/FSS configuration using the infinite array simulator in the same way as done previously. In the second stage, we considered the balun structure and terminated the balun slotline with the slot impedances (varying with frequency) as computed at the first stage. This configuration was used to compute the final impedances. A schematic illustration of this two-stage modeling is given in Figure 6.6. In Figure 6.7, we display the predicted input impedances obtained by means of this proposed approach. Also displayed are the slot impedances for the slot/FSS configuration where the resistivity of the fan element was $50\Omega/cm^2$ (see Figure 5.5).

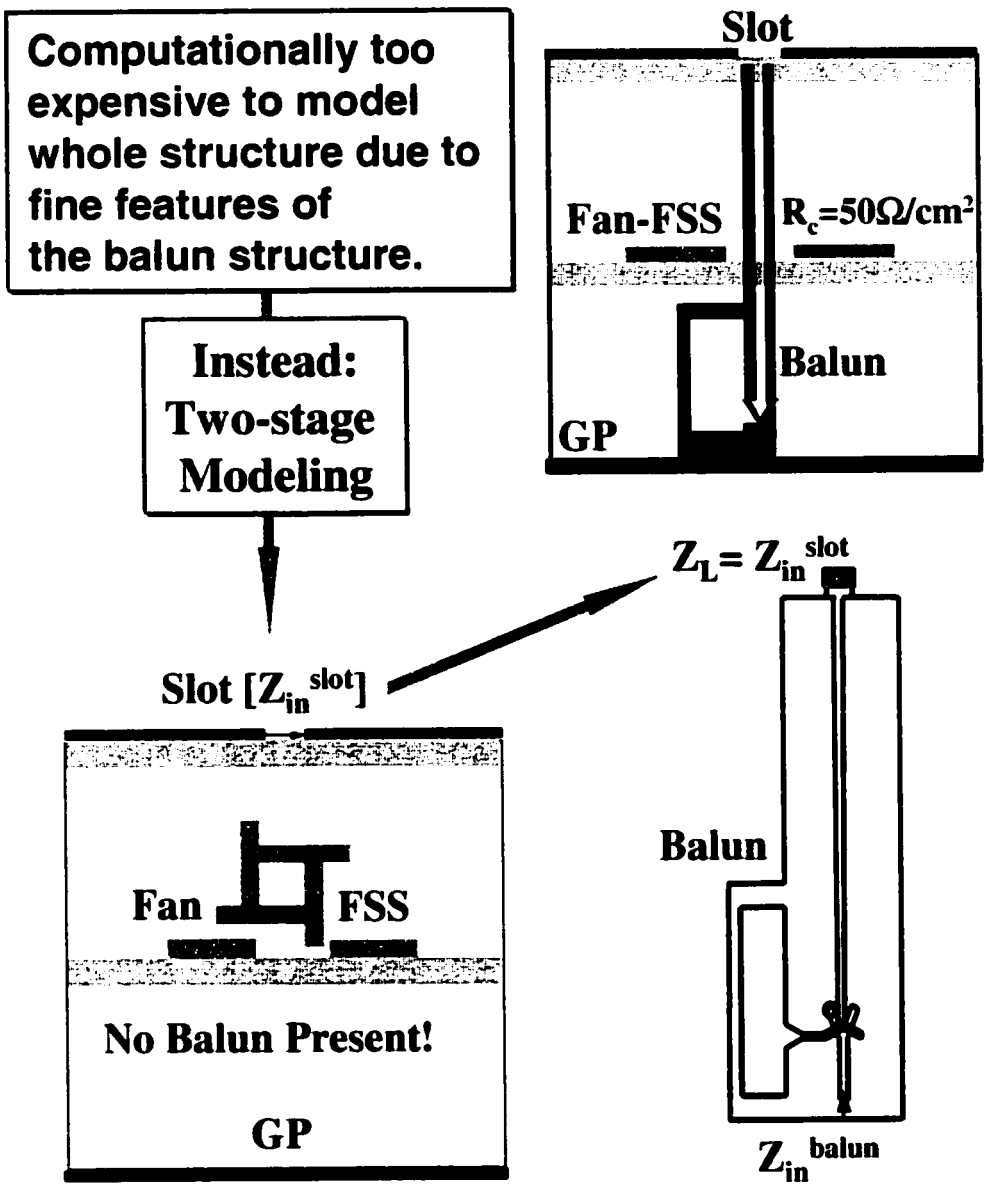

Figure 6.6: Schematic diagram describing the two-stage modeling of the slot/FSS/balun configuration.

As expected, the impedance characteristics shown in Figure 6.7 were changed completely when compared to the slot impedances without the balun feed. In particular, the impedance peak with the balun feed present is quite characteristic and has been repeatedly observed. Of importance is of course that the simulated slot/FSS/balun configuration provides an almost constant impedance profile matched to a 50Ω system over at least a 2:1 bandwidth (starting from 1 GHz up to 2.25 GHz).

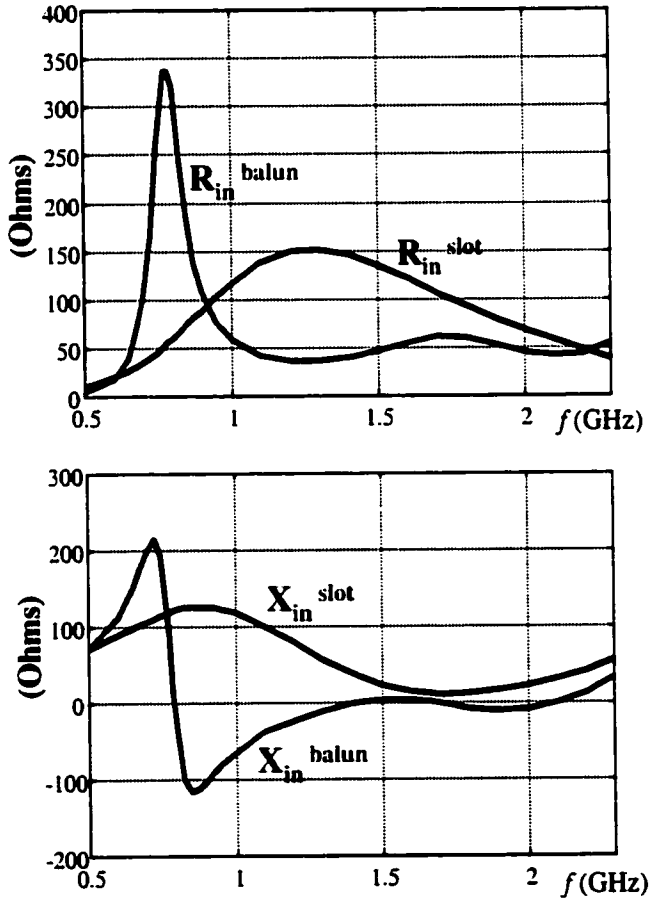

Figure 6.7: Simulated input impedances for the slot/FSS and slot/FSS/balun configurations.

Note that the two-stage modeling presented here is an approximate approach and its accuracy needs to be validated either using another simulator with adaptive meshing capabilities (so that the whole structure can be efficiently modeled) or through measurements. We proceeded to do the latter, with the measured configuration shown in Figure 6.8 (the actual measurement components are explicitly given in Figure 6.9). The corresponding simulated and measured results are compared in Figure 6.10. A small 0.15 GHz frequency shift and reduced impedance levels are observed in the simulated response as compared to the measured response. Nevertheless, the comparison between measurements and calculations is quite good. The differences are likely due to the approximate modeling approach considered for the simulations. Also, in the measurement setup, the configuration was placed in a cavity to simulate the array environment (waveguide simulator), and this can be another reason for the differences. Of importance is that the slot/FSS/balun configuration has the sought after broadband characteristics over at least a 2:1 bandwidth.

In this chapter, we first introduced a broadband balun/feed design to be used as a balanced/matched feed component for the broadband slot/FSS configuration previously presented. We subsequently integrated the two separate designs to construct the slot/FSS/balun antenna structure. The simulations were validated with measurements and demonstrated that the proposed configuration provides at least a 2:1 matched impedance bandwidth.

In the next chapter, we consider other FSS substrates for the reconfigurable slot arrays. A multilayer FSS as well as new slot designs are further introduced for bandwidth enhancement.

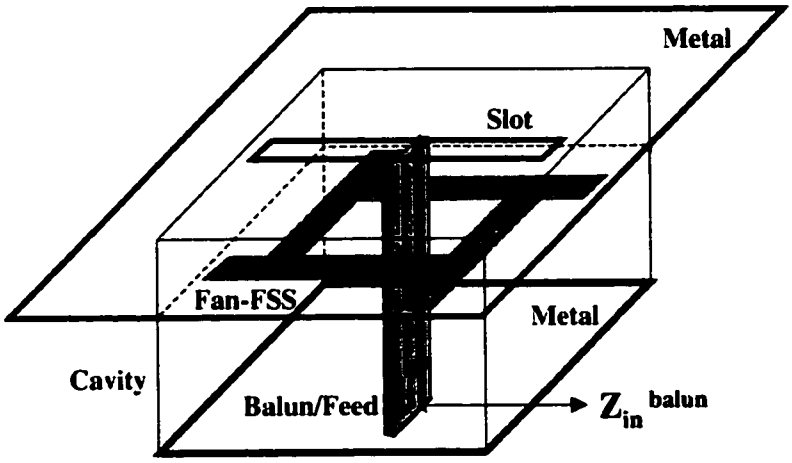

Figure 6.8: Measured slot/FSS/balun configuration.

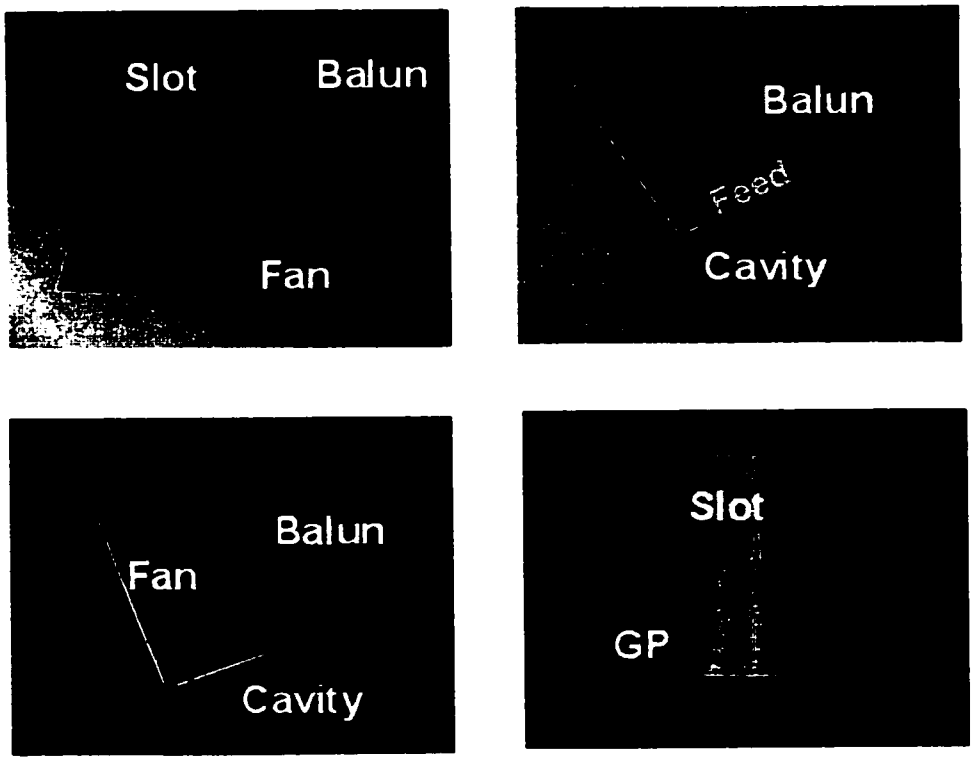

Figure 6. 9: Measurement components of the slot/FSS/balun configuration.

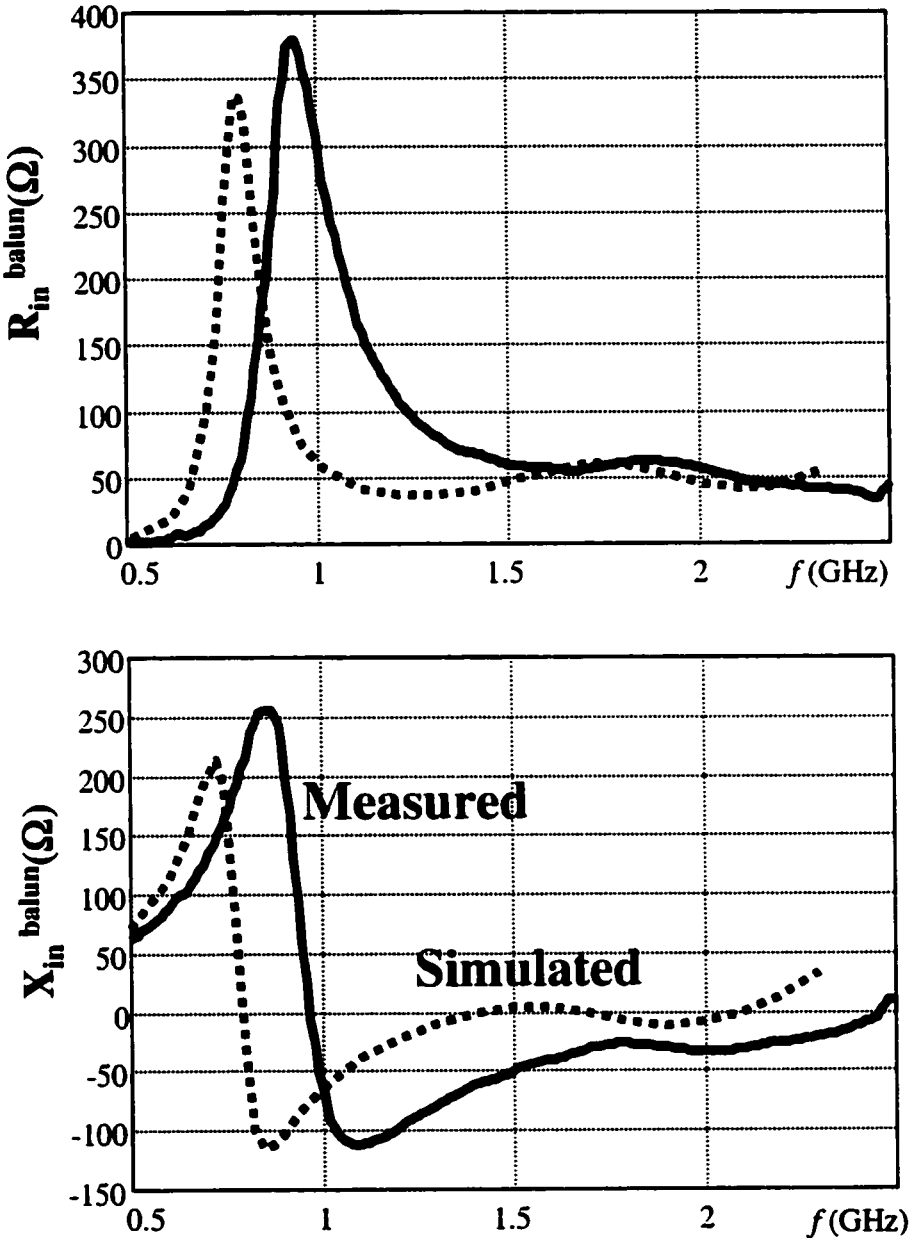

Figure 6.10: Validation of the slot/FSS/balun configuration.

CHAPTER 7

RECONFIGURABLE SLOT ARRAYS ON AN FSS SUBSTRATE

In Chapter 5, we demonstrated bandwidth enhancement for a slot array in presence of an FSS substrate; and then in Chapter 6, we validated the slot/FSS design with measurements by means of a broadband feed element. Here we consider performance of reconfigurable slot arrays in the presence of a similar FSS substrate. Closely-packed crossed slots as shown in Figure 7.1 are used as antenna elements for ease of reconfiguration as well as to avoid grating lobes. An interleaved two-band configuration of these elements provides reduction in array size as much as 40%. Crossed elements also allow for both vertical and horizontal polarizations to be realized.

The array reconfiguration is achieved by means of switches (see Figure 7.1(a)), and in practice, MEMS switches are the preferred choice due to their "on-state" low insertion loss and "off-state" high isolation characteristics over the frequency band of interest. Here these devices are modeled as on/off switches by means of a metallic pad across the width of each slot element. As can be seen from Figure 7.1(a), two types of switches (referred to as #1 and #2) are utilized for reconfiguration to take place. When the switches #2 are opened (off-state), the length of slot dipoles are increased and this is referred to as the low-band array configuration with the parasitic high-band slots (inactive elements) also present (Figure 7.1(b)). In this case, the switches #1 are closed (off-state) to provide isolation between the low-band slots. On the other hand, when the switches #1

are opened (off-state) and the switches #2 are closed (on-state), the slot lengths are shortened and this is referred to as the high-band array configuration (Figure 7.1(c)).

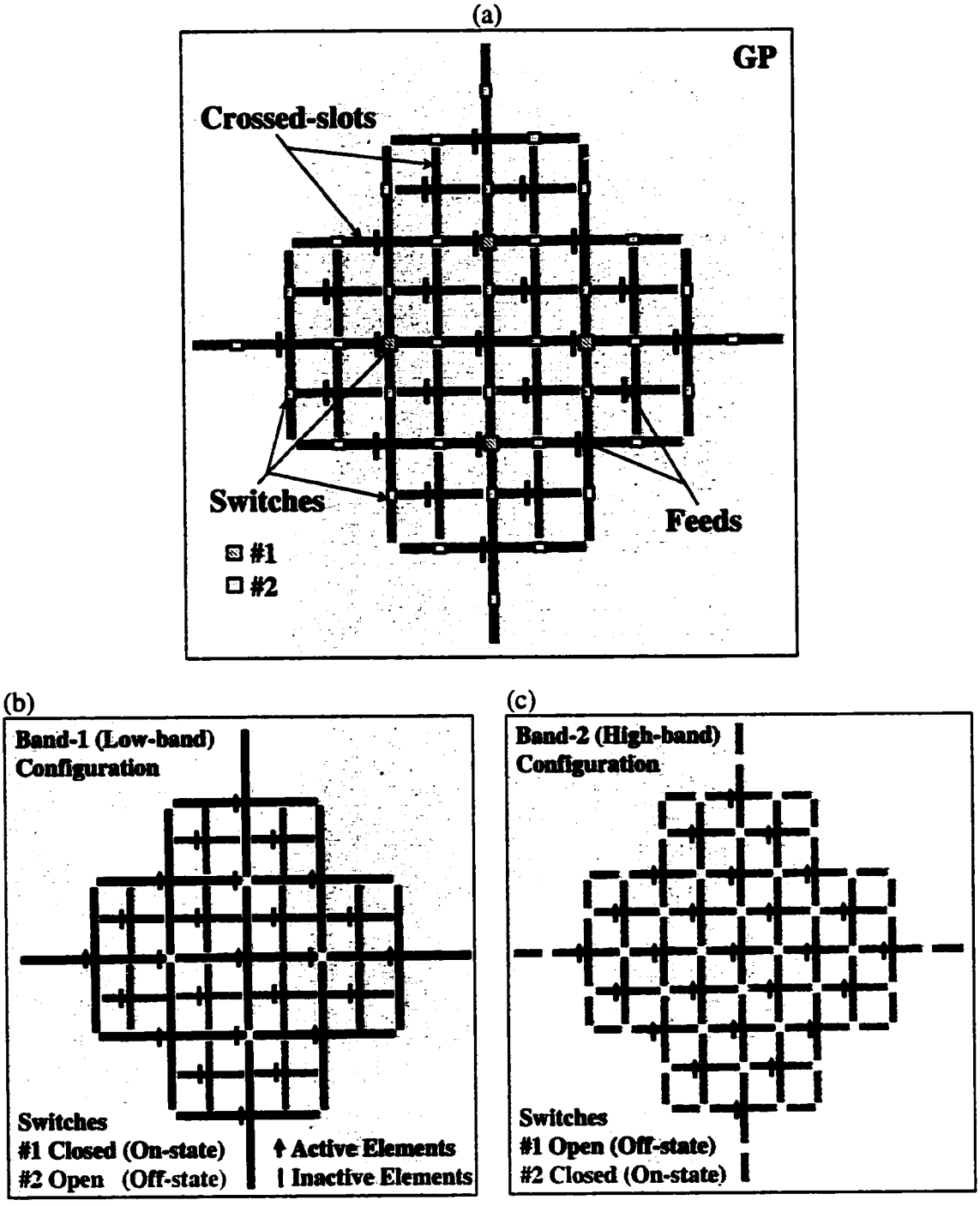

Figure 7.1: Two-band reconfigurable crossed-slot array.

The reconfiguration allows for broadband operation without a need for changing the FSS design which serves as an artificial substrate. That is, the same FSS used for the low-band can also be used when the antenna is reconfigured to operate at a higher band. The frequency band of interest is 0.8-3.2 GHz for a two-band reconfiguration, where 0.8-1.6 GHz band is referred to as Band-1 (low-band), and 1.6-3.2 GHz band is referred to as Band-2 (high-band). In this chapter, we present various reconfigurable slot aperture designs (RESADs) operating over these designated bands. We demonstrate that optimized single layer FSS substrates provide almost the whole band coverage without a need for reconfiguration. Two-band slot designs with multilayer FSS substrates are also introduced to extend the coverage even up to 6.4 GHz. In addition, we examine effects of shorting pins and switches on the bandwidth performance. Finally, we assess gain performance of reconfigurable slot apertures in presence of the FSS substrate. Note that analysis results presented in this chapter were obtained by means of the infinite array simulator, which is discussed in the Appendix and has been well-validated throughout the thesis.

Bandwidth Enhancemet Using Single FSS

We first demonstrate bandwidth enhancement for a reconfigurable crossed-slot array over single layer FSS consisting resistive fan elements as shown in Figure 7.2. The unit cell geometries for Band-1 and Band-2 configurations of this design (referred to as RESAD-1) are also given in Figure 7.2. Note that among the parameters specified in Figure 7.2, the FSS parameters (fan size and resistivity) and the slot-to-FSS distance are the most critical ones which control bandwidth improvement. In Figure 7.3, we display input impedance characteristics for RESAD-1 with and without presence of the designed

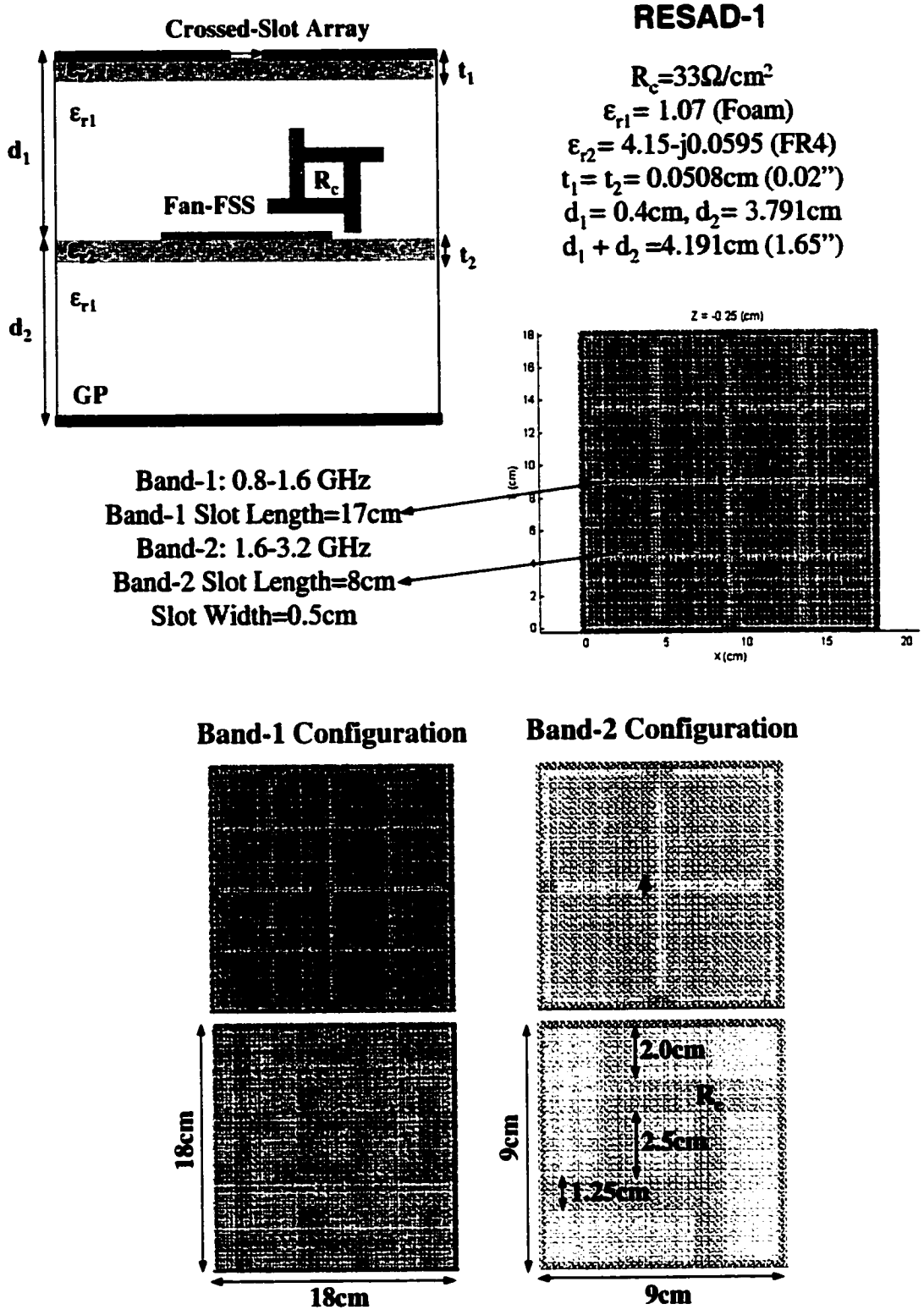

Figure 7.2: Reconfigurable slot aperture design; RESAD-1.

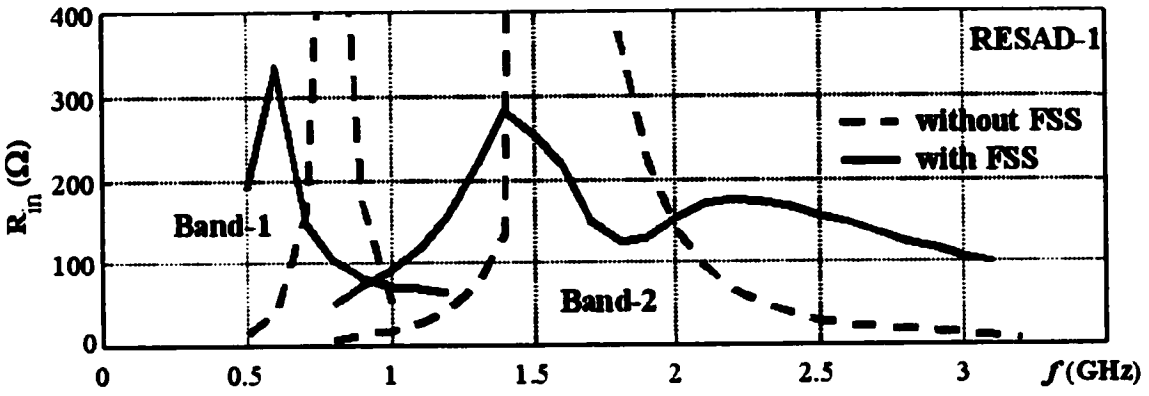

Figure 7.3: Input impedance characteristics (real part) for RESAD-1 with and without presence of the FSS substrate.

FSS substrate. As seen, the FSS substrate provides bandwidth enhancement for the reconfigurable crossed-slot array. In particular, Band-2 configuration covers nearly the whole band (1.05-3.1 GHz) where the impedance levels (real part) vary between 100-300 Ohms. On the other hand, the response for Band-1 configuration shifts towards lower frequencies, thus forming a gap between two responses. This frequency shift in the response is mainly due to presence of parasitic high-band (Band-2) slots during low-band (Band-1) operation. In fact, Band-2 slots increase the effective length of the Band-1 slots during low-band operation (see Figure 7.2), and this loading effect lowers the resonance.

We further optimized RESAD-1 to improve the bandwidth performance of Band-2 configuration. Resulting designs referred to as RESAD-2 and RESAD-3 are depicted in Figure 7.4 along with their corresponding responses shown in Figure 7.5. As seen from Figure 7.5, the impedance variation over the band was improved by means of these new designs. Also, the band-coverage was extended about 0.2-0.3 GHz. These improvements

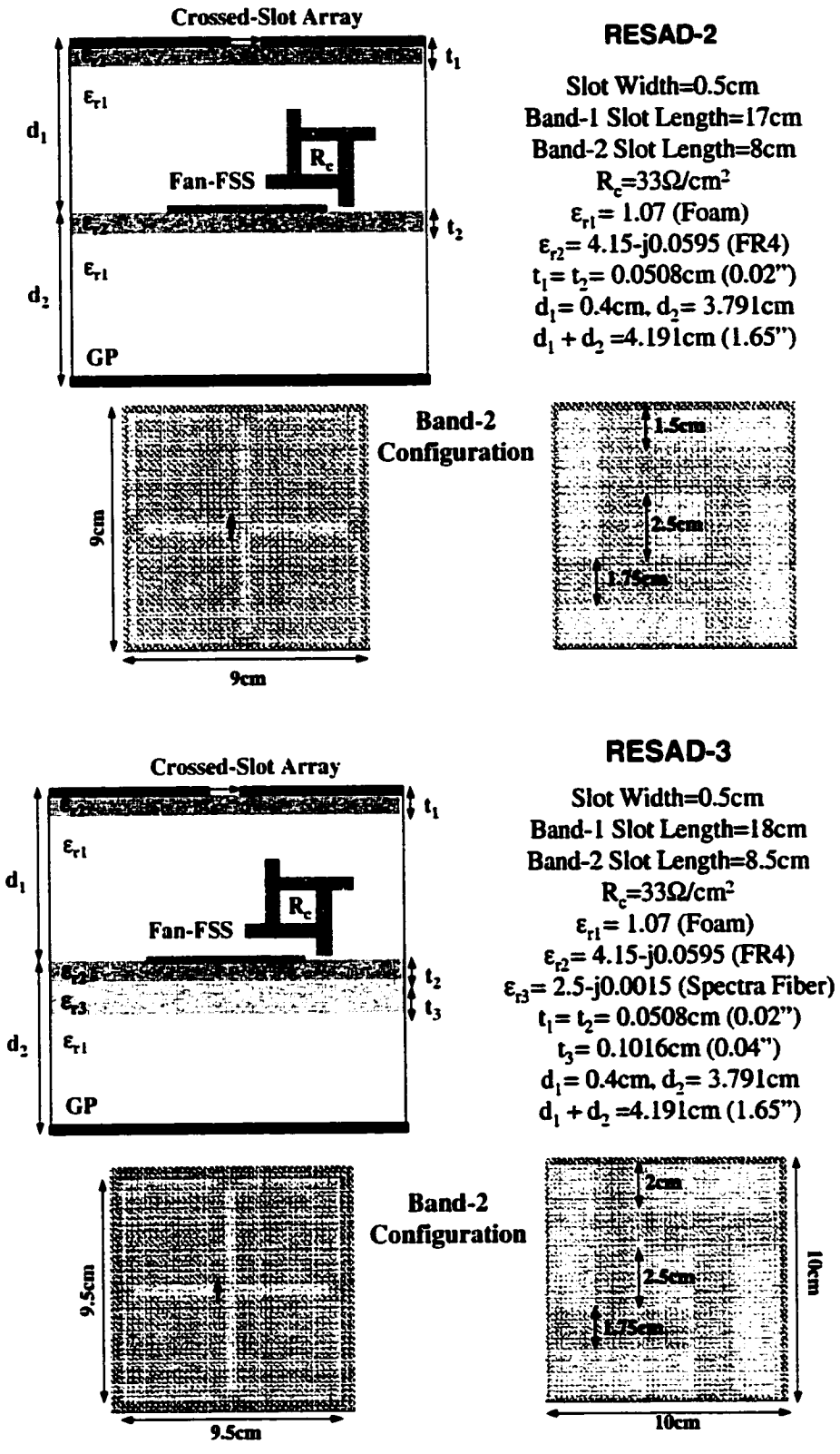

Figure 7.4: Reconfigurable slot aperture designs; RESAD-2 and RESAD-3.

were obtained by modifying the fan element, and further by changing slot dimensions and placing an additional substrate below the FSS layer. As shown in Figure 7.5, almost a 3:1 bandwidth was achieved for the crossed slots by means of the optimized FSS substrates where the real part of the impedances remained around 150 Ohms over the band. Next we consider a multilayer FSS substrate under the reconfigurable slot array to extend the band-coverage beyond 3.2 GHz.

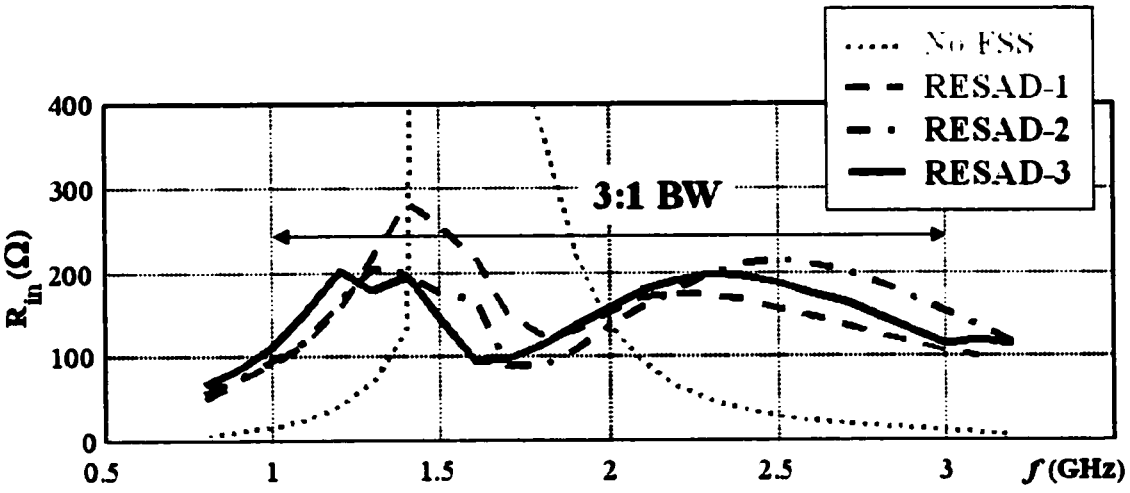

Figure 7.5: Input impedance characteristics (real part) for RESAD-1, RESAD-2, RESAD-3, and the no-FSS case; Band-2 response is shown.

Bandwidth Enhancement with Multiple FSS

To achieve operation over 3.2 GHz with reconfiguration, we considered an additional FSS layer in the design as shown in Figure 7.6. We display the corresponding Band-1 response of this dual FSS design (referred to as RESAD-4) in Figure 7.7 for different cases. As seen, although the impedance bandwidth was improved with the fan-

FSS (referred to as FSS-2), the inclusion of Band-1 parasitic slots degraded this improvement. Furthermore, including a secondary FSS layer (referred to as FSS-1) just under the slots shifted the response towards the lower frequencies. As a result, Band-1 configuration with double layer FSS in presence of parasitic Band-2 slots delivered a 2:1 impedance bandwidth over 0.8-1.6 GHz where the real part of the impedance varied between 100-400 Ohms. Note that Band-1 configuration of RESAD-4 is a commensurate structure where unit cell periodicities within the structure are the same.

On the other hand, the corresponding Band-2 configuration depicted in Figure 7.8 is a non-commensurate structure where the unit cell periodicities for the slot aperture and FSS-1 are the same and different from that of FSS-2. Impedance characteristics for this configuration are also displayed in Figure 7.8. As seen, the bandwidth was greatly improved by dual FSS in this case as the real part of the impedance remained between 250-400 Ohms over the frequency band of 2.7-6.7 GHz. In particular, the response remarkably leveled at 270 Ohms over the 3.7-5.7 GHz band.

In Figure 7.9, we display both Band-1 and Band-2 responses for RESAD-4. As seen, the 0.8-6.4 GHz band is nearly covered by means of dual FSS and reconfiguration. Nevertheless, the performance is degraded within the frequency band of 1.6-2.5 GHz where the impedances are on the order of 100 Ohms or less, thus forming a gap between Band-1 and Band-2 responses (see Figure 7.9). Next we introduce a novel slot design along with dual FSS to close this gap, and achieve a rather continuous/broad bandwidth coverage.

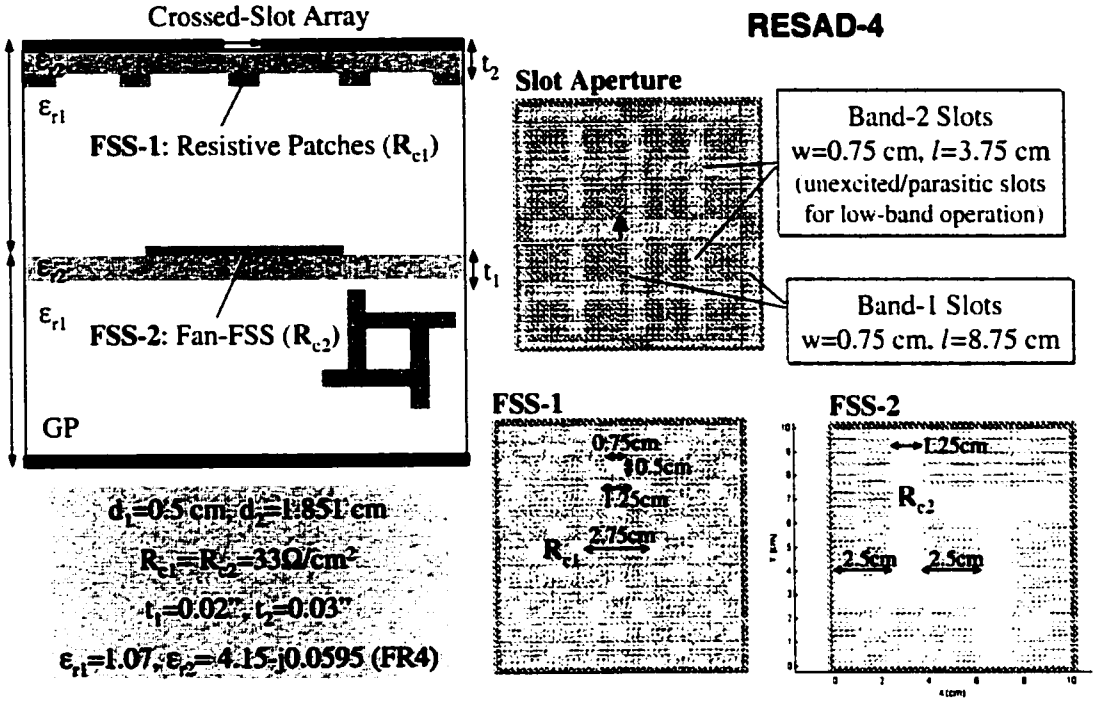

Figure 7.6: Reconfigurable slot aperture design; RESAD-4.

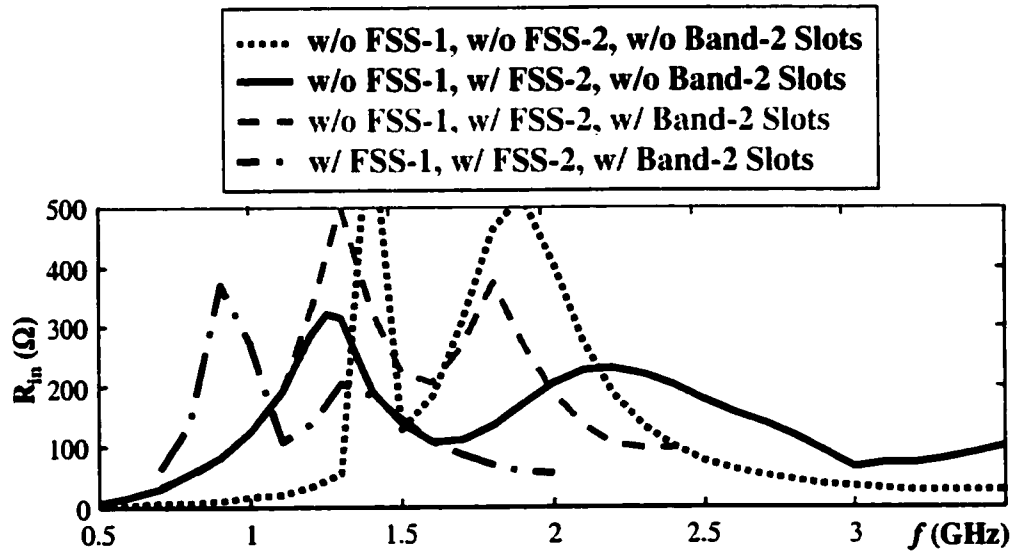

Figure 7.7: Input impedance characteristics (real part) for RESAD-4 with/without presence of FSS-1, FSS-2, and Band-2 slots; Band-1 response is shown.

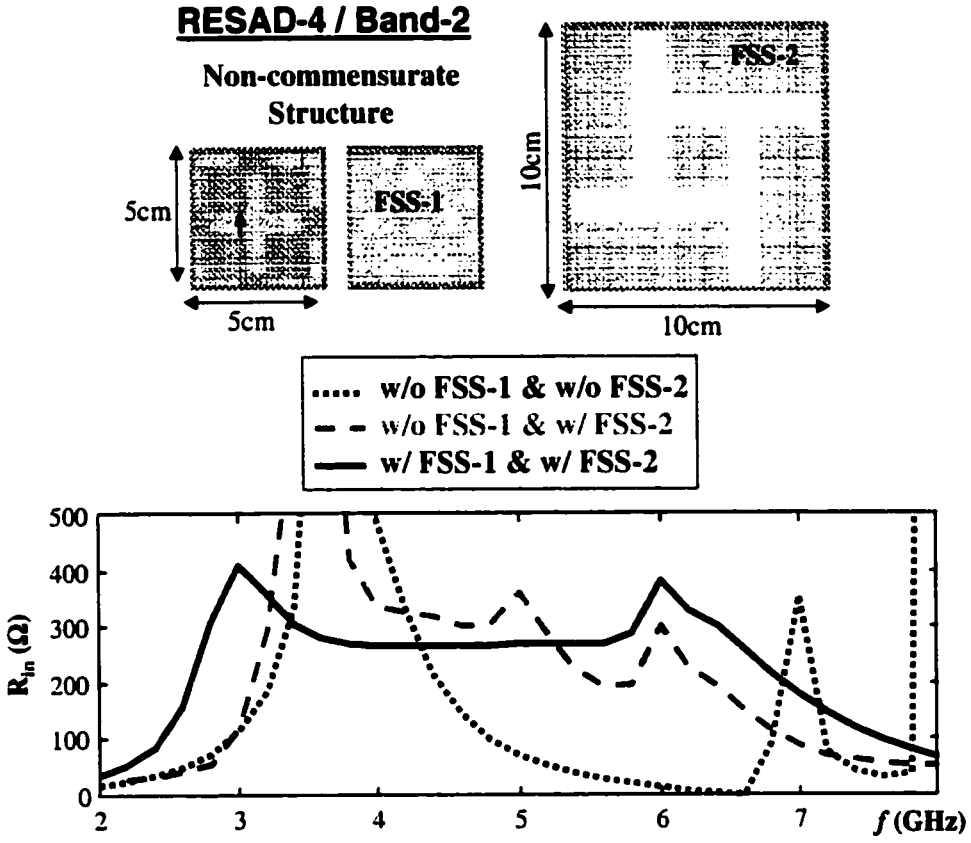

Figure 7.8: Input impedance characteristics (real part) for RESAD-4 with/without presence of FSS-1, FSS-2; Band-2 response is shown.

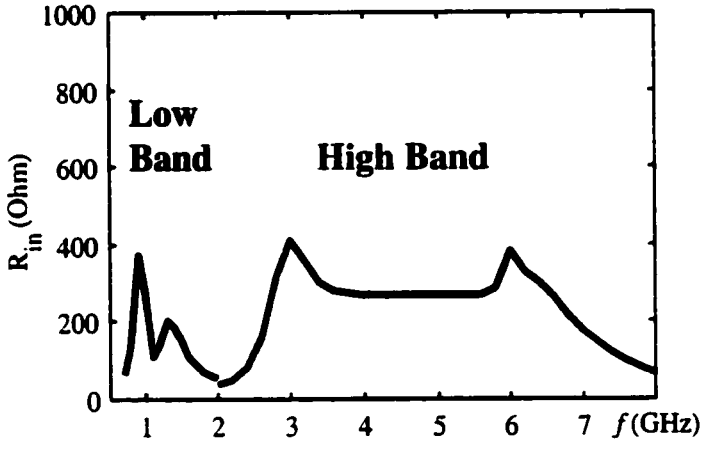

Figure 7.9: Input impedance characteristics (real part) for RESAD-4; both Band-1 and Band-2 responses are shown.

Novel Slot Element Designs

To achieve continuous bandwidth coverage by means of a two-band reconfiguration, we considered inductive loadings within the slot elements as shown in Figure 7.10 in addition to employing a dual-FSS substrate. These loadings were obtained by increasing the slot-width across the slot length at several locations. These spots were chosen accordingly so that they would not overlap with the switch locations, thus allowing proper reconfiguration to take place. A secondary FSS layer consisting of resistive patches was placed just under the slots as depicted in Figure 7.10. As seen, these patches are located just under the slot loadings and they have the same shape as of slot loadings. In Figure 7.11, we display the corresponding input impedance characteristics of this novel slot aperture design (referred to as RESAD-5). As seen, inductive loadings introduced within the slots along with the dual-FSS substrate provided an outstanding 10:1 impedance bandwidth coverage (0.7-7 GHz) with reconfiguration. The average impedance value over this band was 166 + j78 Ohms. The corresponding return loss characteristics are displayed in Figure 7.12, which also demonstrates extremely broadband performance.

Furthermore, we placed an additional FR4 substrate (ε_r=4.15-j0.0595, t=0.1992cm) below the resistive patches to further improve the bandwidth performance. As seen in Figure 7.13, this new design referred to as RESAD-6 provided improved bandwidth performance with less variation in the impedance values over the whole band as compared to RESAD-5.

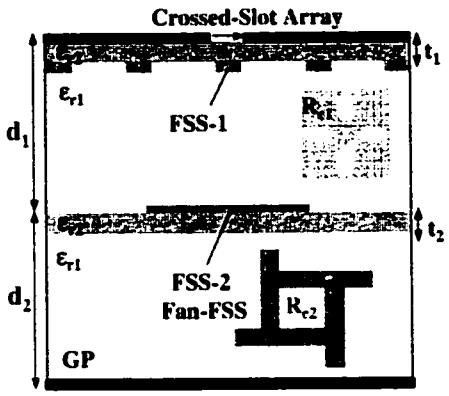

RESAD-5

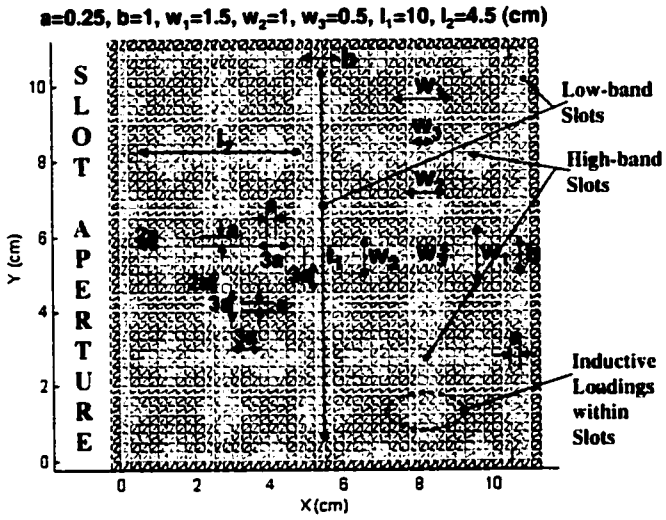

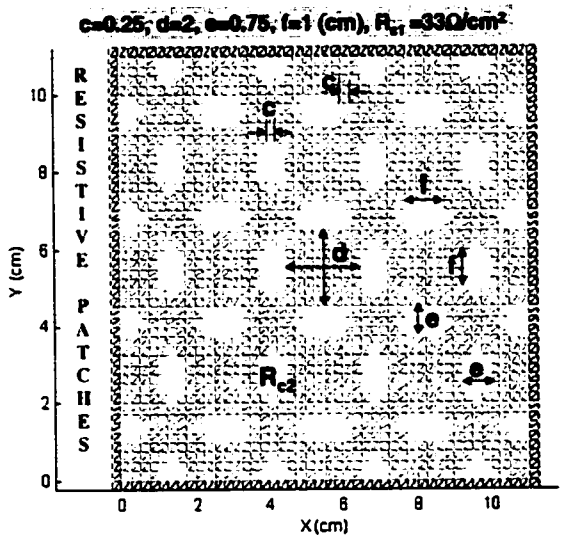

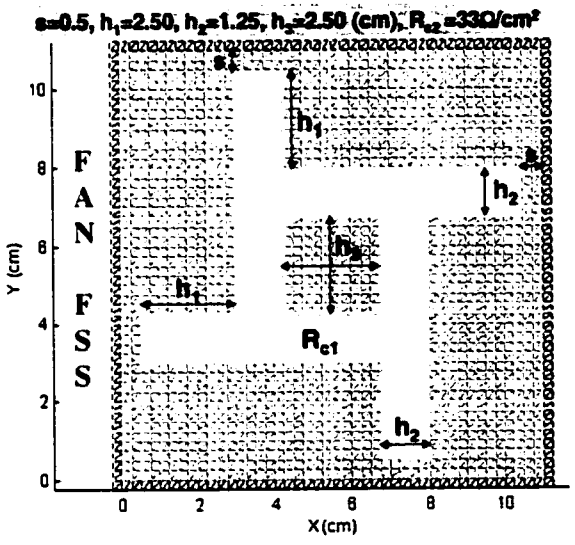

Figure 7.10: Reconfigurable slot aperture design; RESAD-5.

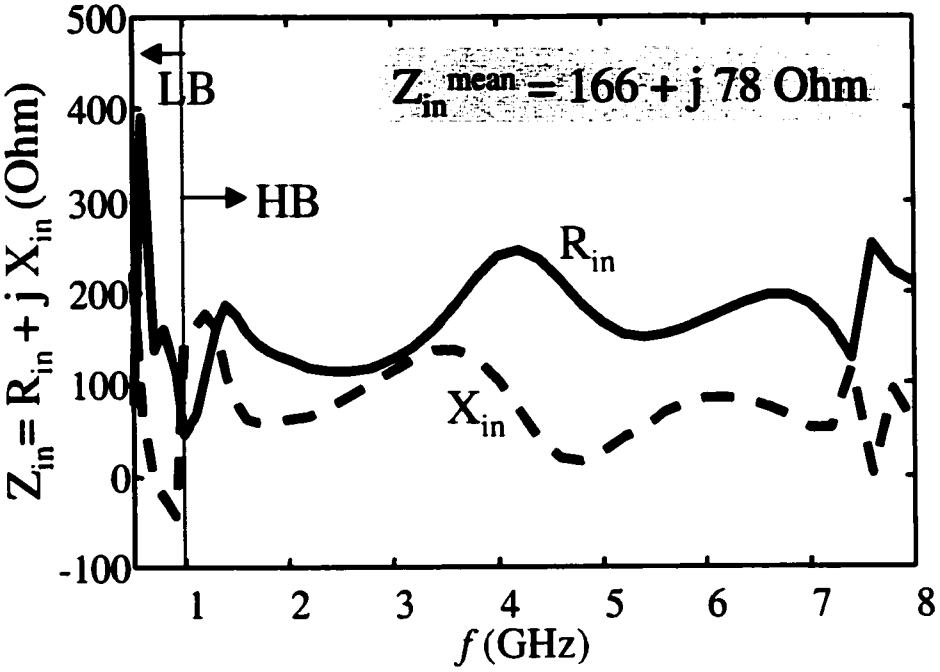

Figure 7.11: Input impedance characteristics for RESAD-5.

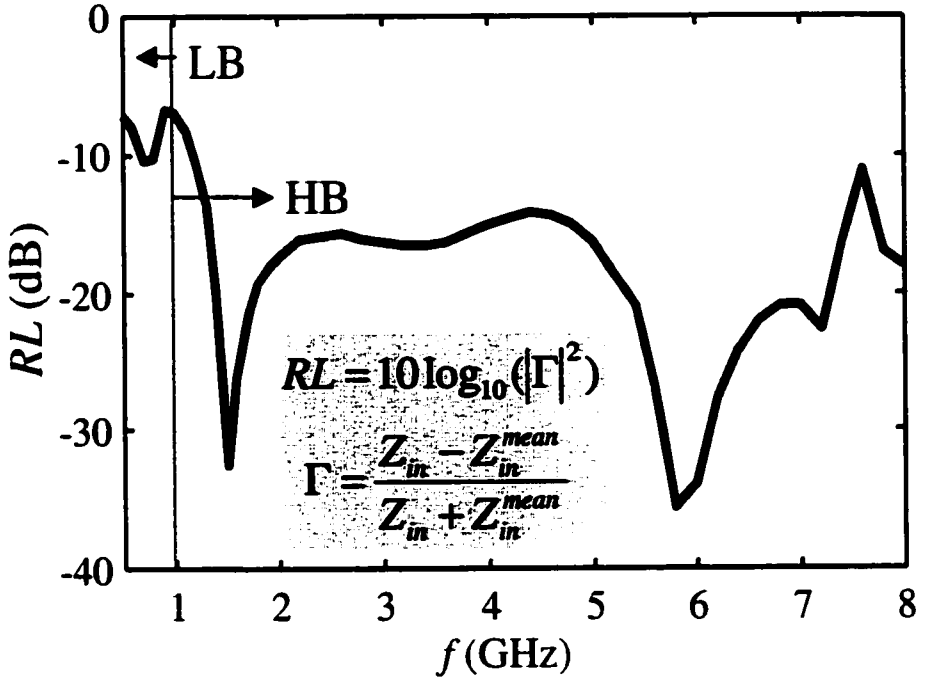

Figure 7.12: Return loss characteristics for RESAD-5.

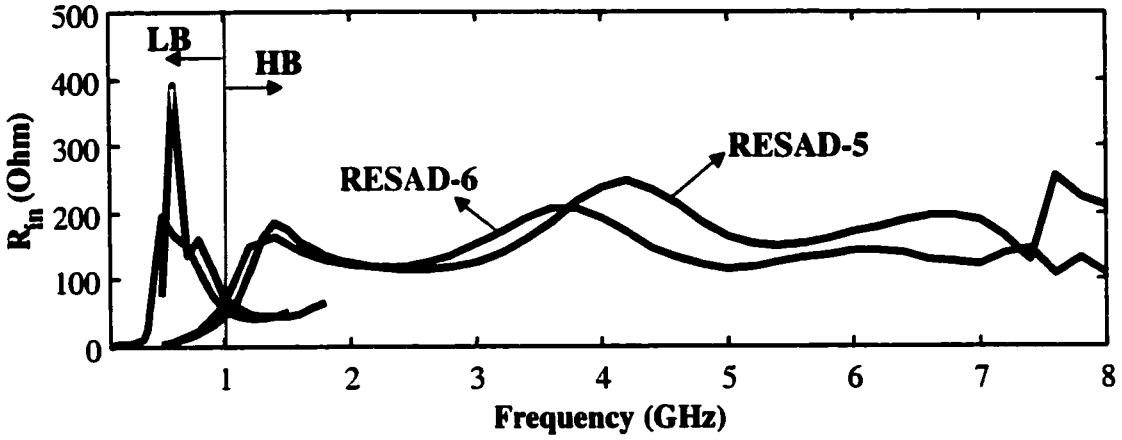

Figure 7.13: Input impedances (real part) for RESAD-5 and RESAD-6.

Note that the low-band and high-band configurations of RESAD-5 were analyzed as commensurate and non-commensurate structures, respectively. To provide an additional validation for the array simulator, we also analyzed a commensurate version of the high-band configuration of RESAD-5 by constructing a super cell for the slot aperture as illustrated in Figure 7.14. For the non-commensurate case, the slot aperture along with the resistive-patch layer (FSS-1) had a unit cell of 5.5x5.5 cm^2, and the fan-FSS unit cell was 11x11 cm^2. In this case, there was only one slot element present in the unit cell (see Figure 7.14). On the other hand, for the equivalent commensurate configuration, the unit cell periodicities remained the same within the structure (11x11 cm^2) and there were five more slot elements present in the super cell. Comparison of the computed slot impedances for the commensurate and non-commensurate configurations is displayed in Figure 7.15. As seen, the input impedances agree reasonably well with each other over the whole band, thus validating the accuracy of the simulator for non-commensurate configurations.

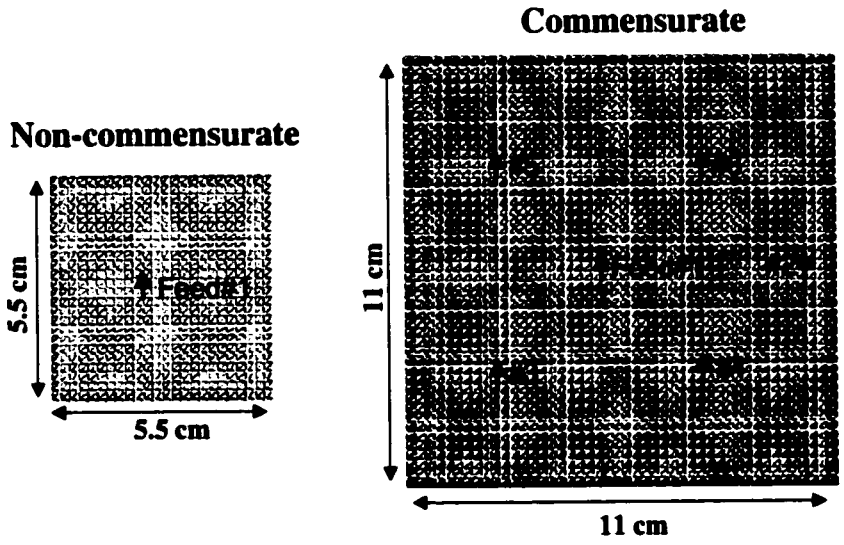

Figure 7.14: Slot aperture unit cell geometries of non-commensurate and commensurate high-band configurations for RESAD-5.

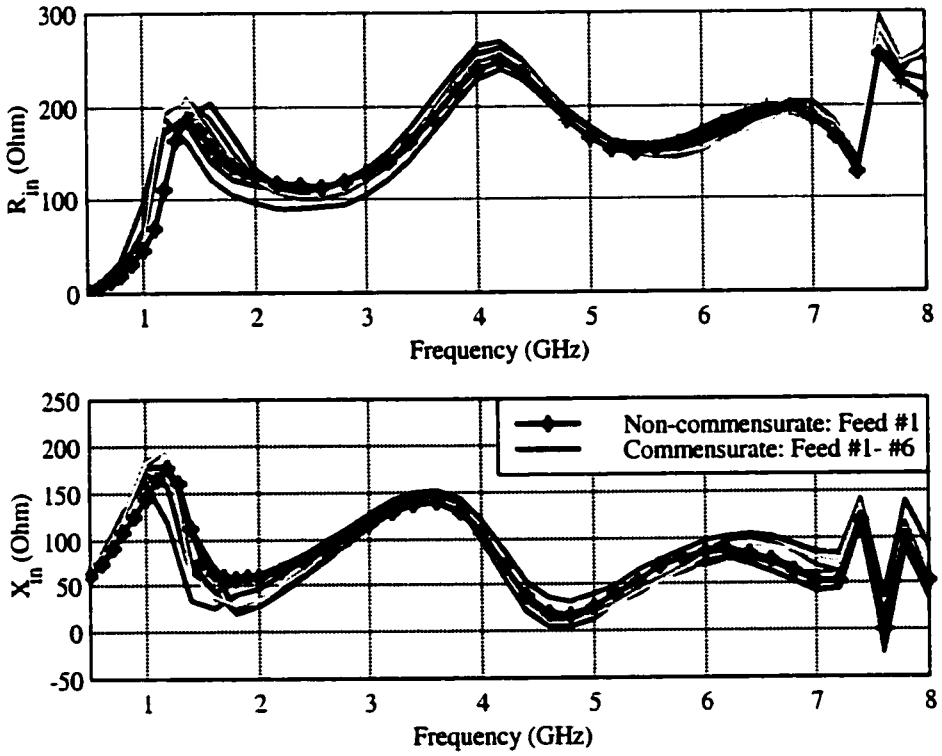

Figure 7.15: Input impedances for non-commensurate and commensurate high-band configurations for RESAD-5.

Effects of Switches & Shorting Pins on Bandwidth Performance

In practice, array reconfiguration is achieved by MEMS switches as mentioned before and these devices are modeled as on/off switches by means of a metallic pad across the width of each slot element. When the switches are closed (on-state), a very low resistance on the order of 0.1 Ω is introduced across the slot-width, resulting in a very low insertion loss. In this case, effect of switch presence on the slot impedance is expected to be unnoticeable. On the other hand, when the switches are opened (off-state), they behave like a capacitor with a very low capacitance (~4 fF), thus yielding a high isolation characteristics. In this case, however, due to frequency dependence of the elements, it is of importance to evaluate the effect of switches on the slot impedances and the bandwidth performance. For this purpose, we analyzed the low-band configuration of RESAD-4 in presence of an equivalent off-state switch model as depicted in Figure 7.16. As seen, the switches were modeled by metallic switch pads and equivalent off-state capacitors across the pads. In Figure 7.17, we display input impedance characteristics for RESAD-4 with and without presence of equivalent switch model. As can be seen, a slight frequency shift is observed with the inclusion of the switch model. In practice, we expect to observe much less frequency shift since practical switches are much smaller in size than the ones modeled here. Note that it would be computationally too expensive to model the switches in their realistic size.

Other components of interest are shorting pins which are placed along the depth of cavity with the intention of suppressing possible parasitic modes which may occur within the structure. To evaluate effect of shorting pins on the slot impedances, we analyzed slot aperture configurations shown in Figure 7.18. Note that the pins were placed accordingly so that they would not cut through the FSS elements. As seen, we also considered configurations where rotated fan elements were used. In Figure 7.19, we display slot impedances with and without presence of shorting pins for the rotated and

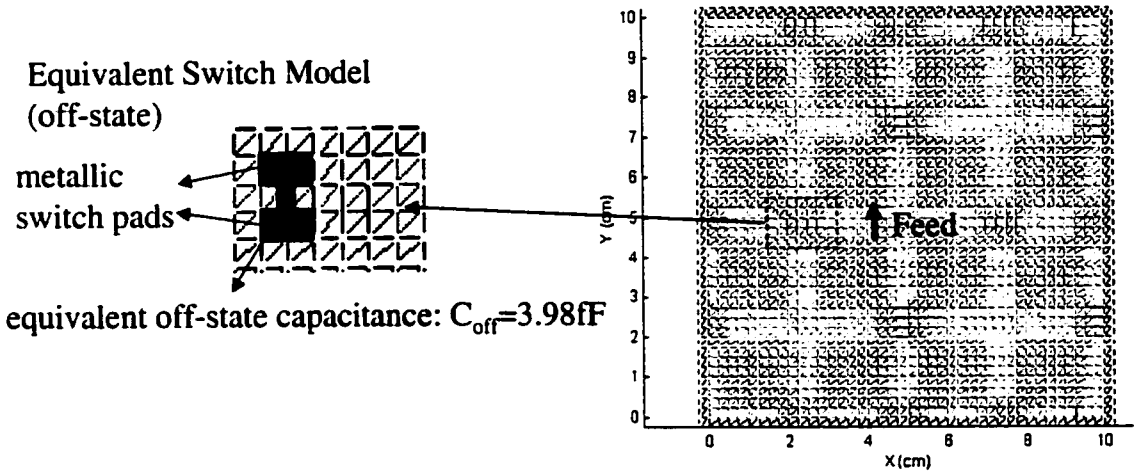

Figure 7.16: Band-1 (low-band) configuration for RESAD-4 in presence of off-state equivalent switch model.

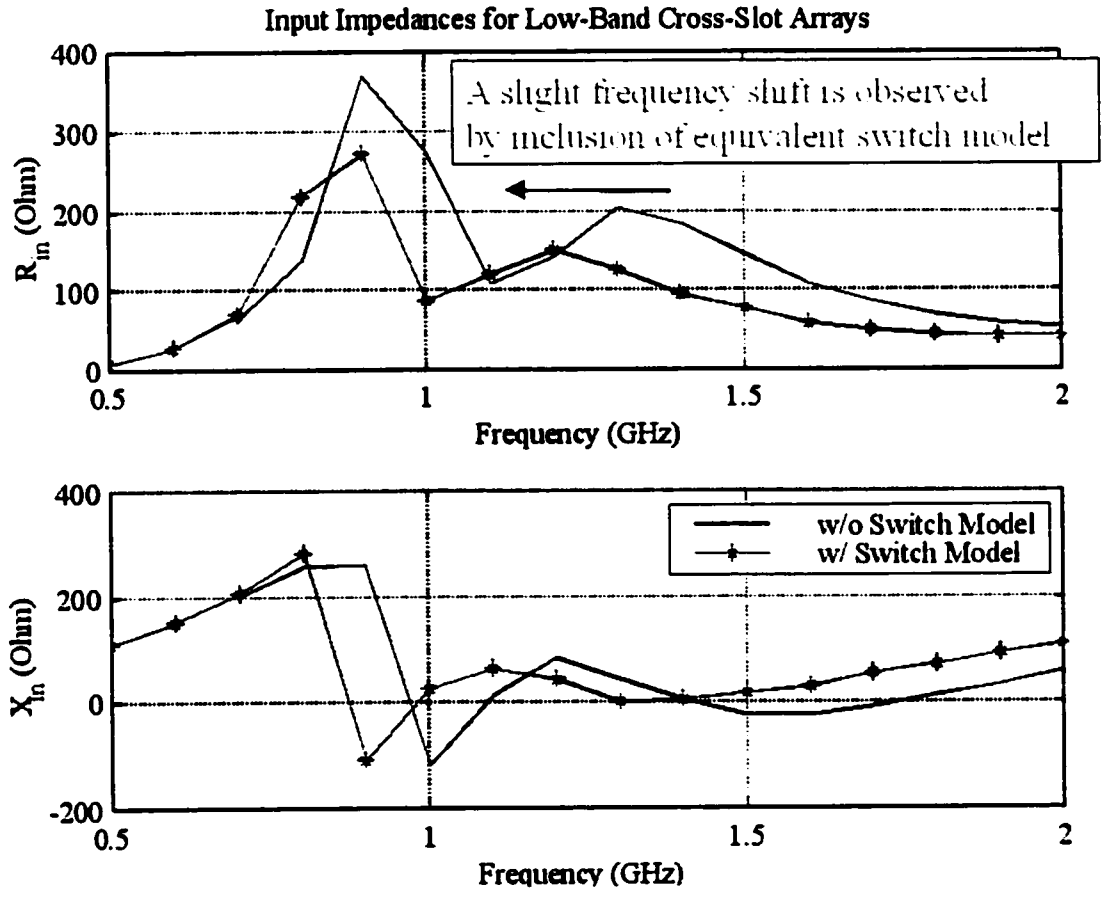

Figure 7.17: Effect of switches on the bandwidth performance.

orthogonal element orientations. As seen, no major effect is observed due to inclusion of shorting pins in either case. On the other hand, rotated fans sharpen the first resonance peak and provide narrower impedance bandwidth.

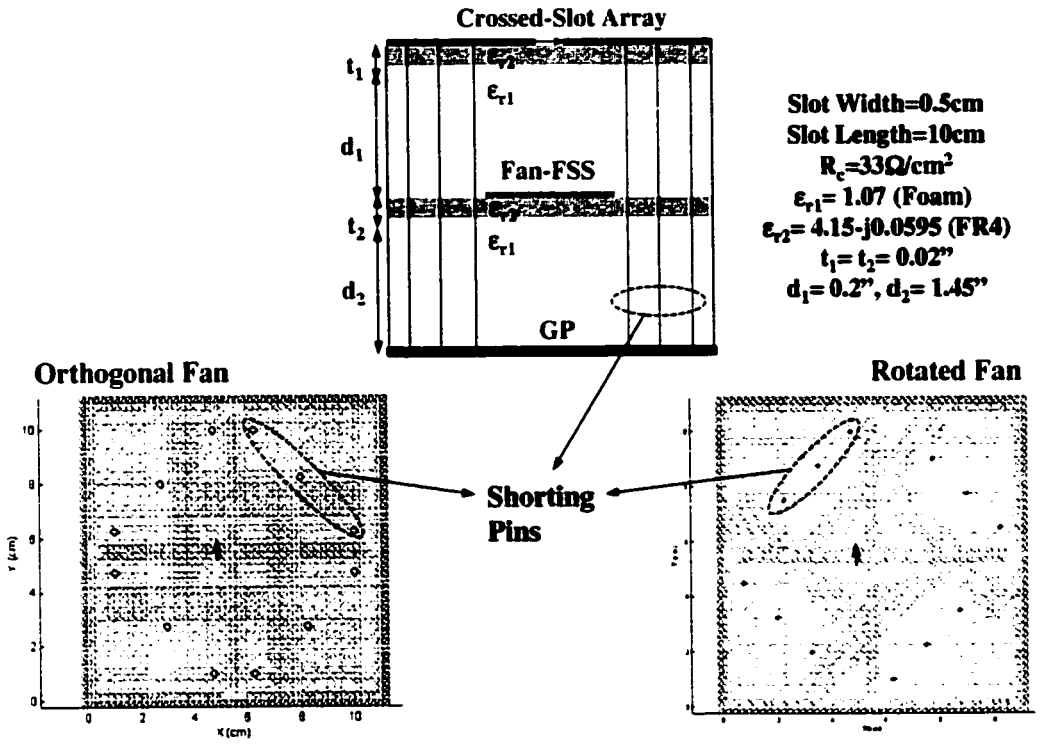

Figure 7.18: RESAD in presence of shorting pins.

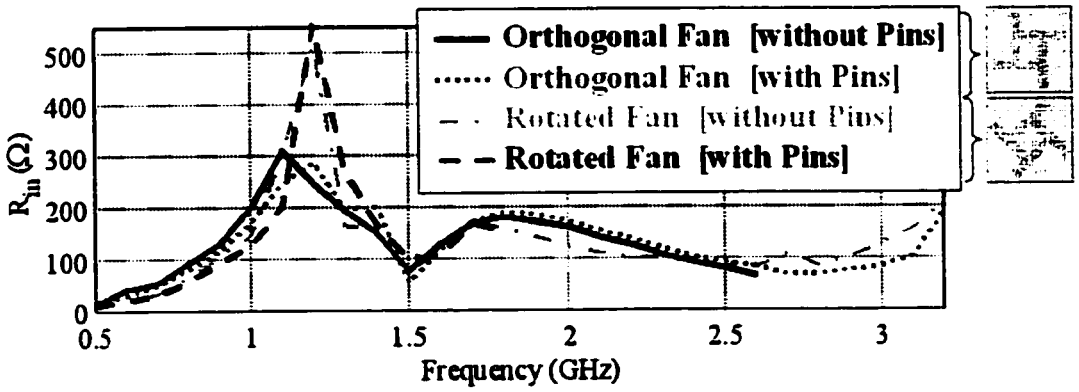

Figure 7.19: Effect of shorting pins and fan orientation on the bandwidth performance.

Gain Performance

Finally, we assess gain performance of reconfigurable slot arrays over the FSS substrate. As discussed in Chapter 5, there is a compromise between overall gain and bandwidth performance of slot arrays with the lossy FSS substrate, and it was demonstrated that the gain profile could be improved at the expense of slot bandwidth. Two important control parameters in this respect are the slot-to-FSS distance (d_1) and the FSS loading (resistivity, R_c). When both of these parameters are increased, the gain profile is improved by sacrificing from the bandwidth. To demonstrate a similar effect for the crossed-slot arrays, we considered Band-2 configuration for RESAD-3, which provided optimum bandwidth for the crossed elements (see Figure 7.5). Corresponding gain profiles along with return loss and mismatch efficiencies for different d_1 and R_c values are displayed in Figure 7.20. Note that the reference impedance value used for the computation of return loss was 150 Ohms. As seen, the isolated slots (no-FSS case) provide higher gains as compared to the slots over the FSS substrate over the whole band, as expected. However, at 1.5 GHz, there exists a dip in the gain profile for the former. In fact, this sudden fall in the gain occurs when the corresponding return loss becomes 0 dB and the mismatch efficiency reaches its lowest value over the band. By use of the FSS substrate, however, this dip is smoothed out and for the optimum bandwidth case it is improved by 10 dB. As d_1 and R_c increase, we observe improvement in the gain profile at the expense of bandwidth. In particular, when d_1=0.30" and R_c=150Ω/cm^2, the corresponding profile results in gain reduction of as much as 3 dB over the 1.6-3.2 GHz band as compared to the no-FSS case. A similar gain/bandwidth behavior was also

observed for the Band-1 configuration when the array was reconfigured to operate at lower frequencies.

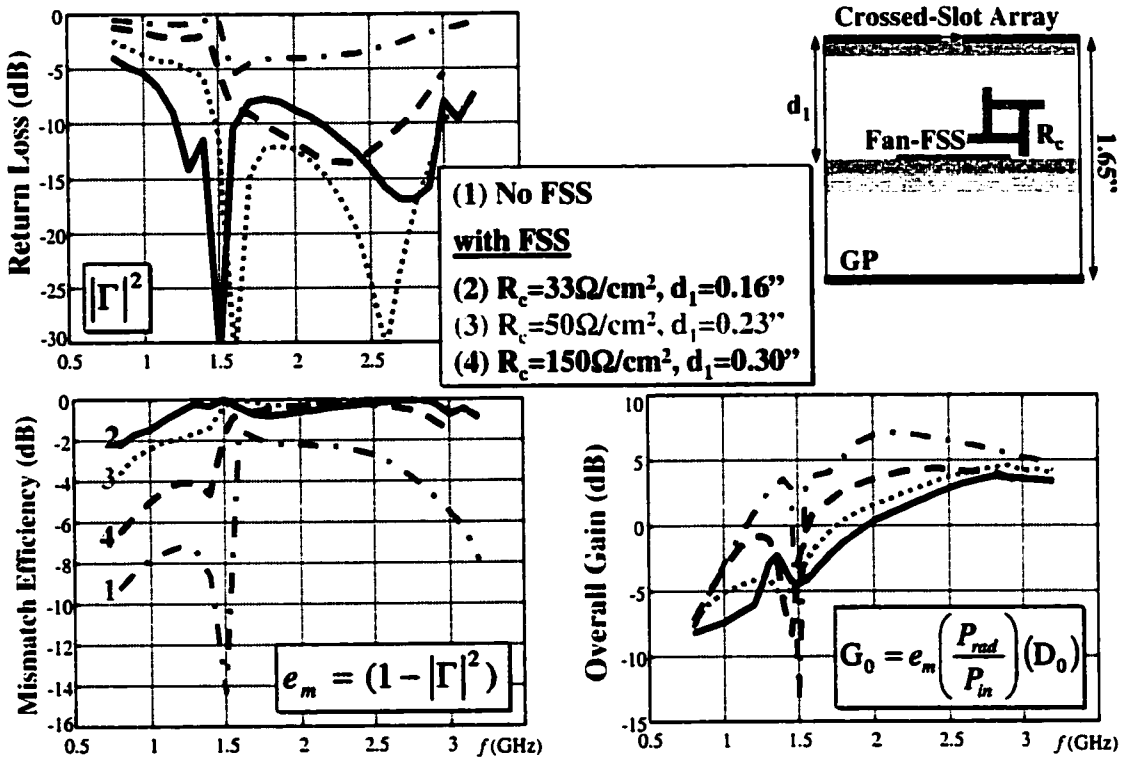

Figure 7.20: Gain performance of crossed-slot array in presence of the FSS substrate.

CHAPTER 8

SUMMARY & CONCLUSIONS

Conformal antenna bandwidth is determined by the antenna element itself and the cavity/substrate structure. Regardless of how the element bandwidth is enhanced, the major limitation for today's conformal arrays relates to the substrate. Much effort in recent years has been devoted to designing substrates that alleviate this bandwidth limitation, and this thesis has offered some new bandwidth enhancement techniques for conformal arrays.

Conformal arrays are usually printed on a planar or curved substrate which consists of a dielectric material backed by a metallic surface. This metal backing is used as a reflecting ground plane (GP) that partially shields objects on the other side. The presence of a GP plays a crucial role in array performance since it re-directs one-half of the radiation into the upper half-space, thus enhancing antenna gain by 6 dB. However, this optimum performance is obtained only when the antenna-to-GP distance is a quarter wavelength at the operating frequency, thus leading to narrowband operation. For broadband operation the effective electrical spacing should remain constant as the operating frequency changes. However, since the physical spacing between the array surface and GP is fixed, such an electrical height change can be achieved only by adjusting the effective dielectric constant of the substrate material and this can be accomplished by possibly using a frequency-dependent substrate. Such a frequency-

dependent substrate should provide in-phase reflections over a broad band of frequencies to improve the overall array performance.

In this thesis, we proposed a new class of broadband substrates aimed at enhancing the bandwidth of conformal arrays. The proposed broadband substrates consisted of multilayer frequency selective surfaces (FSS's) that artificially alter the GP location. These multilayer FSS's are therefore artificial substrates whose reflection coefficient response varies with frequency to enhance array performance. In fact, the FSS used in the array acts to adjust the electrical distance between the FSS and the antenna so that the FSS substrate mimics a magnetic GP over a broad bandwidth (i.e., the reflection coefficient has a nearly constant phase around zero degrees). Below we summarize the thesis work whose focus was on the development of such artificial FSS substrates and on demonstrating their broadband performance with conformal arrays.

In designing a multilayer FSS substrate to achieve a nearly flat phase response, it is essential to consider an equivalent circuit model of the FSS. For this purpose, we began by first developing a simple, yet useful circuit model for a dipole FSS which led to a multilayer FSS design having a pre-specified reflection coefficient (Chapter 3). This multilayer FSS design was comprised of three layers of crossed dipoles interleaved with resistive cards to smooth out the phase response. This initial design was used as an example in understanding the FSS design for achieving nearly constant phase response over a certain bandwidth. In particular, we demonstrated that one way to achieve smooth phase responses is to compromise the amplitude response by introducing some loss within the substrate.

As part of our design effort, a goal was to also minimize the thickness of the multilayer FSS structure by using rather broadband FSS elements. If the element shape is designed such that both capacitive and inductive surface properties are realized within the same structure, the resulting elements are expected to provide broadband performance. Such a novel, broadband element, namely the fan element, was introduced in this thesis (Chapter 3). This fan-like element can be thought as a combination of a loop (inductive) and dipoles (capacitive). By tuning the lengths of the dipoles and the inner radius of the loop, the resonance behavior of the FSS and its bandwidth can be controlled. Further, when a resistively loaded fan element is used, extremely broadband responses can be achieved. For example, a single layer of such a loaded FSS was designed and shown to provide a broadband reflection response over at least a 2:1 bandwidth where the phase remained nearly constant within the range of [-50°,50°] at the expense of amplitude (Chapter 3).

We then employed the designed fan element FSS as an artificial substrate for a printed dipole array (Chapter 4). The FSS substrate provided a remarkable 2:1 impedance bandwidth as well as enhanced radiation and gain performance for the dipoles over the frequency band of interest. This enhancement is mainly due to the relatively flat phase behavior of the fan element FSS. Since the phase is maintained near 0°, the FSS serves to emulate a magnetic GP so that the reflected field arrives in congruence with the direct dipole radiated field without a resort to the typical quarter wavelength distance between the dipole and GP. Furthermore, when the dipoles were reconfigured to operate at a higher frequency band, they delivered overall bandwidth of 3:1 without a need to change the FSS substrate. The use of resistive loading within the FSS layer resulted in some

efficiency loss (a 3dB or so) in the reflected wave. However, the overall efficiency of the printed dipoles was improved by the inclusion of the FSS, mainly due to in-phase reflections provided by this lossy artificial substrate. A similar bandwidth performance could be achieved using a multilayered lossy dielectric above a GP instead. However, the multilayered lossy configuration would lead to higher losses and to a much thicker GP.

A similar FSS substrate consisting of fan elements was also employed as an artificial substrate for a slot array, again resulting in a 2:1 bandwidth enhancement (Chapter 5). However, in this case, the resistive loading introduced in the FSS layer was also associated with a 3-6 dB gain losses over the band. These efficiency losses were mainly due to the higher order reflections taking place within the cavity below the slot aperture. In effect, most of the reflected power was consumed within the cavity. Although the FSS substrate provided bandwidth enhancement for slots, the overall efficiency was degraded more than that of the dipoles. Thus, an additional effort was made to minimize this efficiency loss and improve the gain performance of the slots. We demonstrated that the slot array efficiency could be improved by compromising impedance bandwidth. In this respect, critical FSS parameters were found to be the resistive loading and the FSS-to-aperture spacing and it was shown that by optimizing these parameters accordingly, the gain performance could be improved.

In practice, to preserve bandwidth enhancement due to the FSS substrate, an equally broadband feed is required. For this purpose we designed a new balun/feed consisting of a YY microstrip-to-slotline transition in its input port and a tapered slot-line at the output for impedance transformation (Chapter 6). We considered such a feed component for our designs due to its low loss and compact planar structure. The resulting

feed configuration provided a 6:1 bandwidth for a VSWR < 3 when terminated with a load of 100-200 Ω (this load was used to emulate equivalent slot impedances). The final integrated structure incorporating the slot array, FSS substrate and balun/feed was also fabricated and tested to validate the simulations. For the simulations, we considered a two-stage modeling of the whole structure due to its computational complexity. It was demonstrated that the slot/FSS/balun configuration provided nearly a 2:1 bandwidth matched to a 50Ω system.

Finally, we demonstrated the performance of a reconfigurable slot array over a multilayer FSS substrate (Chapter 7). We considered crossed slots as the array elements due to their polarization agility. In addition, the proposed two-band array configuration provided for an almost 40% reduction in array size to avoid the occurrence of grating-lobes. In practice, the reconfiguration is achieved by means of MEMS switches or PIN diodes. These devices were modeled as simple on/off switches across the slot widths and their effect on the impedance characteristics was shown to be negligible.

Considering the FSS performance with crossed slots, we demonstrated that a single layer resistively loaded fan element FSS allowed for a bandwidth of 0.8-3.2 GHz without a need for reconfiguration. To extend this bandwidth coverage beyond 3.2 GHz, we considered an additional FSS layer consisting of resistive patch elements just underneath the slots. The inclusion of this secondary FSS greatly enhanced bandwidth performance for the high-band operation (3.2-6.4 GHz). However, this inclusion along with the presence of parasitic (unexcited) high-band slot elements degraded bandwidth performance for the low-band operation (0.8-3.2 GHz). As a result, a discontinuity was formed in the frequency response, leaving a gap between the low and high band

responses. To close this gap, and achieve more continuous bandwidth coverage over the 0.8-6.4 GHz band, we altered the radiating slot design by introducing reactive loading along the length of the slot. The purpose of this type of loading was to increase the inductance per unit length of the slot element and thus slow down the wave, with the goal of decreasing the antenna's operational frequency. Consequently, the high-band response was shifted downwards, and the impedance response was more uniform across the entire band. Such a novel loading technique provided an almost 10:1 impedance bandwidth (0.7-7 GHz) coverage with a single reconfiguration.

The analysis and design of the proposed multilayer array/FSS configurations were carried out by means of a fast full-wave simulator based on the finite element-boundary integral (FE-BI) method incorporating fast spectral calculations of the Green's function. The pertinent formulation and validation of the array simulator are given in the Appendix. We remark that an important aspect of this simulator is its capability to model periodic structures, each associated with different periodicities. No such analysis exists in the literature for closely packed FSS layers and a new technique was therefore developed and employed to allow for full flexibility in the design as described in the Appendix.

APPENDIX

ANALYSIS AND DESIGN METHODS

The hybrid finite element-boundary integral (FE-BI) method [35] is used for the numerical analysis of multilayer frequency selective surface (FSS) structures of interest. An important aspect of this hybrid technique is the capability to simulate and design structures which are complex in geometry and incorporate a variety of materials. A multilayer FSS or a frequency selective volume (FSV) in the presence of an antenna array is one such structure as shown in Figure A.1. The highly adaptable finite element method (FEM) [40] is used for modeling the multilayer dielectric region whereas the BI serves as a means of truncating the FE mesh. The BI submatrix typically consumes most of the CPU requirements. Therefore, a recently introduced scheme referred to as the fast spectral domain algorithm (FSDA) [41] is employed to speed up the BI calculations in the context of iterative solvers. As compared to the adaptive integral method (AIM), the FSDA often provides two orders of magnitude faster solutions with memory as well as CPU time complexity of $O(N)$ [41]. Thus, the adaptability of the FE-BI method along with the speed-up advantage of the FSDA serves as a very efficient analysis tool while designing antenna arrays with multilayer FSS's.

Below the hybrid FE-BI formulation in conjunction with the FSDA implementation for the periodic infinite arrays [1] is presented along with several scattering and radiation examples for validation purposes.

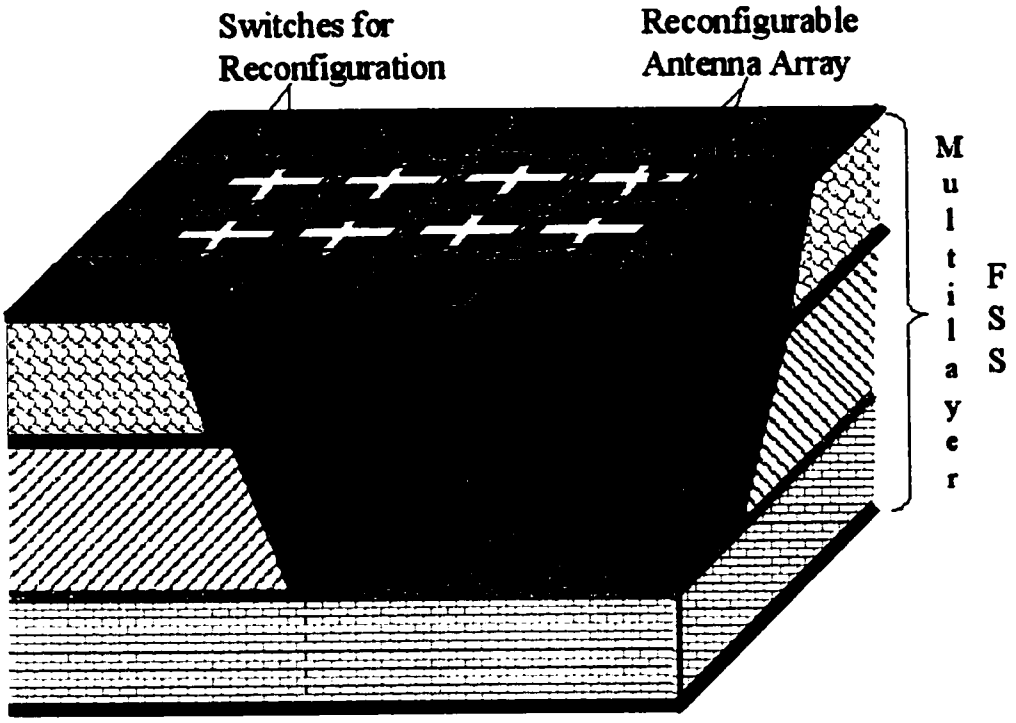

Figure A.1: Reconfigurable antenna aperture over a multilayer FSS structure.

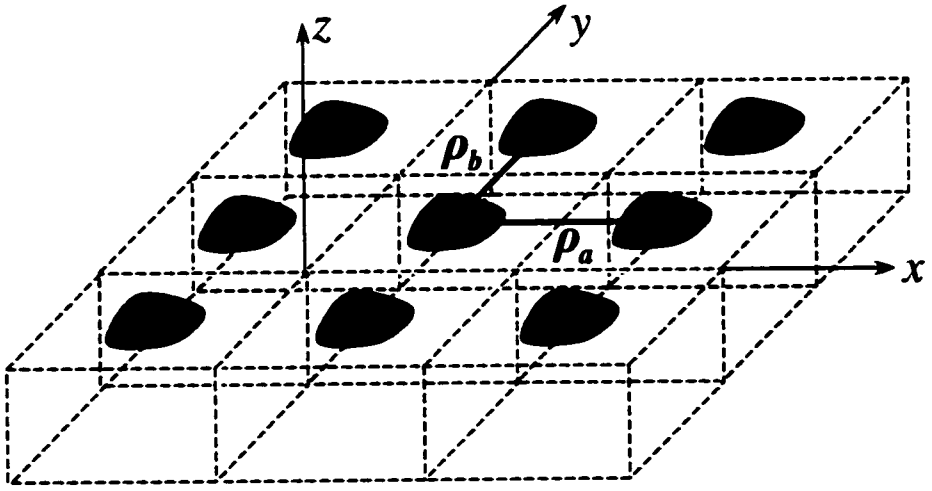

Figure A.2: Infinite doubly periodic structure.

Hybrid Finite Element-Boundary Integral Formulation for Infinite Periodic Array Analysis

We consider the doubly periodic array configuration illustrated in Figure A.2. The array is assumed to be periodic in the *xy*-plane and the (*p*, *q*) cell of the array is obtained by shifting the (0,0) cell through the relation

$$\boldsymbol{\rho}_{pq} = p\,\boldsymbol{\rho}_a + q\,\boldsymbol{\rho}_b \tag{A.1}$$

where $\boldsymbol{\rho}_a$ and $\boldsymbol{\rho}_b$ are the lattice vectors parallel to the *xy*-plane. For periodic excitation of the array with a linear phase factor, time harmonic electromagnetic fields (an $e^{j\omega t}$ time dependence is assumed and suppressed throughout) obey the periodicity conditions

$$\begin{aligned} \mathbf{E}(\mathbf{r}+\boldsymbol{\rho}_{pq}) &= \mathbf{E}(\mathbf{r})\,e^{-j\mathbf{k}_{t00}\cdot\boldsymbol{\rho}_{pq}} \\ \mathbf{H}(\mathbf{r}+\boldsymbol{\rho}_{pq}) &= \mathbf{H}(\mathbf{r})\,e^{-j\mathbf{k}_{t00}\cdot\boldsymbol{\rho}_{pq}} \end{aligned} \tag{A.2}$$

with

$$\mathbf{k}_{t00} = k_{x00}\hat{\mathbf{x}} + k_{y00}\hat{\mathbf{y}} = \pm(k_0 \sin\theta_0 \cos\phi_0 \hat{\mathbf{x}} + k_0 \sin\theta_0 \sin\phi_0 \hat{\mathbf{y}}) \tag{A.3}$$

where k_0 is the free space wavenumber and (θ_0, ϕ_0) are the scan angles of a phased array (positive sign) or the arrival angles of an incident plane wave (negative sign) [42].

Based on the periodicity condition (A.2), the solution domain can be restricted to a single unit cell of the periodic array and the finite element method is employed to model the unit cell volume with appropriate periodic (or phase) boundary conditions (PBCs) for the side walls (see Figure A.3). Truncation of the FE mesh on the unit cell aperture (top and/or bottom) is carried out by using the boundary integral. The contribution of other cells is included through the Floquet theory along with the infinite periodic Green's function and the PBCs. The formulation of this implementation is

already available in the literature [42]-[45] and a summary of this formulation is presented in the following.

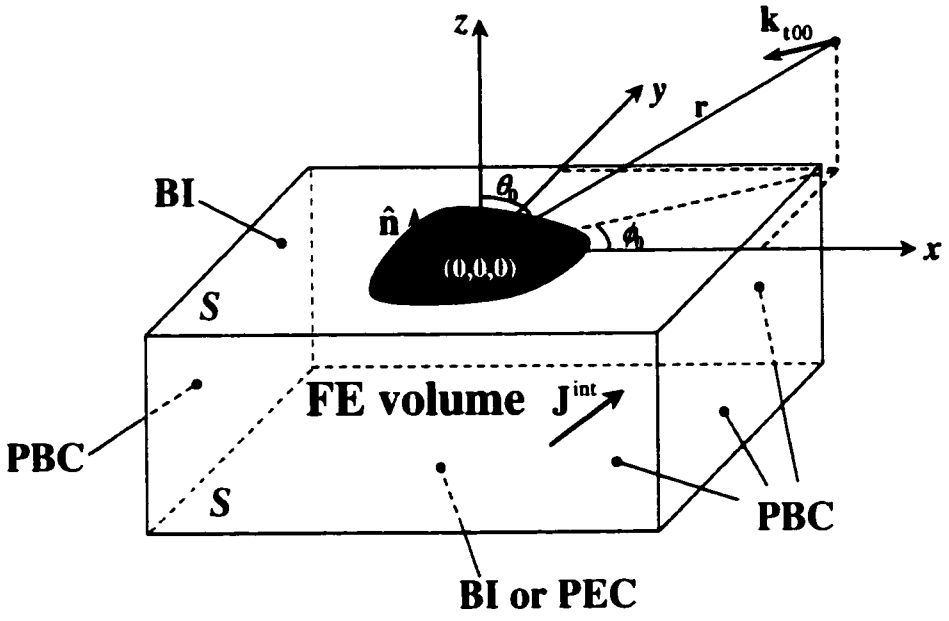

Figure A.3: Unit cell of infinite periodic array with BI termination on top and bottom surfaces and PBCs at vertical boundaries.

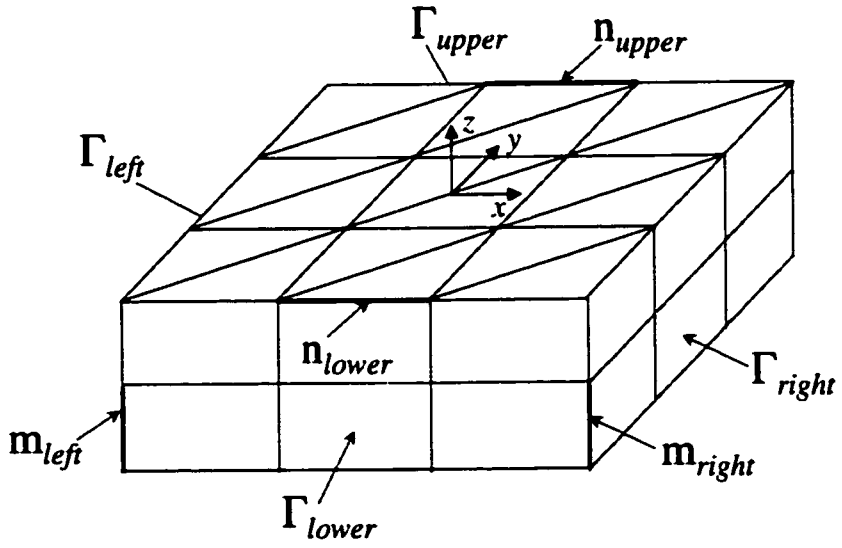

Figure A.4: FE mesh consisting of triangular prisms.

One can start with the well-known vector wave equation for the electric field and proceed using Galerkin's testing to obtain the weak form of the wave equation. The pertinent FE functional for the total electric field then takes the form [40]

$$F(\mathbf{T},\mathbf{E}) = \iiint_V \left[\mu_r^{-1}(\nabla\times\mathbf{T})\cdot(\nabla\times\mathbf{E}) - jk_0^2\varepsilon_r\mathbf{T}\cdot\mathbf{E} + jk_0Z_0\mathbf{T}\cdot\mathbf{J}^{\text{int}}\right]dv + jk_0Z_0\iint_S \mathbf{T}\cdot(\mathbf{H}\times\hat{\mathbf{n}})\,ds \tag{A.4}$$

where $\mathbf{T}$ is the weighting (or testing) function, $\mathbf{J}^{\text{int}}$ denotes an excitation current interior to the FE volume V, S represents boundary surface of the FE domain, $\hat{\mathbf{n}}$ is the unit surface normal directed out of the FE domain (see Figure A.3), and Z_0 is the wave impedance of free space. Even though (A.4) can also be extended to anisotropic material fillings where relative permittivity/permeability is represented in tensor form, here we only consider isotropic materials throughout. To solve (A.4) for $\mathbf{E}$, one requires knowledge of $\mathbf{H}$ over S. In the context of the FE-BI method, the relation between $\mathbf{H}$ and $\mathbf{E}$ is determined by the BI equation

$$\mathbf{H} = -2j\frac{k_0}{Z_0}\iint_S \overline{\mathbf{G}}_P(\mathbf{r},\mathbf{r}_s)\cdot(\mathbf{E}\times\hat{\mathbf{n}})\,ds + \mathbf{H}^{\text{exc}} \tag{A.5}$$

where $\overline{\mathbf{G}}_P(\mathbf{r},\mathbf{r}_s)$ is the spatial domain periodic Green's function given by

$$\overline{\mathbf{G}}_P(\mathbf{r},\mathbf{r}_s) = \left(\bar{\mathbf{I}} + \frac{1}{k_0^2}\nabla\nabla\right)\sum_{p=-\infty}^{\infty}\sum_{q=-\infty}^{\infty} e^{-j\mathbf{k}_{t00}\cdot\boldsymbol{\rho}_{pq}}\frac{e^{-jk_0R_{pq}}}{4\pi R_{pq}} \tag{A.6}$$

with

$$R_{pq} = \left|\mathbf{r} - \mathbf{r}_s - \boldsymbol{\rho}_{pq}\right| \tag{A.7}$$

Here $\bar{\mathbf{I}}$ is the unit dyad, $\mathbf{r}$ and $\mathbf{r}_s$ are the observation and source points, respectively, and ρ_{pq} is defined in (A.1) and $\mathbf{k}_{t00}$ in (A.3). Also, $\mathbf{H}^{exc}$ is a possible external excitation in the presence of a metallic interface in the periodic aperture S.

To construct a linear set of equations using (A.4) and (A.5), one must first tessellate the unit cell volume and introduce expansions for each of the tessellation. Here we employ edge-based basis functions on triangular prismatic elements [46], resulting in triangular surface meshes with Rao-Wilton-Glisson (RWG) basis functions [47] for the equivalent magnetic currents on the top and bottom BI surfaces of the unit cell. A simplified FE mesh with triangular prisms for a unit cell of an infinite periodic array is depicted in Figure A.4 where the four vertical walls of the FE mesh are designated as pairs of opposite sidewalls, namely, (Γ_{lower}, Γ_{upper}) and (Γ_{left}, Γ_{right}). The fields on a vertical boundary of the FE mesh are related to the fields on the opposite boundary by (A.2) through a phase relation. As an example, if $e_{m_{left}}$ is the unknown field at an edge on one of the vertical walls (see Figure A.4), the value of the field at the corresponding edge on the opposite sidewall is given by

$$e_{m_{right}} = e_{m_{left}} e^{-j\mathbf{k}_{t00}\cdot\rho_n} \qquad \text{A.8}$$

provided the surface meshes of the opposite vertical walls are identical, which is easily satisfied using prismatic meshes. The relation (A.8) becomes very useful during the implementation since the unknowns on the surface Γ_{lower} (Γ_{left}) can be eliminated by relating them to those on Γ_{upper} (Γ_{right}) using (A.8).

A situation of interest is the case of non-commensurate FSS or antenna array structures where the periods change from layer to layer as shown in Figure A.5. In

general, an exact formulation of the periodic array problem is possible in case of a commensurate configuration where the structure has a unique periodicity. However, an exact analysis is also possible for non-commensurate structures if a super cell can be defined which is an integer multiple of all different layer periodicities. Despite being a solution option, this approach can be computationally expensive in many cases since the super cell may include a large number of the different layer periods. Alternatively, by modeling each of the periodic lattices separately, a boundary integral can be used at each layer interface and the individual Floquet modes can be tracked forward and backward from one layer to the other, yet still very time consuming. Instead, as proposed in [48] and [49], for planar integral equation methods, an approach based on decoupling the periods of the currents within different layers can provide reasonably accurate results with lower computational effort. In the case of the hybrid FE implementation, a similar approach can be employed by decoupling of the field periodicities [50]. As described in [50], the fields in each layer are presumed to fulfill the PBCs of that layer, thus yielding a decoupling of the different periodicities. This is achieved by meshing the structure according to the geometric periods of each layer as depicted in Figure A.6. For the PBC implementation within the FE mesh, the staircased sidewalls must carefully be dealt with. Using periodic continuation of the different decoupled layers, the edge unknowns within each layer interface are related to the corresponding edges inside the volume mesh to bound the FE domain [50]. Of course, this is only an approximate model as compared to the rigorous approach given in [51], but its accuracy can arbitrarily be improved by grouping several cells in the individual layers with a higher computational effort..

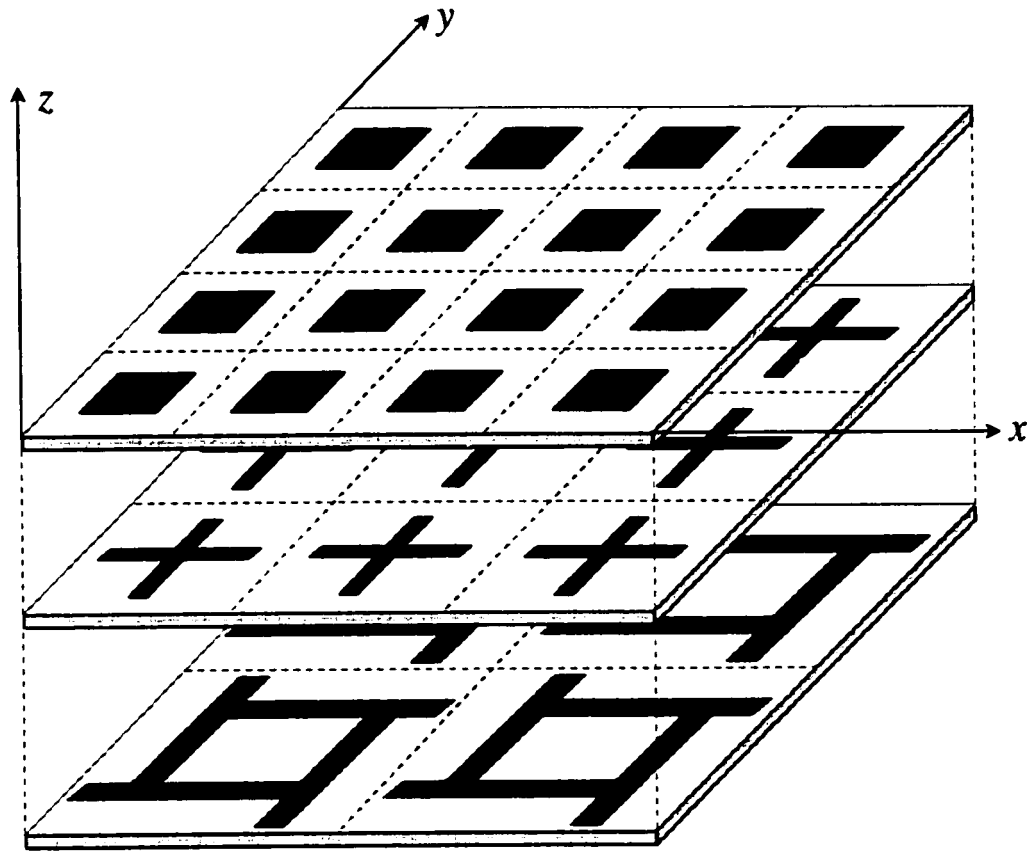

Figure A.5: A multilayer non-commensurate FSS configuration.

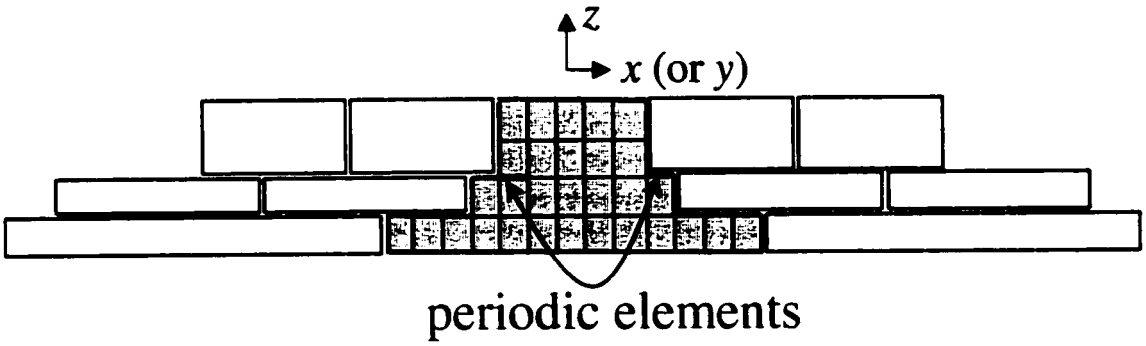

Figure A.6: Decoupling of individual layer periodicities for non-commensurate structures in the context of the FE-BI modeling.

Having employed the discretization of the computational domain as described above, the hybrid FE-BI implementation leads to a linear algebraic system, of the form

$$\begin{bmatrix} A^{\text{int}} & A^{cross}_{1,top} & A^{cross}_{1,bot} \\ A^{cross}_{2,top} & A^{bound}_{top} & 0 \\ A^{cross}_{2,bot} & 0 & A^{bound}_{bot} \end{bmatrix} \begin{Bmatrix} E^{int} \\ E^{bound}_{top} \\ E^{bound}_{bot} \end{Bmatrix} + \begin{bmatrix} 0 & 0 & 0 \\ 0 & Z_{top} & 0 \\ 0 & 0 & Z_{bot} \end{bmatrix} \begin{Bmatrix} E^{int} \\ E^{bound}_{top} \\ E^{bound}_{bot} \end{Bmatrix} = \begin{Bmatrix} f^{int} \\ f^{bound}_{top} \\ f^{bound}_{bottom} \end{Bmatrix} \qquad \text{A.9}$$

The A matrices are sparse (around 30 non-zero entries per row) and are associated with the FE portion of the hybrid method, whereas the BI Z matrices are fully populated and are associated with the top and bottom boundaries of the unit cell. The right-hand side vector elements f represent excitations within the FE-BI domain [1].

For arbitrary scan angles of the array, the matrices in (A.9) can be non-symmetric due to the periodicity conditions as well as the periodic Green's function. Hence, the non-symmetric biconjugate gradient (BiCG) iterative solver [40] was used for the solution of the matrix system. The major computational burden in the solver is due to the matrix-vector product represented by the left-hand side of (A.9). The total A matrix is sparse and its complexity (per matrix-vector product) is $O(N_V)$ where N_V is the number of edges within the FE volume. On the other hand, since the Z matrices are fully populated, the complexity of pertinent matrix-vector products becomes $O(N^2_{\text{top/bot}})$ with storage requirements of the same order (using a direct solver) where $N_{\text{top/bot}}$ is the number of BI unknowns in top/bottom BI surfaces. Therefore, it is crucial to reduce the complexity of the BI matrix-vector products for a more efficient implementation. For array problems, it also becomes essential to reduce the number of the explicitly computed BI matrix entries as far as possible due to relatively high numerical cost for generating the periodic Green's function. To overcome these computational burdens, the FSDA [1] was carried out in our

array modeling. The FSDA is especially attractive for reducing the complexity of the matrix-vector products since it is completely free of generating any BI matrix entries. The formulation of the FSDA as described in [1] is presented in the following section.

Fast Spectral Domain Algorithm (FSDA)

In the spectral domain method, the BI equation (A.5) can be written as

$$\mathbf{H}(\mathbf{r}) = -2j\frac{k_0}{Z_0}\int_{k_t}\int_{k_y}\tilde{\bar{\mathbf{G}}}_P(k_x,k_y)\cdot\left(\tilde{\mathbf{E}}(k_x,k_y)\times\hat{\mathbf{n}}\right)e^{-jk_t\cdot x}e^{-jk_y y}dk_x dk_y \qquad \text{A.10}$$

where ~ denotes 2-D Fourier transforms. Note that $\mathbf{H}^{exc}$ in (A.5) is skipped here for simplicity. In (A.10), $\tilde{\mathbf{E}}(k_x,k_y)$ is the Fourier transform of the electric field intensity on the top/bottom apertures of the unit cell and $\tilde{\bar{\mathbf{G}}}_P(k_x,k_y)$ denotes the spectral representation of the periodic Green's function, given by [44]

$$\tilde{\bar{\mathbf{G}}}_P(k_x,k_y) = \frac{1}{2jAk_0^2}\sum_{p=-\infty}^{\infty}\sum_{q=-\infty}^{\infty}\frac{1}{k_z}\begin{bmatrix}k_0^2-k_x^2 & -k_xk_y\\ -k_xk_y & k_0^2-k_y^2\end{bmatrix}\delta\left(\mathbf{k}_t-\mathbf{k}_{tpq}\right) \qquad \text{A.11}$$

where $A=|\boldsymbol{\rho}_a\times\boldsymbol{\rho}_b|$ is the cross-sectional area of the unit cell's top/bottom boundary surface (see Figure A.2). Also,

$$\mathbf{k}_t = k_x\hat{x}+k_y\hat{y} \qquad \text{A.12}$$

$$\mathbf{k}_{tpq} = \mathbf{k}_{t00}+\frac{2\pi}{A}\left[p(\boldsymbol{\rho}_b\times\hat{z})+q(\hat{z}\times\boldsymbol{\rho}_a)\right] \qquad \text{A.13}$$

is the so-called reciprocal lattice vector, and

$$k_z = \sqrt{k_0^2-\mathbf{k}_t\cdot\mathbf{k}_t} \qquad \text{A.14}$$

with the branch cut taken so that $\mathrm{Re}(k_z)\geq 0$ and $\mathrm{Im}(k_z)\leq 0$.

In the context of FSDA, we next introduce the expansion

$$\mathbf{E}(\mathbf{r}) = \sum_{m=1}^{N_{top/bot}} E_n \boldsymbol{w}_n(\mathbf{r}) \tag{A.15}$$

where $\boldsymbol{w}_n(\mathbf{r})$ are Whitney edge elements [46], and E_n represents the expansion coefficients. Introducing (A.15) into (A.10) and then applying MoM testing with the weighting functions [40]

$$\boldsymbol{b}_m(\mathbf{r}) = \hat{\mathbf{n}} \times \boldsymbol{w}_m(\mathbf{r}) \tag{A.16}$$

which are well-known RWG basis functions results in [1]

$$\left\langle \boldsymbol{b}_m(\mathbf{r}), \mathbf{H}(\mathbf{r}) \right\rangle = \sum_{p=-\infty}^{\infty} \sum_{q=-\infty}^{\infty} \tilde{\boldsymbol{b}}_m^*(k_{xpq}, k_{ypq}) \cdot \frac{1}{k_0 Z_0 A k_{zpq}} \begin{bmatrix} k_0^2 - k_{xpq}^2 & -k_{xpq}k_{ypq} \\ -k_{xpq}k_{ypq} & k_0^2 - k_{ypq}^2 \end{bmatrix} \cdot \sum_{n=1}^{N_{top/bot}} E_n \tilde{\boldsymbol{b}}_n(k_{xpq}, k_{ypq}) \tag{A.17}$$

where * denotes complex conjugation. Here the discrete wavenumbers k_{xpq} and k_{ypq} are he x- and y-components of the reciprocal lattice vector, respectively, as defined in (A.13). Also, $\tilde{\boldsymbol{b}}_n$ are the Fourier transforms of the RWG basis functions as described in [52]. Note that (1.17) represents the m^{th} row-vector product of $\left[Z_{top/bot}\right]\left\{E_{top/bot}^{bound}\right\}$ and all row-vector products are generated by letting $m = 1, 2, \ldots, N_{top/bot}$.

For a conventional implementation of (A.17), the summation over n along with the E_n coefficients is first moved in front of the infinite spectral sums. The spectral series is then evaluated for each (m, n) combination so as to compute all matrix entries of the BI submatrices $\left[Z_{top/bot}\right]$, thus evaluating the spectral series $N_{top}^2 + N_{bot}^2$ times. Similarly, incase of an iterative solver, the evaluation of the pertinent matrix-vector products also requires $N_{top}^2 + N_{bot}^2$ multiplications. On the other hand, the FSDA provides evaluation of

the matrix-vector products $[Z_{top/bot}]\{E^{bound}_{top/bot}\}$ using only $O(N_{top/bot})$ CPU time complexity for a fixed set of Floquet modes [1]. As described in [1], the following steps are executed to achieve the reduced order complexity:

Step 0 : pre-compute the Fourier transforms $\tilde{\boldsymbol{b}}_n(k_x, k_y)$ and $-2jk_0 / Z_0 \, \tilde{\overline{\mathbf{G}}}_P(k_x, k_y)$ in (A.17) for the discrete wavenumbers $k_x = k_{xpq}$ and $k_y = k_{ypq}$.

Step I : compute the iteration field vector

$$V_{pq} = \sum_{m=1}^{N_{top/bot}} E_n \tilde{\boldsymbol{b}}_n(k_{xpq}, k_{ypq}) \qquad \text{A.18}$$

in the spectral domain for all (p, q) modes.

Step II : compute

$$W_{pq} = -2jk_0 / Z_0 \, \tilde{\overline{\mathbf{G}}}_P(k_{xpq}, k_{ypq}) \cdot V_{pq} \qquad \text{A.19}$$

for all (p, q) modes.

Step III : finally, compute

$$\sum_p \sum_q \tilde{\boldsymbol{b}}^*_m(k_{xpq}, k_{ypq}) \cdot W_{pq} \ , \ m = 1, 2, \ldots, N_{top/bot} \qquad \text{A.20}$$

to complete the evaluation of $[Z_{top/bot}]\{E^{bound}_{top/bot}\}$.

For a constant number of (p, q) modes, ***Step I*** requires $C_1 N_{top/bot}$ operations; ***Step II***, C_2 operations; and ***Step III***, $C_3 N_{top/bot}$ operations, where the constants C_1, C_2, C_3 depend on the number of included modes. Thus, summing up all operations needed for the evaluation of the BI matrix-vector products within the iterative solver, we obtain $C_1 N_{top/bot} + C_2 + C_3 N_{top/bot}$ operations, i.e., a CPU time complexity of $O(N_{top/bot})$. Also, $C_4 N_{top/bot}$ operations are needed in ***Step 0*** prior to the iteration process. Thus, the FSDA provides extremely low CPU time complexity as compared to other fast integral methods

such as the fast multipole method (FMM) or the adaptive integral method (AIM) [53], where the near-coupling elements must be calculated explicitly. The memory demand of the FSDA is mainly determined by the pre-computed Fourier transforms of the basis function (in ***Step 0***) and is thus $C_3N_{top/bot}$, i.e., of $O(N_{top/bot})$ as well [1].

As noted above, the constants C_i (i=1,2,3,4,5) depend on the number of Floquet modes to ensure convergence in the spectral series. For larger unit cell sizes, typically, increasing number of modes are required, as is also the case for conventional BI implementations even incase of acceleration techniques such as the Ewald transformation [42] employed. In addition, the convergence of the spectral series is determined by the total field distribution in the BI surfaces, rather than the spectrum of the periodic Green's function or the individual basis functions. In light of this observation, convergence of the spectral series can often be drastically improved by shifting the BI surface by a small distance from the inhomogeneities of the FE volume domain [1], [43].

Accuracy as well as efficiency of the FSDA implementation in connection with the hybrid FE-BI method has been demonstrated in [1] for multilayer frequency selective surface (FSS) configurations. It has been shown that since no matrix elements (including those in the near-zone) are explicitly calculated, the FSDA provides a speed-up of about two orders of magnitude, even for small numbers of BI unknowns (as small as 500), as compared to conventional BI implementations and other fast integral methods such as AIM [1].

In the following section, several FSS and antenna array examples will be presented as the additional validation for the developed array simulator which employs the hybrid FE-BI method in conjunction with the FSDA .

Validation Examples

In this section, we present four representative examples to demonstrate modeling capability as well as accuracy of the fast infinite array simulator. The first two instances examine reflection/transmission through multilayer FSS configurations, and the other two study radiation from slot arrays. Simulation results will be presented along with measured or literature data for validation purposes.

Double Layer Jerusalem Cross Frequency Selective Surface

We first consider reflection from a metal-backed, double layer Jerusalem cross FSS. For validation purposes, a 7x7 finite array of the Jerusalem cross FSS was built, and reflection coefficient measurements were carried out. The corresponding unit cell geometry of the non-commensurate structure is shown in Figure A.7 along with the dimensions given in Table A.1. Comparison between measurements (finite array) and calculations (infinite array) for the reflection coefficient are displayed in Figure A.8. As seen, the full-wave simulator and measured data agree quite well for both magnitude and phase of the reflection coefficient, thus validating the accuracy of the simulator. Also, note that here the metallic FSS elements were interleaved with resistive cards [54] in order to suppress strong phase variations. In the following chapters, it will be shown that resistively loaded FSS elements provide broadband reflections with flat phase response.

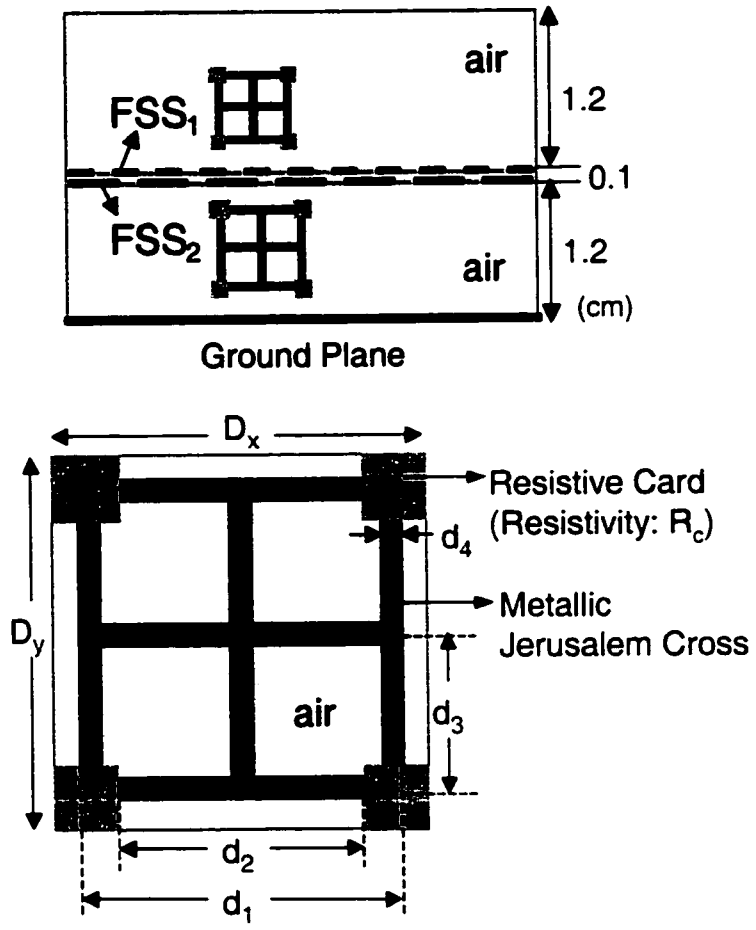

Figure A.7: Configuration and unit cell geometry of the double layer Jerusalem cross FSS.

(cm)	FSS_1	FSS_2
d_1	9.60	13.21
d_2	6.98	10.16
d_3	5.05	6.86
d_4	0.51	0.51
$D_{x(y)}$	10.67	13.72
$R_C(\Omega/cm^2)$	370	230

Table A.1: Dimensions of the double layer Jerusalem cross FSS.

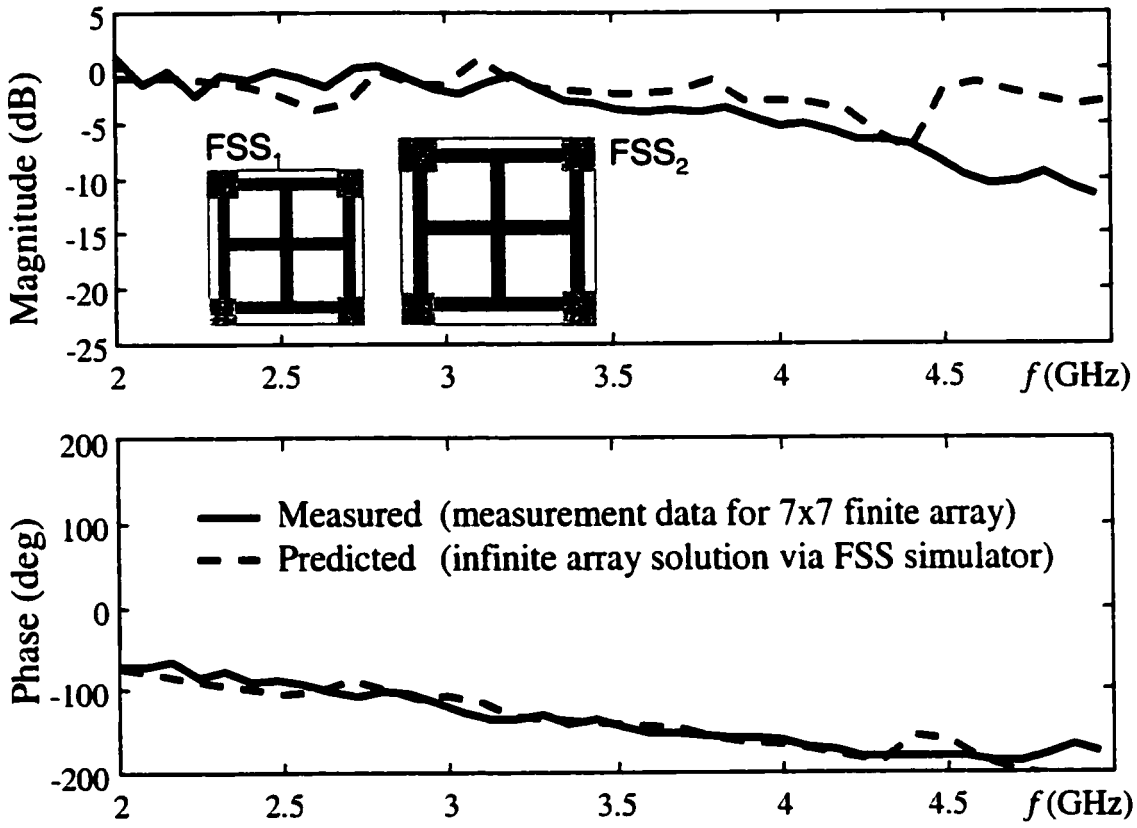

Figure A.8: Reflection coefficient of the double layer Jerusalem cross FSS: comparison between predicted (simulated) and measured data.

Circular Slot Frequency Selective Surface

Secondly, we consider a circular or ring slot FSS printed on a 0.3μm substrate with ε_r=16 (see Figure A.9). This FSS is intended for use in the thermo-photovoltaic filter applications. In this case, the FSS serves the purpose of rejecting frequency bands possibly damaging to photovoltaic cells exposed to infrared radiations (as may be the case for photovoltaic panels used to power satellites). Below we present a brief characterization of this FSS.

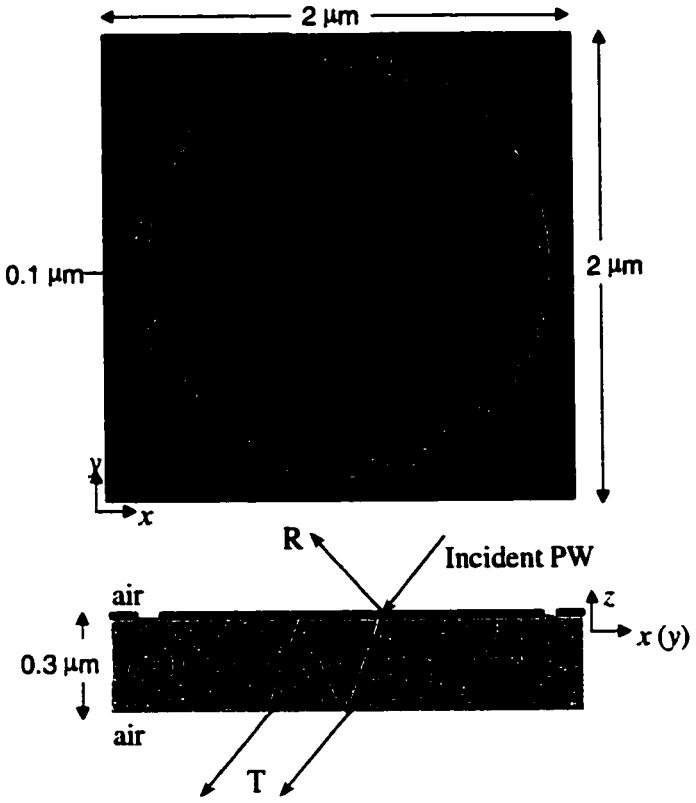

Figure A.9: Unit cell geometry of dielectric-backed circular slot array.

Before proceeding with the characterization of the ring slot FSS, we first carried out a validation of our FE-BI periodic implementation with data based on a standard moment method (MoM) analysis [55][1]. Two different meshes were generated for modeling of the circular geometry as illustrated in Figure A.10. The comparison given in Figure A.11 shows that the FE-BI solution is in complete agreement with MoM data when the unstructured grid/mesh is employed with 0.1μm per edge length (mesh was generated by SDRC-IDEAS). However, our simpler structured mesh generated by triangles of the rectangular grid of density 0.1μm x 0.1μm does show some shift in frequency. This is due to the staircasing associated with the approximation of the ring slot.

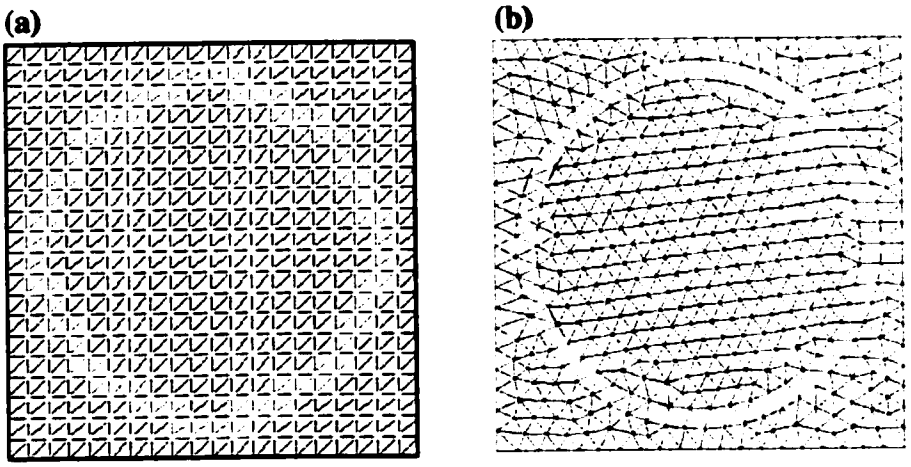

Figure A.10: Triangular surface meshes for modeling of the ring slot FSS: (a) structured mesh; (b) unstructured mesh generated by SDRC-IDEAS.

---

[1] The data given in [55] are in error for the ring slot. Dr. Wu provided the new data in Figure A.11 for comparison with our calculations.

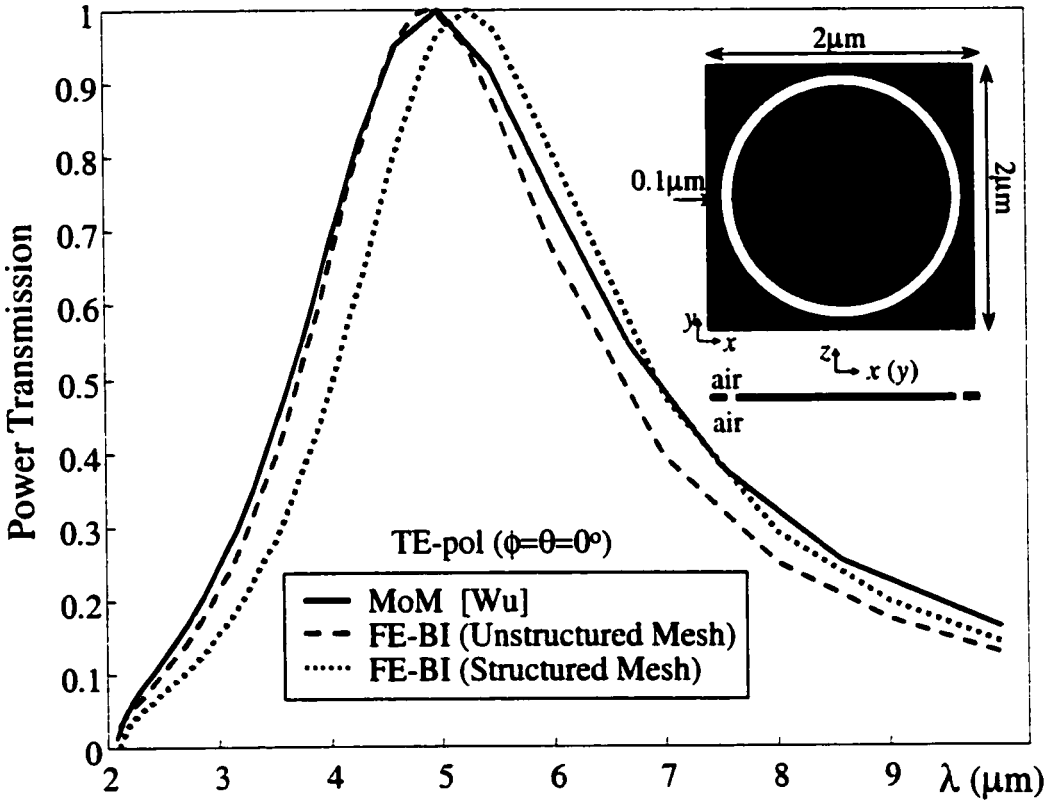

Figure A.11: Validation of the FE-BI solution with the MoM for the free-standing ring slot FSS.

For the application at hand, we are interested in the performance of FSS for different incidence angle. Ideally, we would like the FSS to retain its bandwidth as the incident angle is varied since incoming radiation can be received from all angles. Figure A.12 displays the transmission properties of the dielectric-backed ring slot FSS (see Figure A.9). As seen, the behavior of the FSS is fairly well maintained with maximum transmission occurring at about 17.65THz (λ=17μm). For the TE-polarization, the transmission bandwidth narrows as the incidence angle moves away from normal. However, for TM polarized incidence, the bandwidth increases with incidence angle. Thus, on the average for a randomly polarized signal, the FSS is likely to pass similar levels of power for different oblique incidence angles.

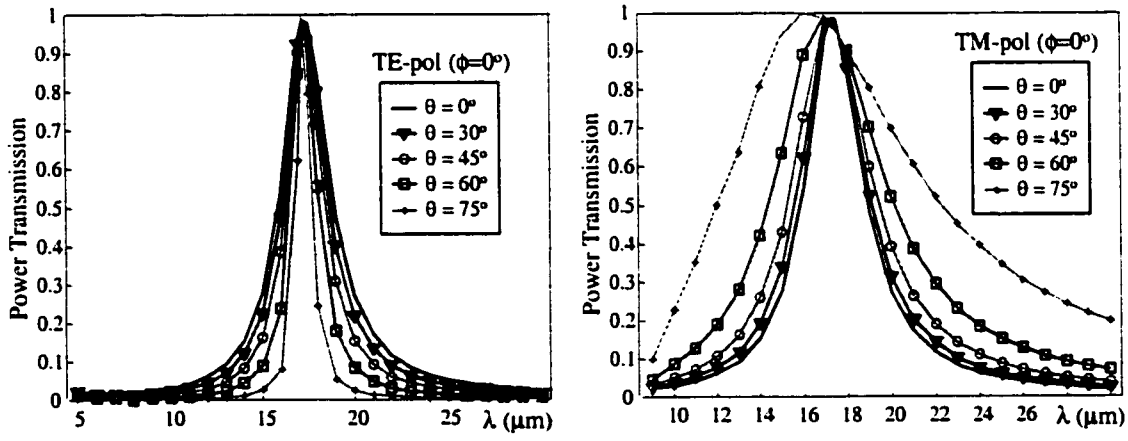

Figure A.12:Transmitted power by the dielectric-backed circular slot FSS at different incidence angles for TE and TM polarizations.

Cavity-backed Cross Slot Array

Next, we consider radiation from a cavity-backed cross slot array. A 3x5 finite cross slot array was fabricated, and radiation pattern measurements were carried out. The array configuration is depicted in Figure A.13. As shown, only seven of the center slot elements were excited while the others remained inactive. In addition, shorting pins were placed among slot elements, along the cavity depth. Here, the vertical pins are used with the intention of suppressing possible parasitic modes which may occur within the cavity. Also, note that triangular periodicity is used for array configuration to avoid grating lobes as well as to achieve broadband operation. Later, it will be shown that this choice of gridding suits quite well for reconfiguration of slot arrays.

For validation purposes, we carried out two analysis approaches. First, we obtained the equivalent aperture currents within the unit cell of the slot array by using the infinite array simulator. These currents were then integrated to compute the far-zone element pattern (E-plane) at broadside. Finally, the element pattern was multiplied by the 3x5 array factor to calculate the overall array pattern. Note that only those terms of the array factor corresponding to the excited slot elements (see Figure A.13) were considered in the multiplication process. As a second approach, we analyzed the exact finite array geometry shown in Figure A.13 by using a well validated full-wave simulator [34]. In Figure A.14, the corresponding E-plane radiation patterns are displayed for the measurements along with the simulations. As seen, the agreement between the measured and simulated data is well correlated for the main beam, but it deteriorates towards the sidelobes. Since the array truncation was not realized exactly in the simulations, the diffraction effects due to edges could not be accurately accounted for, resulting in some deviation in sidelobe levels as observed in Figure A.14.

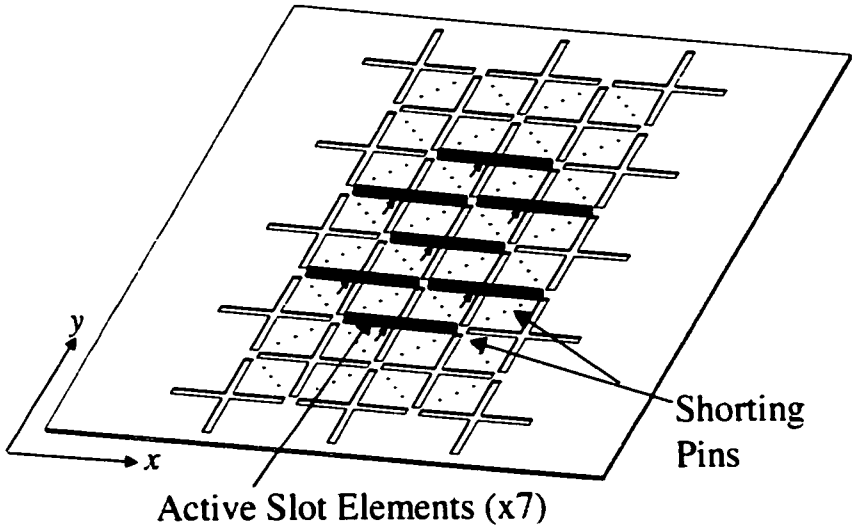

Figure A.13: 3x5 cross slot array: only seven center elements as shown were excited.

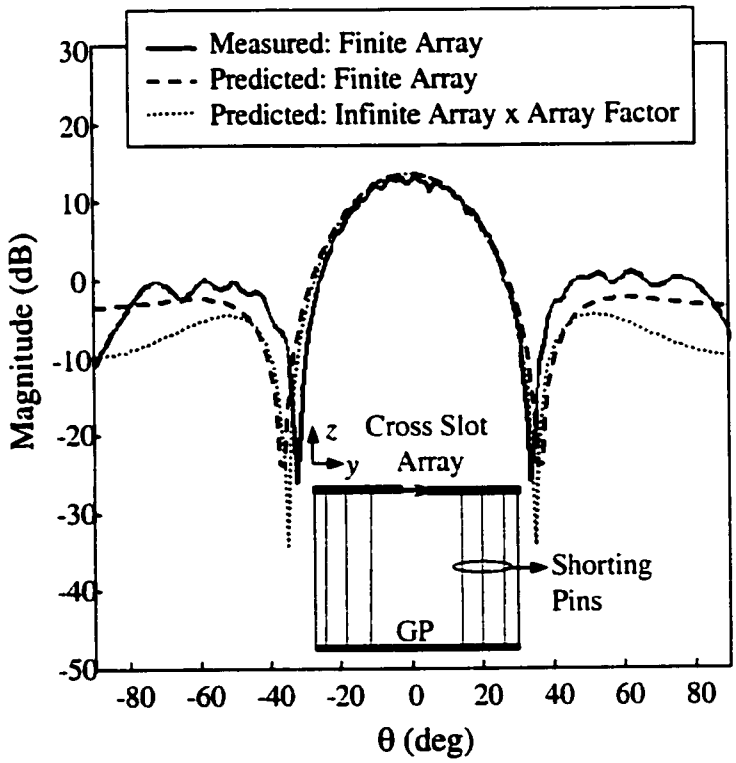

Figure A.14: E-plane radiation patterns for the 3x5 cross slot array: measurements vs. simulations.

BIBLIOGRAPHY

BIBLIOGRAPHY

[1] Eibert, T. F. and J. L. Volakis, "Fast spectral domain algorithm for hybrid finite element/boundary integral modelling of doubly periodic structures," *IEE Proc.-Microw. Antennas Propag.*, vol. 147, no. 5, pp. 329-334, Oct. 2000.

[2] Erdemli, Y. E., K. Sertel, R. A. Gilbert, D. E. Wright, and J. L. Volakis, "Frequency selective surfaces to enhance performance of broadband reconfigurable arrays," accepted in *IEEE Trans. Antennas Propag.*, Nov. 2001.

[3] Erdemli, Y. E., J. L. Volakis, D. E. Wright, and R. A. Gilbert, "Reconfigurable conformal slot arrays on artificial substrates," in IEEE Antennas Propagat. Int. Symp., pp. 338-341, 2001.

[4] Yngvesson, K. S., D. H. Schaubert, T. L. Korzeniowski, E. L. Kollberg, T. Thungren, J. F. Johansson, "Endfire tapered slot antennas on dielectric substrates," *IEEE Trans. Antennas Propag.*, vol. 33, pp. 1392-1400, Dec. 1985.

[5] Filipovic, D. S., M. Nurnberger, and J. L. Volakis, "Ultra wideband slot spiral with dielectric loading: measurements and simulations," in IEEE Antennas Propagat. Int. Symp., pp. 1536-1539, 2000.

[6] Nurnberger, M. W., J. L. Volakis, J. A. Mosko, and T. Ozdemir, "Analysis of the log-periodic folded slot array," in IEEE Antennas Propagat. Int. Symp., pp. 1282-1285, 1994.

[7] Brown, E. R., "RF-MEMS switches for reconfigurable integrated circuits," *IEEE Trans. Microwave Theory Tech.*, vol. 46, pp. 1868-1880, Nov. 1998.

[8] Schiek, B. and J. Kohler, "An improved microstrip-to-microslot transition," *IEEE Trans. Microwave Theory Tech.*, pp. 231-233, Apr. 1976.

[9] Chung, H. H., W. Foy, and S. Y. Peng, "Printed crossed slot phased array antenna system for mobile satellite communication," in IEEE Antennas Propagat. Int. Symp., pp. 204-207, 1988.

[10] Contopanagos, H., L. Zhang, and N. G. Alexopoulos, "Thin frequency-selective lattices integrated in novel compact MIC, MMIC, and PCA architectures," *IEEE Trans. Microwave Theory Tech.*, vol. 46, pp. 1936-1948, Nov. 1998.

[11] Coccioli, R., F.-R. Yang, K.-P. Ma, and T. Itoh, "Aperture-coupled patch antenna on UC-PBG substrate," *IEEE Trans. Microwave Theory Tech.*, vol. 47, pp. 2123-2130, Nov. 1999.

[12] Schumpert, J. D., W. J. Chappell, and L. P. B. Katehi, "Parallel-plate mode reduction in conductor-backed slots using electromagnetic band gap substrates," *IEEE Trans. Microwave Theory Tech.*, vol. 47, pp. 2099-2104, Nov. 1999.

[13] Collin, R., Field Theory of Guided Waves. New York: IEEE Press, 1991.

[14] Sigalas, M. M., R. Biswas, Q. Li, D. Crouch, W. Leung, R. Jacobs-Woodbury, B. Laogh, S. Nielsen, S. McCalmont, G. Tuttle, and K.-M. Ho, "Dipole antennas on photonic band-gap crystals: experiment and simulation," *Microwave Opt. Technol. Lett.*, vol. 15, no. 3, pp. 153-158, June 1997.

[15] Yang, H.-Y. D., N. G. Alexopolous, and E. Yablonovitch, "Photonic bandgap materials for high-gain printed circuit antennas," *IEEE Trans. Antennas Propagat.*, vol. 45, pp. 185-187, Jan. 1997.

[16] Leung, W. Y., R. Biswas, S.-D. Cheng, M. M. Sigalas, J. S. McCalmont, G. Tuttle, and K.-M. Ho, "Slot antennas on photonic bandgap crystals," *IEEE Trans. Antennas Propagat.*, vol. 45, pp. 1569-1570, Oct. 1997.

[17] Gonzalo, R., P. De Maagt, M. Sorolla, "Enhanced patch antenna performance by suppressing surface waves using photonic-bandgap substrates," *IEEE Trans. Microwave Theory Tech.*, vol. 47, pp. 2131-2138, Nov. 1999.

[18] Sievenpiper, D., L. Zhang, R. F. J. Broas, N. G. Alexopolous, and E. Yablonovitch, "High-impedance electromagnetic surfaces with a forbidden frequency band," *IEEE Trans. Microwave Theory Tech.*, vol. 47, pp. 2059-2074, Nov. 1999.

[19] Li, Z. and Y. Rahmat-Samii, "PBG, PMC and PEC ground planes: a case study of dipole antennas," in IEEE Antennas Propagat. Int. Symp., pp. 674-677, 2000.

[20] Park, J. Y., C.-C. Chang, Y. Qian, and T. Itoh, "An improved low-profile cavity-backed slot antenna loaded with 2D UC-PBG reflector," in IEEE Antennas Propagat. Int. Symp., pp. 194-197, 2001.

[21] Rahman, M. and M. A. Stuchly, "Wide-band microstrip patch antenna with planar PBG structure," in IEEE Antennas Propagat. Int. Symp., pp. 486-489, 2001.

[22] Caloz, C., C.-C. Chang, Y. Qian, and T. Itoh, "A novel multilayer photonic band-gap (PBG) structure for microstrip circuits and antennas," in IEEE Antennas Propagat. Int. Symp., pp. 502-504, 2001.

[23] *J. Opt. Soc. Amer. B, Opt. Phys.* (Special Issue), vol. 10, Feb. 1993.

[24] Ma, K.-P., K. Hirose, F.-R. Yang, Y. Qian, and T. Itoh, "Realisation of magnetic conducting surface using novel photonic bandgap structure," *Electron. Lett.*, vol. 34, no. 21, pp. 2041-2042, Oct. 1998.

[25] Contopanagos, H., C. Kyriazidou, W. Merrill, and N. G. Alexopoulos, "Physical realization of magnetic walls using finite-thickness 3D printed arrays," in IEEE Antennas Propagat. Int. Symp., pp. 1916-1919, 1999.

[26] Kyriazidou, A. C., H. F. Contopanagos, W. M. Merrill, and N. G. Alexopoulos, "Artificial versus natural crystals: effective wave impedance of printed photonic bandgap materials," *IEEE Trans. Antennas Propag.*, vol. 48, pp. 107-116, Jan. 2000.

[27] Sievenpiper, D., "High-impedance electromagnetic surfaces," Ph.D. dissertation, Dept. Electrical Engin., Univ. California at Los Angeles, Los Angeles, CA, 1999.

[28] Mittra, R., C. H. Chan, and T. Cwik, "Techniques for analyzing frequency selective surfaces – A review," *Proc. IEEE*, vol. 76, pp. 1593-1615, Dec. 1988.

[29] Munk, B. A., Frequency Selective Surfaces. New York: J. Wiley, 2000.

[30] Yeo, J. and R. Mittra, "Bandwidth enhancement of multiband antennas using frequency selective surfaces for ground planes," in IEEE Antennas Propagat. Int. Symp., pp. 366-369, 2001.

[31] Volakis, J. L., M. W. Nurnberger, and D. S. Filipovic, "A broadband cavity-backed slot spiral antenna," *IEEE Antennas Propagat. Mag.*, vol. 43, no. 6, pp.15-26, Dec. 2001.

[32] Nelder, J. A. and R. Mead, "A simplex method for function minimization," *Computer Journal*, vol. 7, pp. 308-313, 1965.

[33] Hansen, R. C., Phased Array Antennas. New York: J. Wiley, 1998.

[34] Jin, J.-M. Jin and J. L. Volakis, "A hybrid finite element method for scattering and radiation by microstrip patch antennas and arrays residing in a cavity," *IEEE Trans. Antennas Propag.*, vol. 39, pp. 1598-1604, Nov. 1991.

[35] Volakis, J. L., T. Ozdemir, and J. Gong, "Hybrid finite-element methodologies for antennas and scattering," *IEEE Trans. Antennas Propag.*, vol. 45, pp. 493-507, Mar. 1997.

[36] Balanis, C. A., Antenna Theory: Analysis and Design. New York: Harper & Row, 1982.

[37] Trifunovic, V. and B. Jokanovic, "Review of printed marchand and double Y baluns: characteristics and applications," *IEEE Trans. Microwave Theory Tech.*, vol. 42, pp. 1454-1462, Aug. 1994.

[38] Kragalott, M., W. R. Pickles, and M. S. Kluskens, "Design of a 5:1 bandwidth stripline notch array from FDTD analysis," *IEEE Trans. Antennas Propag.*, vol. 48, pp. 1733-1741, Nov. 2000.

[39] Wadell, B. C., Transmission Line Design Handbook. Boston: Artech House, 1991.

[40] Volakis, J. L., A. Chatterjee, and L. C. Kempel, Finite Element Method for Electromagnetics. New York: IEEE Press, 1998.

[41] Eibert, T. F. and J. L. Volakis, "Fast spectral domain algorithm for rapid solution of integral equations," *Electron. Lett.*, vol. 34, no. 13, pp. 1297-1299, June 1998.

[42] Eibert, T. F., J. L. Volakis, D. R. Wilton, and D. R. Jackson, "Hybrid FE/BI modeling of 3D doubly periodic structures utilizing triangular prismatic elements and a MPIE formulation accelerated by the Ewald transformation," *IEEE Trans. Antennas Propag.*, vol. 47, pp. 843-850, May 1999.

[43] Lucas, E. W. and T. W. Fontana, "A 3-D hybrid finite element/boundary element method for the unified radiation and scattering analysis of general infinite periodic arrays," *IEEE Trans. Antennas Propag.*, vol. 43, pp. 145-153, Feb. 1995.

[44] McGrath, D. T. and V. P. Pyati, "Phased array antenna analysis with the hybrid finite element method," *IEEE Trans. Antennas Propag.*, vol. 42, pp. 1626-1630, Dec. 1994.

[45] McGrath, D. T. and V. P. Pyati, "Periodic structure analysis using a hybrid finite element method," *Radio Sci.*, vol. 31, no. 5, pp. 1173-1179, Sept./Oct. 1996.

[46] Ozdemir, T. and J. L. Volakis, "Triangular prisms for edge-based vector finite element analysis of conformal antennas," *IEEE Trans. Antennas Propag.*, vol. 45, no. 5, pp. 788-797, May 1997.

[47] Rao, S. M., D. R. Wilton, and A. W. Glisson, "Electromagnetic scattering by surfaces of arbitrary shape," *IEEE Trans. Antennas Propag.*, vol. 30, no. 3, pp. 409-418, 1982.

[48] Vardaxoglou, J. C., A. Hossainzadeh, and A. Stylianou, "Scattering from two-layer FSS with dissimilar lattice geometries," *IEE Proc. H*, vol. 140, no. 1, pp. 59-61, Feb. 1993.

[49] Aroudaki, H., V. Hansen, H.-P. Gemund, and E. Kreysa, "Analysis of low-pass filters consisting of multiple stacked FSS's of different periodicities with applications in the submillimeter astronomy," *IEEE Trans. Antennas Propag.*, vol. 43, pp. 1486-1491, Dec. 1995.

[50] Eibert, T. F. and J. L. Volakis, "Hybrid FE/BI modeling of commensurate and non-commensurate 3D doubly periodic structures," in IEEE Antennas Propagat. Int. Symp., pp. 338-341, 1998.

[51] Bhattacharyya, A. K., "Analysis of multilayer infinite periodic array structures with different periodicities and axes orientations," *IEEE Trans. Antennas Propag.*, vol. 48, pp. 357-369, Mar. 2000.

[52] McGrath, D. T., "Phased array antenna analysis using hybrid finite element methods," Ph.D. dissertation, Air Force Institute of Technology, Wright-Patterson AFB, OH, June 1993.

[53] Volakis, J. L., T. F. Eibert, and K. Sertel, "Fast integral methods for conformal antenna and array modeling in conjunction with hybrid finite element formulations," *Radio Sci.*, vol. 35, no. 2, pp. 537-546, Mar./Apr. 2000.

[54] Senior, T. B. A. and J. L. Volakis, "Sheet simulation of a thin dielectric layer," *Radio Sci.*, vol. 22, no. 7, pp. 1261-1272, Dec. 1987.

[55] Wu, T.-K., "Infrared filters for high efficiency thermovoltaic devices," *Microwave Opt. Technol. Lett.*, vol. 15, no. 1, May 1997.